Universitat Autònoma de Barcelona

Myosin VB in intestinal pathogenesis

Fernando Cartón García

Myosin VB in intestinal pathogenesis

Doctoral thesis presented by

Fernando Cartón García

For the PhD degree
Biochemistry, Molecular Biology and Biomedicine doctorate program

Biochemistry and Molecular Biology Department
Faculty of Medicine
Universidad Autónoma de Barcelona

Work carried out in
Group of Biomedical Research in Digestive Tract Tumors

Molecular Biology and Biochemistry Research Center
(CIBBIM-Nanomedicine)

Vall d'Hebron Research Institute

June 2017

DIRECTOR
Dr. Diego Arango

ACADEMIC TUTOR
Dr. Joan Seoane

PhD STUDENT
Fernando Cartón

INDEX

RESUMEN

Miosina VB es una proteína que actúa como un motor molecular usando la energía del ATP para moverse a lo largo de filamentos de actina. Participa en el trafico intracelular de endosomas de reciclaje en la parte subapical de células polarizadas y no polarizadas. Su expresión es muy abundante en el intestino donde participa en el establecimiento y mantenimiento de la polaridad de los enterocitos. Mutaciones en *MYO5B* causan la enfermedad de inclusión de microvellosidades, in raro trastorno congénito que afecta a las células epiteliales del intestino cursando con diarrea acuosa persistente que suele ser fatal. Esta enfermedad se caracteriza por la presencia de alteraciones morfológicas en los enterocitos, atrofia de las vellosidades y deslocalización de proteínas del polo apical y basolateral del enterocito. Su patología molecular no se conoce, principalmente por la falta de modelos animales. En el presente estudio, describimos un versátil modelo murino con inactivación constitutiva de *Myo5b* e inactivación condicional en las células epiteliales intestinales inducida por tamoxifeno. En ambos casos, los animales muestras un cuadro clínico muy semejantes al de los pacientes con enfermedad de inclusión de microvellosidades, presentado diarrea y deshidratación que causan la muerte del animal. A nivel histológico, el intestino muestra las mismas alteraciones en los enterocitos que las presentes en pacientes humanos, incluyendo atrofia de vellosidades y deslocalización de marcadores proteicos. Además, la inactivación de *Myo5b* también provocó hiperproliferación de las criptas intestinales. Por lo tanto, el modelo animal presentado constituye una herramienta muy útil para investigar las causas moleculares de la enfermedad y ensayar de manera preclínica fármacos u otras opciones terapéuticas. Por otro lado, la pérdida de polaridad y diferenciación es también una de las señas de identidad de los carcinomas metastásicos avanzados y correlaciona con un mal pronóstico de los pacientes. En concreto, para el cáncer colorrectal, investigaciones previas llevadas a cabo en nuestro laboratorio ya han demostrado que la pérdida de miosina IA promueve la progresión la enfermedad y tiene actividad supresora de tumores. Dicha proteína es

abundante en el borde en cepillo de los enterocitos, y participa en el mantenimiento de la estructura polarizada. Otros estudios han señalado la relación entre la inactivación de *MYO5B* con un incremento en la motilidad e invasión de células de cáncer gástrico, aunque todavía no se conoce nada de su relación con en el cáncer colorrectal. Para resolver esta cuestión, hemos diseñado modelos *in vitro* inducibles por doxiciclina para sobre expresar y reducir la expresión de dicha proteína en líneas celulares de cáncer de colon. Además, se ha empleado la tecnología CRISPR/Cas9 para inactivar la expresión de *MYO5B* en la línea de cáncer de colon Caco2-BBE. Los resultados muestran cambios en la polarización y diferenciación de dichas líneas celulares, de acuerdo con observaciones previas. También se ha observado una posible relación entre MYO5B y la capacidad de movilidad e invasión de las líneas de cáncer de colon. Sin embargo, la hiperproliferación observada en el intestino de los ratones no se reproduce en las líneas de cáncer de colon empleadas tras reducir o sobre expresar MYO5B, o en modelos *xenograft* subcutáneos *in vivo* de dichas líneas. Por otro lado, usando un microarray de tejidos con 155 muestras de tumores primarios de pacientes con cáncer colorrectal en estadio Dukes C se ha comprobado que una reducción en la expresión de MYO5B se asocia con una disminución en el tiempo de recaída y en la supervivencia total de los pacientes de cáncer de colon. Además, tumores con un grado de diferenciación bajo también expresan niveles de MYO5B significativamente reducidos. Finalmente, todos estos resultados indican que MYO5B juega un papel importante en la diferenciación del intestino normal y de las líneas de cáncer de colon. De la misma manera, MYO5B también podría desempeñar un papel en la progresión del cáncer colorrectal promoviendo la movilidad e invasión de las células tumorales.

ABSTRACT

Myosin VB is a molecular motor protein that uses the energy of ATP to move along actin filaments. It participates in the recycling endosomes trafficking in the subapical cytoplasmic region of non-polarized and polarized cells. It is highly expressed in the small and large intestine, where its role in the establishment of polarized function in enterocytes is also well known. Inactivating mutations of *MYO5B* have been associated with microvillus inclusion disease (MVID), a rare congenital disorder of the intestinal epithelial cells that presents with persistent life-threatening watery diarrhea. It is characterized by morphological enterocyte abnormalities such as microvillus atrophy and mislocalization of apical and basolateral protein transporters. The molecular pathology of the disease is not well known mainly due to the lack of animal models. In the present study, we report a versatile murine model with targeted inactivation of *Myo5b*. This model allowed us to generate and characterized a constitutive *Myo5b* knockout mice and a tamoxifen-inducible intestinal-epithelium-specific *Myo5b* knockout. In both cases, the mice closely resemble the phenotype of MVID patients, developing watery diarrhea and dehydration causing the death of the animal. Histological study of the intestine showed all the characteristic enterocyte defects observed in MVID patients, including microvillus atrophy and mislocalization of protein markers. Moreover, the inactivation of MYO5B also originated hyperproliferation of the intestinal crypts. Therefore, our mice constitute a useful model to further investigate the underlying molecular mechanism of this disease and to preclinically assess the efficacy of novel therapeutic approaches. In addition, hyperproliferation as well as loss of cell polarity, differentiation, and tissue architecture are hallmarks of advanced metastatic carcinomas and strongly correlate with poor patient prognosis. Specifically, for colorectal cancer, the third most common type of cancer worldwide, we have previously demonstrated that the loss of brush border MYO1A, also involved in cell polarity, promotes cancer progression and has tumor suppressor activity. Other studies have indicated a relationship between MYO5B inactivation and gastric cancer, promoting

invasion and motility, but little is known regarding its role in colorectal cancer. To address this question, we have developed novel doxycycline-inducible *in vitro* models of MYO5B overexpression and downregulation. Moreover, we have generated MYO5B knockout Caco2-BBE cells using CRISPR/Cas9 technology. Our results showed changes in the polarization and differentiation of colon cancer cells, in agreement with previous observations in the normal intestine. Moreover, we have observed a relationship between MYO5B and the motility and invasion capacity of colon cancer cells, indicating a possible role of MYO5B in colon cancer progression. However, the effect of MYO5B loss in cell proliferation observed in our *Myo5b* knockout mice could not be confirmed in our models *in vitro* and *in vivo*, employing cell line-derived xenografts. In addition, using a tissue microarray containing triplicate samples from 155 primary Dukes C colorectal tumors, reduced MYO5B expression was found to be associated with shorter disease-free and overall survival of the patients. Moreover, poorly differentiated tumors showed significantly reduced expression of MYO5B. Collectively, our results indicate that MYO5B plays an important role in the differentiation of the normal intestinal epithelium and colon cancer cells, as well as a possible role in cancer progression promoting cell motility and invasion.

1.1 Anatomy and Histology of the human digestive tract

1.1.1 Anatomy and histology of the small intestine

The **duodenum** is the shortest part of the intestine (around 25 cm long). It connects the stomach to the jejunum and has an elongated C shape. It has no connection with the mesentery, being partially covered by the peritoneum. It receives the secretions from the pancreas and liver through the pancreatic and common bile ducts. These secretions allow neutralizing the acid coming from the stomach and facilitate the digestion of the fats. It also contains digestive enzymes for the breakdown of carbohydrates and proteins. The **jejunum** begins at the duodenojejunal junction and extends for around 2.5 m. It shows a deep red color, consequence of its high vascularization which allows for a fast absorption and transport of the nutrients. It has a thick wall formed by smooth circular and longitudinal muscles layers whose contraction is responsible for the movement of the food through a process called peristalsis. The **ileum** is the longest part of the small intestine with around 3.5 m length. It continues from the jejunum until the ileocaecal junction. Its walls are thinner that in the jejunum and it is less vascularized with a pale pink color. Both jejunum and ileum are attached to the posterior abdominal wall trough the **mesentery.** The mesentery has a supportive function carrying blood and lymphatic vessels to the intestine and it has been recently proposed as a new organ of the human body [2,3].

The intestinal wall is formed by four different layers: mucosa, submucosa, muscular layer and serosa (Figure 2). The two inner layers (mucosa and submucosa) form circular folds, structures known as **kerkring valves**. They constitute projections to the lumen of the intestine with a maximum height of 8 mm, whose function is to increase the absorptive surface and delay the passage of the food. They are more abundant in the duodenum and jejunum disappearing at the end of the ileum. Moreover, the mucosa is additionally folded in millions of smaller projections (0.5-1 mm) called **villi**. In short, all these structures highly increase the absorptive surface of the intestine that has been estimated in 32 m^2, improving the uptake of the nutrients. The mucosa is also covered by tubular pits connected to the lumen through small apertures between the villi. These invaginations are termed intestinal glands or **crypts of Lieberkhün**, in honor to their discoverer Jonathan Nathanael Lieberkhün (1711–1756) (**Figure 2**) [2,3].

The **mucosa** is formed by the epithelium, the underlying lamina propia and the "muscularis mucosae", a smooth muscle layer (**Figure 2**).

Epithelium: It is covering the villi and crypts. The most abundant cell types covering the villi are the **enterocytes** (>90% of the cells). They are tall columnar cells displaying a highly polarized structure and specialized in the absorption and digestion of some of the nutrients. Their luminal pole is covered by microvilli, microscopical projections of the plasmatic membrane with an approximate length of 1 μm that greatly increased the absorptive surface. The surface microvilli is seen as a brush border in light micrographs (**Figure 4**) [3,4]. Scattered among the enterocytes are the **goblet cells,** which represent between 7-10% of the cells. These cells are in charge of producing mucin, high molecular weight glycoproteins that form a gel layer, known as mucus that lubricates and physically protects the intestine from the passage of the food. It hosts the endogenous microbiota adapted to symbiotic living within the gut, and acts as a dynamic protective barrier between the epithelium and the luminal contents that often includes pathogen bacteria, parasites and viruses. They also participate in the immune defense of the intestine secreting IgA antibodies [3,5,6]. The **Enteroendocrine** cells (EEC) represent a small minority (1%) of the overall epithelial cell population and reside disseminated in the villi and crypts. They produce and secrete a wide variety of peptide hormones to the lamina propia that regulate gastrointestinal motility and secretion. They can be classified in at least 15 subtypes, depending on the peptides they produce [3,7]. **Microfold** cells (M cells) reside in the specialized epithelium that overlies the Peyer's patches, lymphoid tissue in the intestinal wall. It acts as a sampling system that transfers antigens to the underlying tissue for the production of antibodies [3,8,9]. The last cell subtype found in the villi is the **tuft** cells that produce opioids [9]. **Paneth cells** are exclusively located in the base of the crypts of Lieberkhün. They have long been known to produce and secrete bactericidal products such as lysozyme, defensins and mucus. Paneth cells also secrete factors that help to sustain the epithelial stem/progenitor cells in the crypts of the small intestine [3,8,10].

Lamina propia: is a thin layer of connective tissue that forms the scaffold of the villi and supplies blood, innervation and lymph drainage to the mucosa (**Figure 2**). It presents accumulation of lymphocytes and macrophages that form lymphoid follicles, known as Peyer's patches. These follicles can be detected macroscopically as white patches [3].

Muscularis mucosae: it consists of two layers of smooth muscle, an external longitudinal and internal circular layer (**Figure 2**). Its contraction is responsible for expelling the glandular crypts keeping a constant gentle agitation that facilitates the digestion and absorption of the nutrients [3].

The **submucosa** is a layer of connective tissue that lies beneath the *muscularis mucosa.* Blood vessels, lymphatic vessels, nerve network and ganglion neurons are found here (**Figure 2**). Its collagen and elastin fibers distributed in a specific disposition confer support, elasticity and resistance for the peristaltic movements [3].

The **muscularis propia or muscularis externa** of the small intestine consists of two layers of smooth muscle with a similar disposition to the *muscularis mucosae*; an outer layer of longitudinal muscle fibers and an inner thicker layer of circular fibers. Its contraction is responsible of the peristalsis (Figure 2).

Finally, the **serosa** is the outer layer tissue which conducts the major vessels, adipose tissue and nerves. It separates the intestine from the surrounding peritoneal cavity [3] (**Figure 2**).

1.1.3 The polarized organization of the enterocyte

The enterocytes are the most abundant cells of the intestinal epithelium. As described above, their main functions comprises: absorption of nutrients from the lumen of the intestine through the active molecule transporters on their apical surface, the secretion of a cocktail of hydrolytic enzymes into the lumen and the transport of immunoglobulins from the basolateral surface to the intestinal lumen. In doing so, the enterocytes display a highly differentiated/polarized structure: the nucleus is located in the basal half of the absorbing cell, the Golgi apparatus is in the supranuclear cytoplasm, the mitochondria are concentrated in the apical area of the cytoplasm, and the endoplasmic reticulum (ER) is distributed over the remaining cytoplasm. The plasma membrane of the enterocytes shows too different domains: apical brush border domain and basolateral domain [12–14].

The **apical domain** contains the **brush border** formed by a numerous closely packed microvilli 1-3 µm high and 100 nm wide. These microvilli protrusions are hold by an inner cytoskeleton of actin bundles that anchors to an apical dense network of cytokeratin filaments, the terminal web that promotes the long-term stability of the brush border (**Figure 4**). The proteins villin, fimbrin and espin bundled the individual actin filaments within a microvilli. Moreover, the protrusions are stabilized by binding to the plasma membrane through molecules such as unconventional myosins and ERM (ezrin, radixin, moesin) family proteins. For example, myosin IA and myosin VI cross-link the plasma membrane to the actin core. Ezrin has a similar function after its phosphorylation in the threonine T567 (phospho-ezrin, p-ezrin) that triggers a conformational change from its "close" inactive conformation, unable to bind F-actin, to an "open" active conformation (**Figure 4**). Finally, connection between microvilli is also observed and it is responsible of the organization of the whole brush border that would otherwise be a disordered system. Protocadherin-24 (PCDH24), mucin-like protocadherin (MLPCDH), harmonin and myosin VIIB proteins, are responsible of this function (**Figure 4**). The molecular mechanism underlying brush border formation is described in the "Myosin VB" chapter [12–14].

The **basolateral plasma membrane domain** forms deep folds and contains two different junctional complexes that regulate the permeation of extracellular molecules through the mucosal epithelium. The “tight junctions” or “zonula occludens” are closely associated areas of two cells whose membranes join together forming an impermeable barrier to molecules and ions, ensuring its absorption through the transcellular pathway. They contain three major types of transmembrane proteins, occludins, claudins and junctional adhesion molecules (JAM), that bind the cytoplasmic cytoskeleton through scaffolding proteins ZO-1, 2 and 3. The second type of junctional complexes are the “adherens junctions” more basal than tight junctions that initiate the cell-cell contacts and mediate the maturation and maintenance of the contact. They consist of the transmembrane protein E-cadherin, and intracellular components, p120-catenin, β-catenin and α-catenin that bind to the actin cytoskeleton (Figure 4). [12–15]

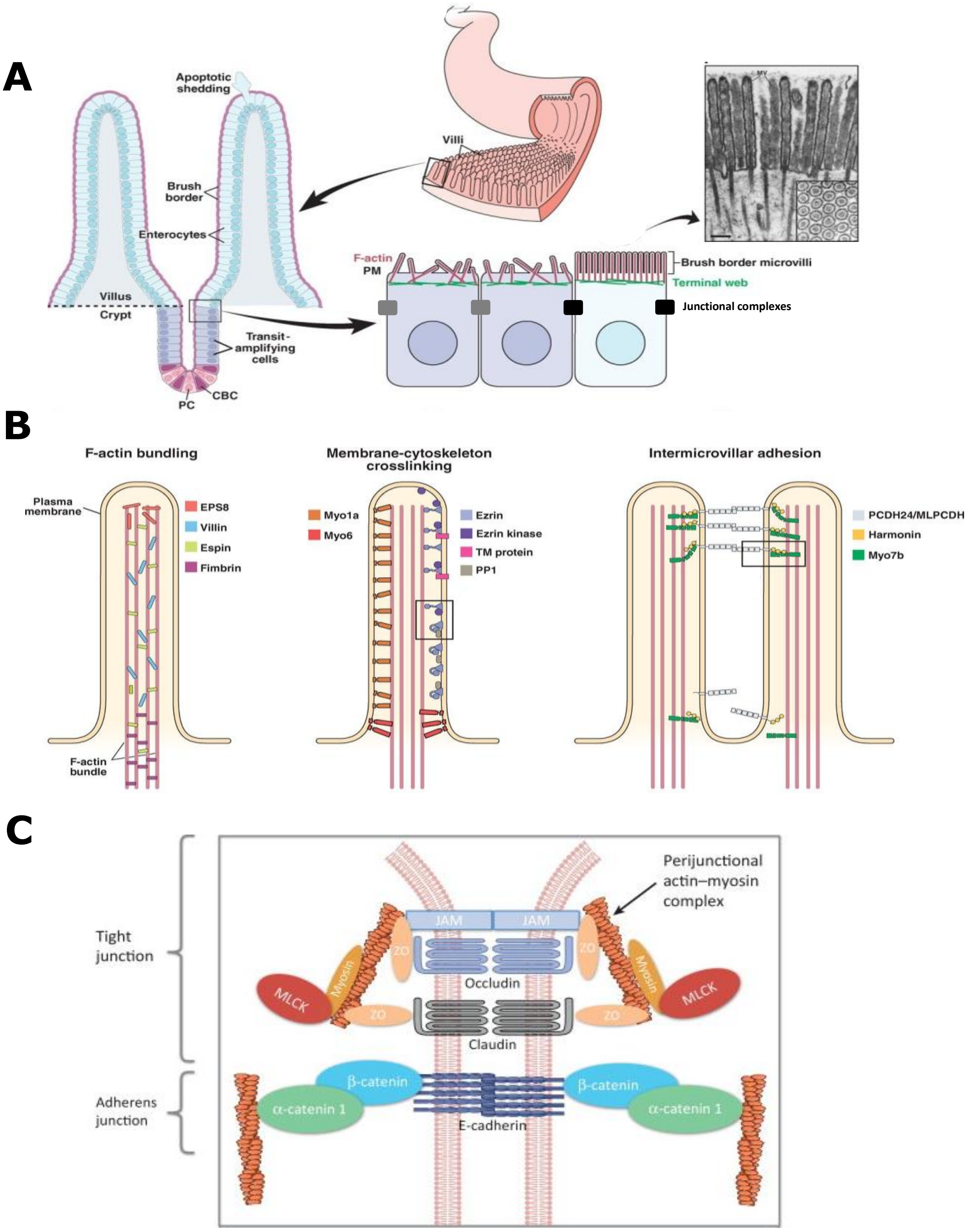

Figure 4. Apical brush border and basolateral domain of the enterocyte. (A) Intestinal villi and microvilli, (PC) Paneth cells, (CBC) crypt base columnar cells, (PM) plasma membrane. **(B)** Bundling of actin filaments in the microvillar actin core is performed through the collective and potentially redundant function of villin, espin, fimbrin, and EPS8. Membrane–cytoskeleton cross-linking plays an important role in microvillar stabilization and is mediated by myosin 1A, myosin 6, and the active form of ezrin; (PP1) possibly protein phosphatase 1, (TM) transmembrane protein. Extracellular adhesion between the distal tips of microvilli is used to optimize the packing of these protrusions during brush border assembly. Intermicrovillar adhesion is mediated by PCDH24, MLPCDH, harmonin and, potentially, myosin VIIB. **(C)** The gut barrier. The single layer of columnar cells in the intestinal epithelium is held together by tight junctions and adherens junctions which regulate the paracellular movement of intraluminal contents. Myosin light chain kinase (MLCK) modulates contraction of the actin–myosin ring. Adapted from Crawley *et al.* 2014 [13] and Mittal *et al.* 2013 [16].

1.2 Phisiology of the human intestinal epithelia

The intestinal epithelium is the fastest self-renewing tissue in the body. All the epithelium derives from the intestinal stem cells confined to the crypts of Lieberkhün, slow-dividing cells with a cell cycle period of 24 h. They give rise to a cohort of rapid proliferating cells that undergo three or four cycles of division (~150 cells dividing every 12 h). These progenitor cells, called "transit-amplifying" cells, migrate upwards from the depths of the crypts onto the surface of the villi, where no further division occurs and gradually differentiate into the principal epithelial lineages: absorptive, goblet, enteroendocrine, tuft, microfold and Paneth cells. Finally, the cells undergo apoptosis and are shed from the villus tips. An exception for this pathway is seen in Paneth cells which migrate downward after differentiation to occupy the crypt base, where they live for 6–8 weeks. This renewal process operates continuously with the cells taking two to seven days from the site of its final division until their exfoliation in the villus tip. In the colon there are no villi, but the organization is similar; cells are discarded into the gut lumen after they emerge onto the exposed flat surfaces around the mouths of the crypts [17–20].

1.2.1 Organization of the intestinal crypt – the stem cell niche

The intestinal epithelium is sustained throughout life by a small number of intestinal stem cells (ISCs) (n = 10–15 per crypt) located at the bottom-most positions that intermingled with Paneth cells (only in the small intestine). The rest of the crypt is occupied by the transit-amplifying cells and mesenchymal cells of the myofibroblast lineage, closely applied to the basal lamina and surrounding the crypt. These non-epithelial cells are believed to secrete various growth factors and cytokines that promote epithelial proliferation [9,20–22].

Currently, two types of stem cells are considered to be found in the crypts: **Crypt base columnar cells (CBC)** that specifically express Leucine-Rich Repeat Containing G Protein-Coupled Receptor 5 (Lgr5+) and generate all type of epithelial cells. They are adjacent to Paneth cells that serve as multifunctional guardians both by secreting bactericidal products and by providing essential niche signals [23–25]. 2) A quiescent population of ISCs or **label retaining cells (LRC)** identified by BMI1, LRIG1, TERT, and HOPX has been proposed to serve as "reserve" stem cells and are located around position +4 relative to the crypt bottom. They are normally destined to become Paneth and enteroendocrine cells but retain the ability to reacquire stem-cell function and can be recruited to serve as a functional stem population under conditions of regeneration [9,20,25,26].

1.2.2 Intestinal stem cell homeostasis – signaling pathways

Canonical Wnt signaling – Wnt signaling is the driving force in the self-renewal of the epithelium since it specifies the identity of the ISCs in the crypts. The Wnt signaling pathway (**Figure 5**) is activated by WNT glycoproteins (WNT3, WNT6 and WNT9B) that bind frizzled (Fz) seven-span transmembrane receptors 5, 6 and 7, and the low-density lipoprotein receptor-related proteins 5 and 6 (LRP5/6) single-span transmembrane correctors. The Wnt signals are provided by adjacent Paneth cells and the surrounding stromal cells [9,27,28]. Expression of the Wnt activator R-spondin-1 also potentiates Wnt pathway and induces ISCs by binding LGR4/LGR5 receptors [29]. Intracellularly, Wnt signaling leads to the stabilization of β-catenin (**Figure 5**) that interacts with the transcription factor of the T-cell factor/lymphoid enhancing factor (TCF/LEF) family to form a bipartite complex: TCF/LEF factors provide the DNA-binding specificity, while β-catenin provides transactivation domains. TCF/LEF target sites are located in promoters and/or enhancers and comprise the conserved sequence AGATCAAAGG [20]. Some of the key target genes activated by Wnt are *c-MYC* [30], cycline D1 [31] and *CD44* [32]. In the absence of a Wnt signal, transcriptional repressors like Groucho bind TCF/LEF transcription factors [20].

persistence of a highly proliferative intestinal epithelium and a deficit of properly differentiated cells. The restriction of the proliferation to the intervillus regions depends on a feedback loop in which mesenchymal cells respond directly to hedgehog from the epithelium, and deliver a signal back to the epithelium by some other signaling pathway [17,34] (**Figure 6**).

BMP pathway inhibits crypt formation – bone morphogenetic protein (BMP) signaling in the intestine represses crypt formation. Under the control of hedgehog signaling, BMP2 and BMP4 proteins are expressed by mesenchymal cells in the villi decreasing proliferation at the crypt–villus border and allowing differentiation. In parallel, epithelial cells express BMP receptor 1A (*BMPR1A).* BMPs, when bound to their receptors, transduce a signal from cytoplasm to nucleus through receptor-mediated phosphorylation of SMAD transcription factors that finally triggers a suppression of Wnt/β-catenin signaling. Thus, conditional deletion of BMPR1A results in hyperproliferative crypts [35]. To coordinate the segregation between proliferation and differentiation, BMPs are active at the top of the crypt, where differentiation occurs. BMPs are also produced at the crypt bottom, but here they are kept in check by BMP inhibitors (such as noggin) that are specifically expressed by the mesenchyme in the ISCs region. Notably, BMPs also have dual functions and are involved in lineage fate decisions towards secretory cells. Through BMPs and noggin, the mesenchymal microenvironment thus secures a spatial organization in the crypt [17,22,36,37] (**Figure 6**).

Notch Signaling: the first decision between absorptive and secretory cell fate – As described above, Notch activity in the intestine determines lineage decisions between enterocyte and secretory cell differentiation, which is the first decision made by daughters of stem cells as they become committed to differentiation [22]**.** Notch receptors are activated by DLL1 and DLL4 ligands, expressed by surrounding cells including Paneth cells. Once activated, the Notch intracellular domain (NICD) is cleaved by γ-secretase and translocated to the nucleus driving the expression of Notch target genes such as HES1 transcription factor [17,22,37,38] (**Figure 6**)**.**

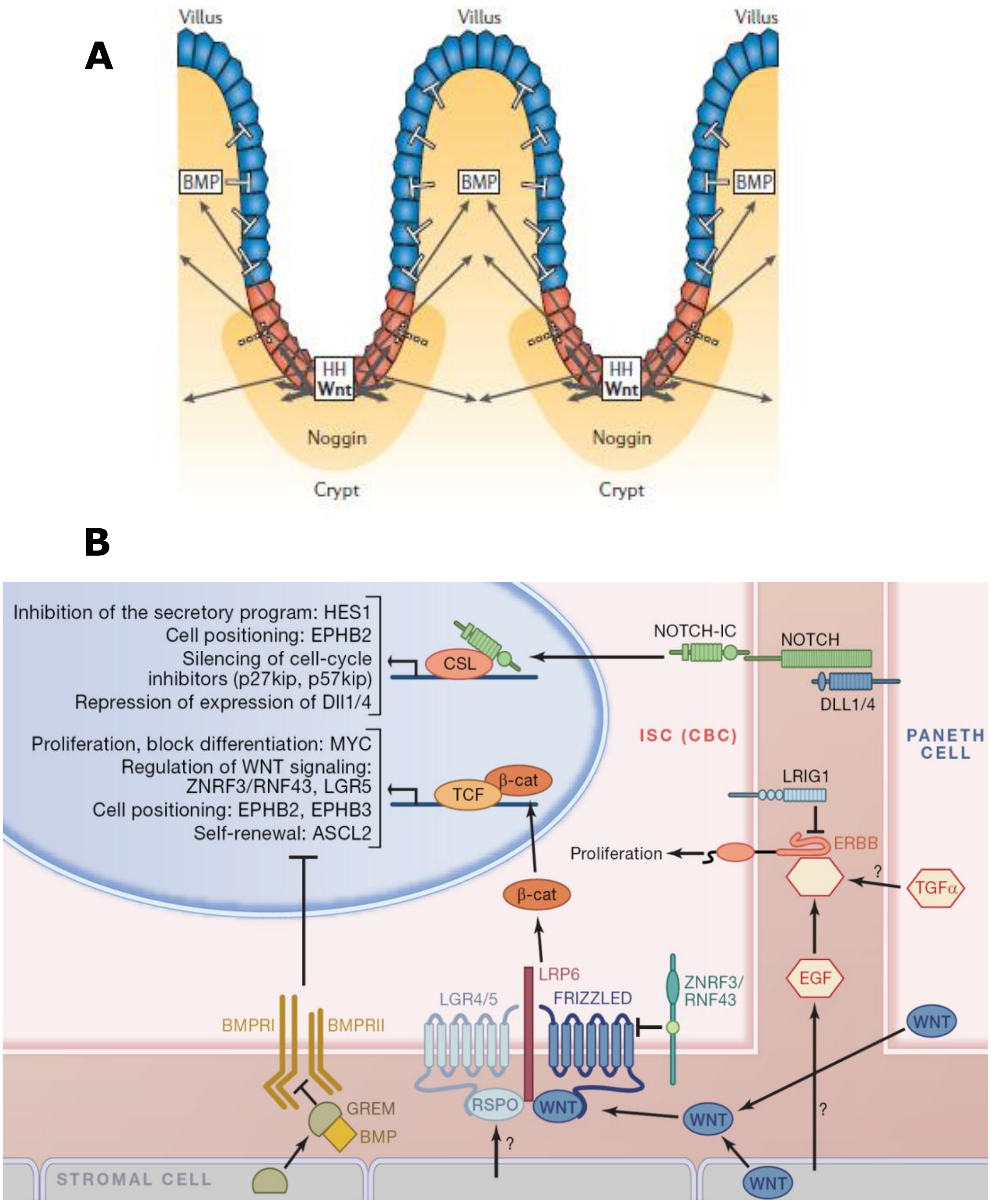

Figure 6. Signaling pathways in the intestinal epithelium.(A) Different signaling pathways between the epithelia and the crypt are combined to organize the pattern of villi and crypts. **(B)** Detailed signaling pathways, transcription factors and its functions. Adapted from Crosnier *et al*. 2006 [17] and Clevers and Batlle 2013 [9]**.**

1.2.3 Differentiation of epithelial cells

ISCs divide symmetrically while competing for a niche of limited size double and stochastically adopt either stem or TA fates [39]. TA cells further differentiate into one of the six cell types of the epithelium that belong to the enteroendocrine or secretory lineages. The Notch pathway seems to play a central function in these intestinal cell fate decisions. Typically, active Notch signaling results in transcription of a first tier of genes of the Hairy/Enhancer of Split (*HES*) class that encode transcriptional repressors. HES repressors in turn repress transcription of a second tier of genes, typically basic helix-loop-helix (bHLH) transcription factors that, induce differentiation along specific lineages. Thus, the direct Notch target gene *HES1* represses transcription of the bHLH transcription factor MATCH-1 that controls differentiation into either absorptive or secretory progenitor cells: *MATCH-1* is required for further differentiate into secretory cells (tuft, goblet or endocrine cells) whereas repression of *MATCH-1* determines absorptive lineage (enterocytes; **Figure 7**). Paneth cells, as the other secretory cells, need the expression of MACTH-1 transcription factor and also active Wnt signaling, although they interpret these signals for their maturation and not for their proliferation. Paneth cells are formed around positions 5–7 of the crypt and subsequently migrate down to position 1. This compartmentalization is achieved through the tyrosine kinase guidance receptors EPHB2 and EPHB3, both activated by Wnt signaling. These tyrosine receptors generate repulsive forces when interacting with their ephrin-B ligands, which are expressed to high levels by villus cells. SOX9 transcription factor, another Wnt target, also plays a role in Paneth cells differentiation. In order to become an M cell, the activation of transcription factor SPI-B is necessary [9,20] (**Figure 7**).

2. Cancer

2.1 General characteristics of cancer

Cancer is a multistep process that occurs on a time scale of months or years and results from the accumulation and selection of genetic and epigenetic alterations originating gain of function of oncogenes and loss of function of tumor suppressor genes. It leads to uncontrolled proliferation, migration and invasion (metastasis) of other tissues and organs. Cancer can be understood as a microevolutionary process that depends on the same principles of mutation and natural selection that govern the long-term evolution of all living organisms.

2.1.1 Classification

Cancer types are classified depending on the tissues they arise from [40].

Epithelial cancers:

- Carcinoma: they arise from epithelial cells and represent ~80% of human tumors.
- Adenoma/Adenocarcinoma: they arise from epithelial specialized cells that secrete substances into the ducts or cavities that they line (lung, colon, breast, pancreas, stomach, prostate, ovary…). When the adenoma becomes malignant (invasive) is termed as adenocarcinoma.
- Squamous cell carcinoma: they arise from epithelial cells forming a protective cell layer (skin, esophagus…).

Non-epithelial cancers:

- Sarcoma: tumors arise from connective tissue and mesenchymal cell types (fibroblasts, adipocytes, osteoblast, myocytes…). They represent ~1% of the tumors.
- Tumors derived from the hematopoietic tissue:
    - Leukemia: arising from hematopoietic cell lineages that move freely (T and B lymphocytes)
    - Lymphoma: tumors of the lymphoid lineage (T and B lymphocytes) that aggregate to form solid tumors, usually found in lymph nodes.

- Neuroectodermal tumors: they have their origin in the central and peripheral nervous system and comprise around 1.3% of all cancers. They arise from glial cells (gliomas and glioblastomas), primitive nerv cells that remain in the body (neuroblastomas), Schwann cells (schwannomas) or immature or embryonal cells in brain and cerebellum (medulloblastomas).
- Other types of tumors: those formed from cells derived from the embryonic neural crest. For example, melanomas and small-cell lung carcinoma.

2.1.3 Incidence

Cancer is a major disease burden worldwide, with approximately 14 million new cases per year in 2012, a number estimated to reach 22 million within two decades. The cancer-related deaths are estimated in 8.2 million and expected to increase to 13 million per year within the same period. Globally, in 2012 the most common cancers diagnosed were: lung cancer (1.8 million cases, 13.0% of the total), breast cancer (1.7 million cases, 11.9%), and colorectal cancer (1.4 million cases, 9.7%). The most common causes of cancer death were: lung cancer (1.6 million deaths, 19.4% of the total), liver cancer (800,000 deaths, 9.1%), and stomach cancer (700,000 deaths, 8.8%). More than 60% of world's total new annual cases occur in Africa, Asia, Central and South America. These regions account for 70% of the world's cancer deaths, mainly due to the lack of early detection and access to treatment [41].

In the case of Europe, 3.4 million new cases were diagnosed in 2012 (53% in men, 47% in women). The most common cancer sites were breast cancer (464,000 cases, 13.5% of the total), followed by colorectal cancer (447,000, 13.0%), prostate cancer (417,000, 12.1%) and lung cancer (410,000, 11.9%). The estimated total number of cancer deaths was 1.75 million (56% in men, 44% in women). The most frequent cause of death per cancer site was: lung cancer (353,000 deaths, 20% of the total), colorectal cancer (215,000 deaths, 12.2%), breast cancer (131,000 deaths, 7.5%) and stomach cancer (107,000 deaths, 6.1%) [42] (Figure 8).

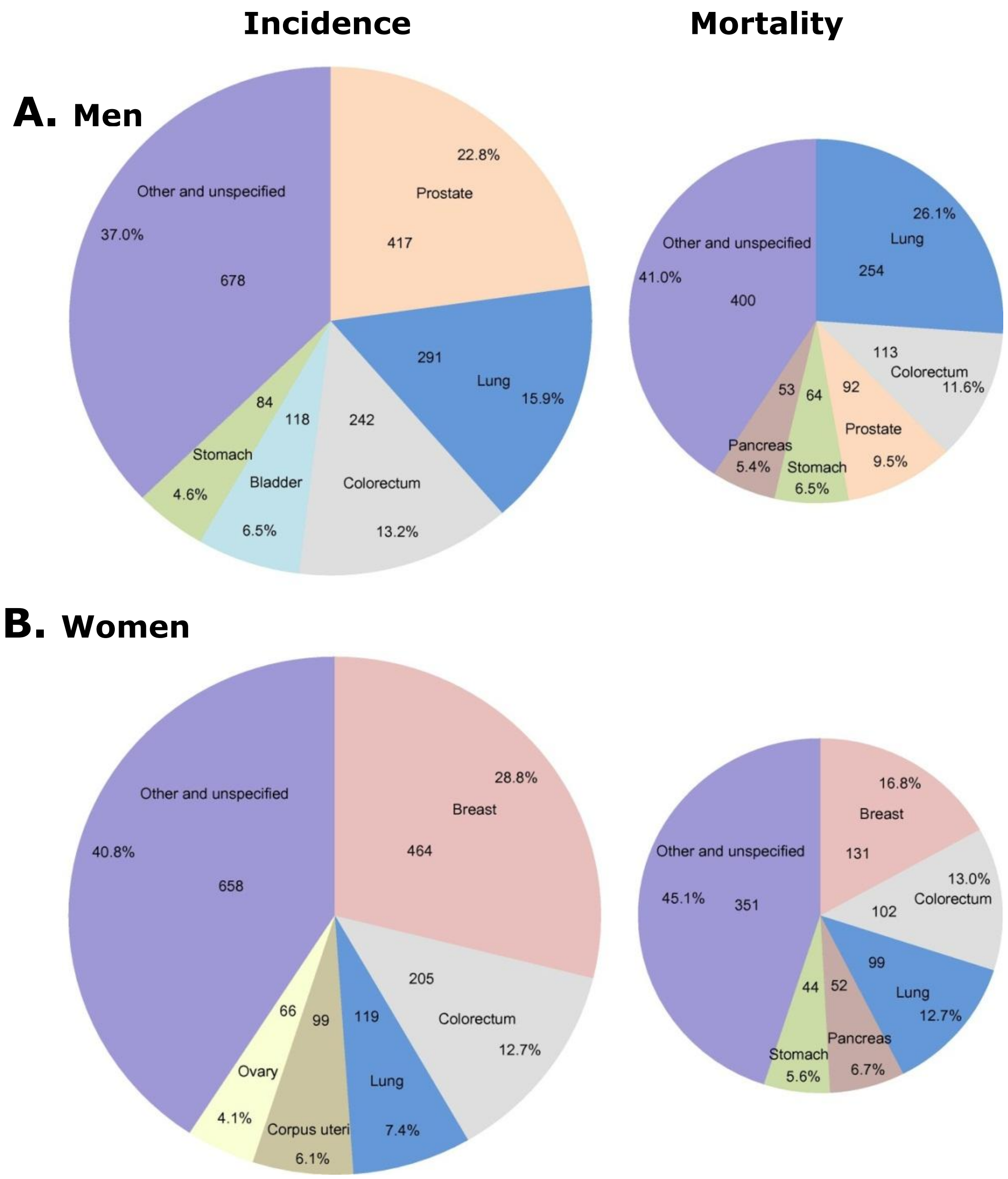

Figure 8. Distribution of the estimated cases and deaths for the five most common cancers in Europe 2012. (A) The most common primary sites in men were prostate (22.8% of the total), lung (291,000, 15.9%), colorectal (242,000, 13.2%) and bladder (118,000, 6.5%). B) In women, breast (28.8% of the total), followed by colorectal (205,000, 12.7%), lung (119,000, 7.4%) and corpus uteri (99,000, 6.1%) cancers. Obtained from Ferlay *et al.* 2013 [42].

Some of the many different types of human cancers seems to appear by random genetic accidents and thus with comparable frequencies in different human populations. This fact is true for pediatric tumors. However, other factors must intervene, explaining the high total number of cancer cases diagnosed per year. These other contributing factors are heredity and environment. Different human populations may carry cancer-susceptibility alleles that contribute to cancer at different frequencies, however, the environment in which people live is which definitely marks the disease incidence rates. Thus, the air that we breathe, the water, diet and lifestyle are extremely important determinants that contribute to the disease [40]. Tobacco consumption is the most important risk factor for cancer, causing 30% of all malignant tumors and around 70% of global lung cancer deaths. Infections by *Helicobacter pylori*, human papillomavirus (HPV), hepatitis B/C virus (HBV, HCV), and Epstein-Barr virus (EBV) were attributed to 15.4% of new cancer cases in 2012. Alcohol drinking, environmental pollution, radiation, immunosuppression among many others are also important cancer causing factors [41,43].

2.1.4 Hallmarks of cancer

Along the evolution process that takes place from a normal cell to a neoplastic state, cancer cells need to acquire some new capabilities that transform them into tumorigenic and eventually malignant. Hanahan and Weinberg [44,45] have grouped these capabilities into different "hallmarks of cancer". Each of them is explained below.

1. **Sustained proliferative signaling:** the production of growth-promoting signals by a tissue is tightly regulated, which ensures its normal homeostasis and architecture. During cancer development, cancer cells are able to deregulate these signals acquiring a phenotype of uncontrolled self-sustained proliferation. Many of these growth-promoting factors bind to membrane receptors with intracellular tyrosine kinases domains that transmit the signal. In many cases, the expression of these receptors is upregulated in cancer cells, making them hyperesponsive to a limited amount of growth factors. Alternatively, these receptors can be mutated,

either in the receptor itself or in a downstream effector, which finally leads to a constitutive activation of the pathway. Cancer cells are also able to produce growth factors themselves (autocrine stimulation), or even induce stromal cells to do it [44,45].

2. **Evade growth suppressors:** cancer cells also bypass many programs that negatively regulate cell proliferation, usually by inactivating tumor suppressor genes such as the ones encoding the cell-cycle gatekeepers retinoblastoma (Rb) and *TP53*. Contact inhibition programs are also abolished in many types of cancer cells [44,45].

3. **Resisting programmed cell death (apoptosis)**: apoptosis represents a tightly regulated mechanism in which the cells receiving extracellular and/or intracellular death-inducing signals are progressively disassembled and eliminated. This mechanism is orchestrated by a series of sensors and effectors, usually misregulated in cancer cells. The most commonly pro-apoptotic sensor is TP53, which is lost in more than 50% of the human cancers. This results in the removal of a key DNA damage sensor, which would normally initiate an apoptotic cascade [44,45].

4. **Enabling replicative immortality**: normal cells are able to pass through a limited number of successive cell growth-and-division cycles. The telomeres, tandem hexanucleotide repeats that protect the ends of chromosomal DNAs, from end-to-end fusions and shorten progressively on each cycle. Cells finally entered in a senescence state and apoptosis. To avoid this process, cancer cells express telomerase, a specialized DNA polymerase that adds hexanucleotide repeats onto the ends of telomeric DNA. Telomerase is expressed in about 90% of cancers [44,45].

5. **Induced angiogenesis:** tumors, as highly metabolic masses of cells, need support in the sense of nutrients, oxygen as well as the ability to evacuate carbon dioxide and metabolic waste. During tumor development, cancer cells are able to induce the formation of new vasculature (vasculogenesis) that spreads around the neoplastic growth (angiogenesis). This process is triggered by the production of many angiogenic factors such as vascular endothelial growth factor-A (VEGF-A), angiogenesis inhibitor thrombosporin-1 (TSP-1) and fibroblast growth factor (FGF). Some of these factors such as VEGF-A can be upregulated by hypoxia [44,45].

6. **Activating invasion and metastasis:** This complex process implies local migration and invasion of cancer cells, then intravasation into nearby blood and lymphatic vessels, transit through the lymphatic and hematogenous systems, followed by escape of cancer cells from the lumen of such vessels into the parenchyma of distant tissues (extravasation), formation of small nodules of cancer cells (micrometastases), and finally the growth into macroscopic tumors (metastasis or secondary tumors). This process represents the essence of cancer disease since metastasis are responsible of more than 90% of all cancer-related deaths. At the molecular level it is controlled by two main mechanisms: epithelial-mesenchymal transition (EMT) by which transformed epithelial cells dedifferentiate, invade and disseminate; and mesenchymal-epithelial transition (MET), the reverse process, by which cancer cells form new colonies with similar histopathology to those in the primary tumor [44,45].
7. **Genome instability and mutation:** tumor progression can be understood as the successive expansion of clonal populations that acquire new mutant genotypes. The accumulation of mutations is accelerated by compromising the surveillance systems that monitor genomic integrity and force genetically damaged cells to apoptosis, for example *TP53*. Other caretakers of the genome are usually affected in cancer cells including DNA reparation machinery or proteins involved in early detection and elimination of mutagenic molecules [44,45].
8. **Tumor-promoting inflammation:** neoplastic lesions are usually infiltrated by immune cells which constitutes an attempt of the immune system to eradicate the tumor. However, during recent years many studies have shown how inflammatory responses could enhance tumorigenesis and help tumor progression. Inflammation could contribute to this process by supplying growth, surviving and angiogenic factors, inducing EMT, producing extracellular-modifying enzymes that facilitate migration and invasion as well as generating reactive oxygen species (ROS) that would contribute to the tumoral genetic instability [44,45].
9. **Reprogramming energy metabolism:** active cell proliferation with large-scale biosynthetic programs requires great amount of ATP and high intake of glucose. Cancer cells are able to upregulate glucose transporters

such as GLUT1 and some glycolytic enzymes. Moreover, many cancer cells within a tumor grow under hypoxic conditions, where glucose catabolism in the mitochondria cannot be carried out. Cancer cells have adopted some mechanisms to face this situation, for example switching their metabolic processes to an anaerobic catabolism, favoring glycolysis. This phenomenon was first observed by Otto Warburg in 1924 and it is now known as "Warburg effect" [44–46].

10. **Evading immune destruction:** immune surveillance is responsible for recognizing and eliminating the vast majority of nascent tumors and constitutes a significant barrier to tumor formation and progression. Cancer cells are able to evade immune destruction by disabling components of the immune system and the molecular mechanisms that modulate this response are been clarified during the last years. This field is currently subjected to intense research since such molecular mechanisms could be used as therapeutic targets (immunotherapy) [44,45].

1.3.4 Oncogenes and Tumor suppressor genes

Tumors evolve from benign to malignant lesions by acquiring a series of mutations over time. This process is largely driven by mutations in two types of genes: oncogenes and tumor suppressor genes.

Oncogenes - "Proto-oncogenes" are normal cellular genes whose products are involved in growth-regulation. Once these genes are mutated and transformed into active "oncogenes" they can drive the cancerous growth of the cell. Mutation of one allele is enough to trigger this process. Different regulatory or structural alterations are responsible for this transformation, which in general represents a gain-of-function/activation [40]:

1. **Gene amplification**: some cancer cells show amplification of specific DNA regions that contain a proto-oncogene. The result is an increase in the overall levels of expression (overexpression) and the subsequent deregulation of the process where it participates. A clear example is found with the epithelial growth factor receptor 2 (*HER2*): the chromosome region

17q21, where it is located, is amplified in 30% of human breast cancers and associated with poor prognosis.

2. **Gene translocation:** a large chromosomal sequence containing a proto-oncogene can be translocated to a different genomic region causing deregulation/overexpression of some genes. For example, *c-MYC* deregulation in Burkitt's lymphoma is consequence of its translocation.

3. **Promoter alterations:** Point mutations, deletions, or insertions in the promoter region of a proto-oncogene that lead to increased transcription.

4. **Structural alterations:** point mutations or deletions in the proto-oncogene that transform the structure of the protein to a constitutively active form. *RAS* proto-oncogene, which encodes for a signal transduction protein, is mutated in around 20% of human tumors. The derived RAS oncoprotein always carry specific aminoacid substitutions typically in residues 12, 13 or 61. In the case of epithelial growth factor receptor (EGFR), the presence of a premature STOP codon originates a truncated form of the receptor active in the absence of ligands.

Tumor suppressor genes - these genes generally encode proteins that inhibit cell proliferation. In this case, mutations cause loss-of-function/inactivation of the protein and typically both alleles need to be targeted. The most common tumor suppressor genes are those controlling cell cycle (i.e. cycline-kinase p16), check-point control proteins that arrest the cell cycle if DNA damage or chromosome abnormalities are detected (i.e. *RB*, *TP53*, *ATM*, *ATR*), receptors for specific factors that inhibit cell proliferation (transforming growth factor beta (TGFβ) signaling) and proteins that promote apoptosis (i.e. *BAX*, *BAK*). They are known as "gatekeeper" genes and its mutation directly leads to cancer by allowing uncontrolled cell growth. The genes involved in the DNA reparation machinery do not directly regulate cell proliferation but are also frequently mutated somatically in cancer cells or the germ line of patients predisposed to cancer. These genes are responsible for keeping other genes healthy (i.e. suppressing mutation) and are commonly known as "caretaker" genes. Its inactivation accelerates the acquisition of mutations in other tumor suppressor genes or oncogenes and triggers aberrant mitosis and chromosomal rearrangements, promoting cancer [40]. Genes such as *BRCA*, *MLH1* and *MSH2* are included here.

As diploid organisms, a mutation occurring in a tumor suppressor gene does not significantly affect its function since the remaining copy is not altered. The "loss of heterozygosity" (LOH) process implies a hit in the second allele and the complete inactivation of the gene, which eventually promotes cancer. There are many mechanisms by which the second copy can be lost including mutations, mitotic recombination, non-homologous recombination and promoter methylation [40].

2.2 Colorectal cancer

2.2.1 Incidence, survival and risk factors

Colorectal cancer (CRC) is the **third most common type of cancer worldwide**, with 1.4 million cases (9.7% of the total) as estimated in 2012 and approximately half of the patients die because of the disease. It is more prevalent in developed countries with a Western culture, ranging from more than 40 cases per 100,000 people in the United States, Australia, New Zealand and Western Europe to less than 5 cases per 100,000 in Africa and Asia. In **Europe** in 2012, it was the **second most frequent type of cancer** (13% of total; 13.2% in men and 12.7% in women) and the **second cause of death** (12.2% of total) [36,37,41] (**Figure 8**).

CRC survival highly depends on the stage of disease, thus the earlier the stage at diagnosis the higher the chance of long-term survival. It ranges from a 90% 5-year survival rate for cancers detected at the localized stage; 70% for cancers with regional dissemination; to 10% for people diagnosed for distant metastatic cancer [47] (**Table 1**).

More than 90% of CRCs occur in people aged 50 or older although its incidence appears to be increasing among younger people. The causes of CRCs involve; inherited genetic risks, high fat diets, red meat consumption, diet low in fruits and vegetables, physical inactivity, excess bodyweight and tobacco and alcohol consumption [47].

2.2.2 Origin and classification of colorectal cancer

The normal intestinal epithelium is controlled by a tight balance of proliferation, differentiation, migration and cell death. Tumorigenesis occurs when these mechanisms become deregulated resulting in hyperproliferation and/or loss of differentiation. This leads to epithelial hyperplasia and the formation of aberrant crypt foci that evolve into benign gastrointestinal lesions termed **adenomas** or **adenomatous polyps**. Over the course of several years, the hyperplastic lesion becomes increasingly dysplastic, developing malignant tumors or **carcinomas** [48]. The origin of the cell from which the initial adenoma arises is still under discussion. Two different models have been proposed (**Figure 9**): a **"bottom-up"** model where a mutant cell in stem cell compartment migrates to the crypt apex where it expands and a **"top-down"** model where mutant cells appear in the intracryptal zone and, as the clone expands, cells migrate laterally and downwards to displace the normal epithelium of adjacent crypts [49–51] (**Figure 9**). Evidence for the "bottom-up" model have received genetic support as intestinal ISCs-specific deletion of the CRC driver gene *Apc* in mice lead to the rapid development of a full adenoma [22]. Furthermore, in a fast renewing organ such as human gut epithelia, stem cells are the only cells that persist long enough in the tissue to undergo the prolonged sequence of successive mutation and selection that carcinogenesis requires [21]. On the other hand, inflammatory signaling has been related to the dedifferentiation of intestinal epithelial cells and generation of tumor-initiating cells *in vivo*, supporting the "top-down" model [52]. However, deletion of *Apc* in differentiated cells only resulted in sporadic and slow-growing adenomas in a different study [22]. In summary, the origin of CRC is not clear yet. Current research tends to favor a 'bottom-up' mechanism but evidences for the "top-down" model has also been found.

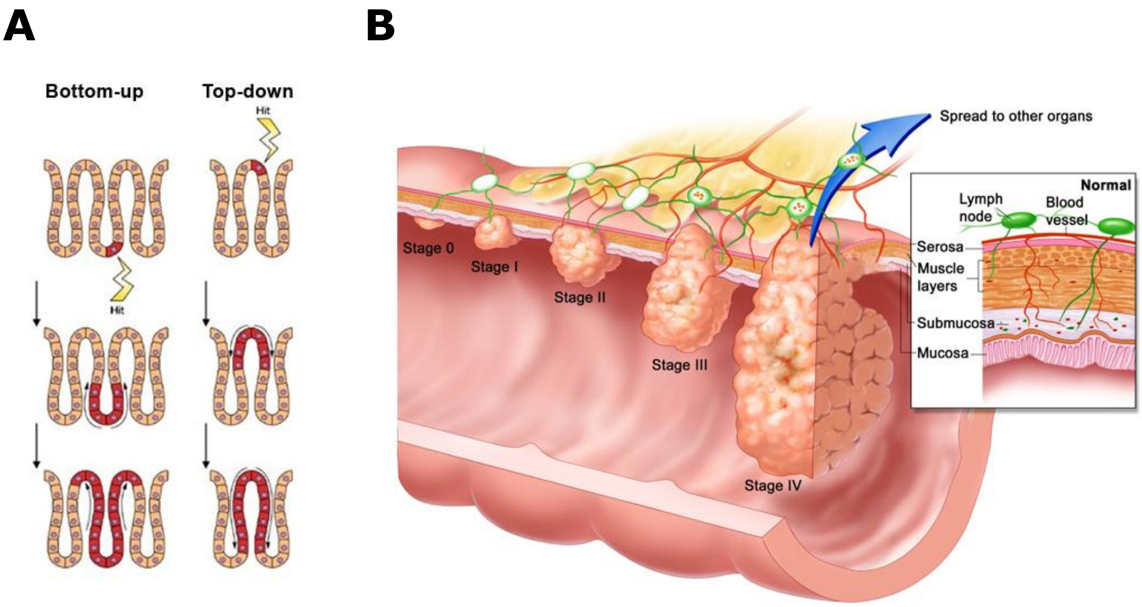

Figure 9. From a polyp to metastatic tumor. (A) "Bottom-up" model includes the spread of dysplastic cells initiated at the base of the crypt within the stem cell zone, and continues upward. "Top-down" model, which suggests that a mutation resulting in the appearance of a dysplastic cell can occur at, or near, the top of the crypt. Modified from McDonald *et al*. **(B)** Stage 0 or carcinoma *in situ*, abnormal cells are found in the mucosa of the colon wall; Stage I, cancer has spread from the mucosa to the submucosa and/or the muscle layer of the colon wall. Stage II, tumors have spread through the muscle layer of the colon wall to the serosa. Stage III, cancer has invaded the mucosa, submucosa and to nearby lymph nodes. Stage IV, the cancer has metastasized other organs, commonly lung and liver. Image taken from the Terese Winslow US Govt.

Staging of colorectal cancer indicates how far the disease has spread. The first stage classification was postulated by Dr. Cuthbert Dukes in 1932 and is known as **Dukes staging**. The different stages are: **"Dukes A"** indicates that the cancer is only affecting the innermost lining of the colon or rectum or slightly growing into the muscle layer of the colon or rectum; **"Dukes B"** the cancer has grown through the muscle layer of the colon or rectum; **"Dukes C"** cancer has spread to at least one lymph node in that area; **"Dukes D"** the cancer has spread to distant organs in the body, commonly liver or lungs. More recently, the American Joint Committee on cancer (AJCC) and the International Union against Cancer proposed the **TNM staging** system (**Table 1**). This system provides 3 key pieces of information: **"T"** describes how far the main (primary) tumor has grown into the wall of the intestine and whether it has grown into nearby areas; **"N"** describes the extent of spread to regional lymph nodes; **"M**" indicates whether the cancer has spread (metastasized) to other organs of the body.

The letter X means "cannot be assessed because the information is not available". The numbers appearing after this letter (from 0 to 4) serve to indicate increasing severity (**Table 1**). Once the TNM categories have been determined, usually after surgery, this information is combined in a process called stage grouping. The stage is expressed in Roman numerals from stage I (the least advanced) to stage IV (the most advanced)[53,54].

Table 1. TNM staging system for CRC and survival rates for different stages. Obtained from Weitz *et al*. 2005 [55].

T-primary tumor	
Tx	Primary tumor cannot be assessed
T0	No evidence of primary tumor
Tis	Carcinoma in situ: intraepithelial or invasion of lamina propia
T1	Tumor invades submucosa
T2	Tumor invades muscularis propia
T3	Tumor invades through the muscularis propia into subserosa
T4	Tumor directly invades other organs or structures and/or
N-regional lymph nodes	
N0X	Regional lymph nodes cannot be assessed
N0	No regional lymph node metastasis
N1	Metastasis in 1 or 3 regional lymph nodes
N2	Metastasis in 4 or more regional lymph nodes
M-distant metastasis	
MX	Distant metastasis cannot be assessed
M0	No distant metastasis
M1	Distant metastasis

Stage	**T**	**N**	**M**	**5-year overall survival**
Stage I	T1,	N0	M0	80-95%
Stage IIA	T3	N0	M0	72-75%
Stage IIB	T4	N0	M0	65-66%
Stage IIIA	T1,	N1	M0	55-60%
Stage IIIB	T3,	N1	M0	35-42%
Stage IIIC	Any	N2	M0	25-27%
Stage IV	Any	Any	M1	0-7%

The tumor is also categorized depending on its **histological grade**, which is known to be of prognostic significance. It describes how closely the cancer resembles normal colorectal tissue when looked under the microscope. The grading scale goes from: G1 (well differentiated, the histology of the tumor looks similar to normal tissue; low grade); G2 (moderately differentiated; intermediate grade); G3 (poorly differentiated; high grade); G4 (undifferentiated, the histology of the tumor looks very different respect to the tissue where it was originated). Low-grade cancers are less aggressive than high grade cancers, and indicates a better prognostic [53].

2.2.4 The distinct paths of colorectal cancer

It has been estimated that 15-30% of CRC cases may have a hereditary component, given the occurrence of CRC in first- or second-degree relatives. Approximately one-quarter of these familial cases (<5% of all CRC cases) occur in a setting with family history and/or clinical features that indicate a highly penetrant, Mendelian cancer syndrome that predisposes to CRC. The majority of these highly penetrant cases are **hereditary nonpolyposis colorectal cancer (HNPCC)** or Lynch syndrome, characterized by germ line mutations in the mismatch repair (MMR) genes, usually *MLH1* or *MSH2*. These patients have a lifetime risk of CRC of almost 100% by the age of 40 years, on average. Another subset of patients is associated with familial **adenomatous polyposis (FAP)** defined by germ line *APC* mutations that originates multiple adenomatous polyps (>100) and carcinomas of the colon and rectum, MYH-associated polyposis and Hamartomatous polyposis syndrome [59–61]. The remaining CRC cases (70-85%) originate from sporadic mutations that underlie the three different pathways above mentioned: MSI, CIN and CIMP. They are schematized in **Figure 11**.

1. Microsatellite instability (MSI) – DNA mismatch repair defects in colorectal cancer

Microsatellite instability is the molecular fingerprint of a deficient MMR system. Microsatellites are repetitive sequences (from mono to hexanucleotides) distributed throughout the human genome. These sequence motifs are especially prone to accumulation of mutations like mismatches, insertions or deletions, mainly because DNA polymerase slippage during replication of these repetitive sequences. The MMR is responsible of the detection and correction of these errors introduced during DNA replication. It includes MLH1, MSH2, MSH3, MSH6 and PMS2 proteins that in eukaryotes act as heterodimers: MSH2 and MSH6 recognize 1bp mismatches and 1bp insertion/deletion mutations; MSH2 and MSH3 recognize 1bp, 2bp and 4bp insertion/deletion mutations; MSH4 and MSH5 participate in the regulation of meiotic recombination. Upon recognition of DNA mismatches, members of the MLH and PMS protein families are recruited, triggering a cascade of events that lead to the excision of the DNA strand carrying the mismatched base, which culminates in DNA resynthesis and ligation [59,62]. Alteration of microsatellite sequences in the tumoral DNA was first reported for HNPCC patients, and was later related with germ line MMR mutations (primarily MLH1 and MSH2) [60]. This phenotype was ultimately termed the microsatellite instability (MSI) phenotype.

Somatic inactivation of MMR genes occurs mainly by MLH1 promoter hypermethylation (~83% of the cases) whereas the rates of LOH and somatic mutation of *MLH1* are 24% and 13%, respectively. The prevalence of MSI in sporadic colorectal cancer is approximately 15%, being more common among stage II (~20%) than stage III (~12%) and even less frequent among stage IV (~4%) [62,63]. Tumor suppressor genes such as transforming growth factor β (*TGF-β*) receptor type II (*TGFBR2*), BCL2-associated X protein (BAX) and brush border myosin IA (*MYO1A*) can be also inactivated in MSI tumors by accumulation of mutations in coding microsatellites [64].

MSI tumors tend to be right-sided in the colon, show high histological degree and display mucinous phenotype. They are diagnosed at early stages and show good prognosis and reduced likelihood of metastasis compared to CIN tumors, which highlights the value of MSI as prognostic marker [62,65].

2. Microsatellite stable (MSS) – chromosomal instability (CIN)

The majority of sporadic colon cancers (85%) are proficient in DNA MMR but show another form of genomic instability at the gross chromosomal level (arm deletions, insertions and translocations) which includes frequent loss of chromosomes 18q and 17p as well as gains of chromosomes 8q, 13 and 20q. It is known as chromosomal instability (CIN). CIN represents the end of a number of processes, including mutations in mitotic checkpoint genes, microtubule spindle defects, and telomere dysfunction that finally lead to an abnormal alignment and segregation of chromosomes during mitosis explaining the abnormal karyotype found in CIN tumors [59,60,66].

The multistep model of adenoma-carcinoma progression proposed by Fearon and Vogelstein two decades ago outlines the contribution of somatic mutation events to the pathogenesis of CRC and is still a reference model to study the development of CIN tumors [60,62]. In fact, couple with the karyotipic abnormalities observed in some oncogenes (*KRAS*, 12p) and tumor suppressor genes (*APC*, 5q; *SMAD4*, 18q and *TP53*, 17p) is the accumulation of mutations (*KRAS*, mutated in 35-45% of CRC tumors; *APC*, 85% of CRC tumors; *SMAD4*, 10-35% of CRC tumors; *TP53*, 35-55% of CRC tumors) [33,64] that constitute a second hit which coupled with the chromosomal defects observed in this type of CRC are capable of inactivating tumor suppressor genes and activating oncogenes [64].

3. CpG island methylator phenotype (CIMP) - Epigenetic changes

Epigenetic silencing of genes, mostly mediated by aberrant DNA methylation, is another mechanism of gene inactivation in patients with colorectal cancer and it is known as **CpG island methylator phenotype (CIMP)**. In CRC cells there is an overall decrease in the total level of DNA methylation (hypomethylation) compared to normal tissues, and DNA hypomethylation is also observed in adenomatous polyps. However, CpG islands at various promoters show increased methylation which is often linked to transcriptional silencing of the gene [60,64]. One example was already given in MSI colorectal cancer where somatic epigenetic silencing blocks the expression of MLH1 and highlights a clear connection between MSI and CIMP phenotype. *BRAF* mutations is another event that appears early in the progression of CIMP tumors [67,68]. The molecular mechanisms responsible for CIMP remains still under study but two possibilities have been proposed. Hypermethylation could arose from selective advantage conferred by silencing of multiple different genes as observed for the tumor suppressor gene Hypermethylated in Cancer 1 (*HIC1*) or the Wnt secreted antagonists known as secreted-Frizzled-related proteins (SFRPs)[69]. On the other hand,

2.2.5 Molecular pathways in colorectal cancer – oncogene and tumor suppressor genes mutations

Colorectal cancers acquire many genetic changes during its development (**Figure 12**). *APC* inactivation is viewed as an early and probably the initiating event in ~70-80% of colorectal adenomas but other somatic defects need to promote further growth and transformation of the adenomas to carcinomas. As previously mentioned, cancer is a microevolutionary process where only specific clones with gene defects promoting key roles in tumor initiation, progression and/or maintenance are selected. In cancer, these genes are termed drivers. In contrast, a so-called passenger gene defect might simply have arisen coincident with a driver alteration [60].

Briefly, more than 80 somatic mutations in exons can be found in a given primary CRC. Examining the overall distribution of these mutations in a large proportion of tumors we only found a handful of commonly mutated genes, called "mountains" and a large number of infrequently mutated genes, "hills" [71]. On the bases of such statistical analysis, Wood *et al.* [71] predicted that only ~15 or fewer of the 80 somatic mutations in any given CRC are critical drivers of tumor initiation, progression, and/or maintenance. Defining these key driver genes and the pathways where they are enrolled is of great importance to better understand the molecular basis of carcinogenesis. In the case of colorectal cancer, the "mountains" account for the inactivation of the *APC*, *TP53*, components of the *TGFβ* pathway tumor suppressor genes and for the activation of *KRAS*, *BRAF* and *PI3K* oncogenes (**Figure 12**) [57,60,64,71,72].

***APC* -** Wnt signaling pathway activation is considered as the initiating event in most sporadic CRC and is responsible of familial adenomatous polyposis (FAP), an inherited cancer prone condition in which numerous polyps are formed in the epithelium of the large intestine [73]. The most common mutation in colorectal cancer inactivates both copies of the gene that encodes the APC protein, and it is observed in 70-80% of sporadic colorectal tumors (**Figure 12**). In the absence of functional APC the coordinated phosphorylation and destruction of β-catenin are disrupted. Thus, β-catenin accumulates in the cytoplasm, complexes with DNA-binding proteins of the TCF/LEF family and translocates to the nucleus activating the expression of many genes. As a result Wnt signaling is inappropriately and constitutively activated [60,64,72,74]. Moreover, it has also been demonstrated that APC truncation acted dominantly to interfere with micro-tubule plus-end attachments and to cause a dramatic increase in mitotic abnormalities. Thus, cancer cells with APC mutations have a diminished capacity to correct erroneous kinetochore-microtubule attachments which would account for the wide spread occurrence of CIN in tumors [75].

Other proteins participating in the Wnt signaling pathway are also found mutated in colorectal tumors. Approximately 48% of the tumors with wild-type APC show activating mutations in *CTNNB1* gene, encoding β-catenin [76,77]. Axin inactivation has also been found in CRC cell lines and tumors [78,79] and are associated with MSI tumors [80].

***KRAS* and *BRAF* -** Oncogenic mutations of *KRAS* and *BRAF*, which activate the mitogen-activated protein kinase (MAPK) signaling pathway, are also common in CRC (**Figure 12**). KRAS somatic mutations are found in approximately 40-50% of CRCs and mainly affects codon 12, 13 and 61, originating a constitutively active form of the protein. *KRAS* mutations do not contribute for the adenoma initiation but are important for tumor progression: around 10% of adenomas smaller than 1 cm show *KRAS* mutations whereas *KRAS* mutations are observed in 40% to 50% of adenomas greater than 1 cm with a higher degree of dysplasia [60,64,81]. BRAF, a protein kinase directly activated by RAS is mutated in approximately 5–10% of CRCs. *BRAF* mutations are more frequent in those tumors with CIMP phenotype [58,64,82].

Phosphatidylinositol 3-kinase (PI3K) - PI3K is activated by receptors tyrosine kinases and catalyzed the phosphorylation of phosphatidylinositol-4,5-biphosphate (PIP2) to phosphatidylinositol-3,4,5-triphosphate (PIP3), a key second messenger with effects on cell growth, proliferation and survival. Around 15%-25% of CRCs bear activating somatic mutations in *PIK3CA* gene which encodes for the catalytic subunit, originating an increased production of PIP3 (**Figure 12**). The PI3K kinase signaling can be antagonized by tumor suppressor phosphatase and tensin homolog (PTEN), a phosphatase that transforms PIP3 to PIP2. Mutations in *PTEN* are observed in ~10% colorectal cancers. Amplification of insulin receptor substrate 2 (*IRS2*), an upstream activator of PI3K signaling, and coamplification of *AKT* and *PAK4*, downstream mediators of PI3K signaling are also found in CRC[60,64].

Transforming growth factor beta (TGFβ) pathway – TGFβ ligand binding to the TGFβ receptor mediates the phosphorylation of SMAD2 and SMAD3. Then, they translocate to the nucleus and complex to SMAD4 that regulates transcription of specific genes regulating growth, apoptosis and cellular differentiation. In CRC cells, inactivation of the pathway can occur by affecting it at different levels (**Figure 12**). Inactivating mutations in the TGF-β type II receptor (*TGFβIIR*) gene are found in ~25% of CRCs. The coding region of the *TGFβIIR* gene contains a long microsatellite sequence, and more than 90% of MSI CRCs harbor somatic insertion/deletion mutations in both alleles, leading to inactivation of TGFβIIR function [83]. In addition, ~15% of MSS CRCs also show inactivating mutations for *TGFβIIR*. *SMAD2* and *SMAD4* genes are located in chromosome 18q that shows LOH in around 70% of CRC tumors (~50% in large, late-stage adenomas; and fewer than 10% in small, early stage adenomas). The second copy is inactivated by mutations in ~10–15% of the tumors in the case of *SMAD4* and ~5% for *SMAD2*. Other studies show that mutations inactivating the *SMAD3* gene, mapping to chromosome 15 are found in ~5% of CRCs. Mutations that inactivate the TGF-β pathway are associated with the transition from adenoma to high grade dysplasia or carcinoma [58,60,64,72].

***TP53* -** The inactivation *TP53* is the second key genetic step in CRC (**Figure 12**). In most tumors, the two *TP53* alleles are inactivated usually by a combination of two mechanisms: 17p chromosome, where *TP53* locus

2.2.6 Colorectal cancer treatment

Surgery is the frontline form of therapy for CRC. In the case of rectum cancer, the standard surgical procedure is total mesorectal excision that removes both tumor and adjacent lymph nodes. Similarly, in colon cancer a portion containing the tumor and the corresponding lymph vessels are removed. The extent of surgery is predetermined by the tumor localization and the supplying blood vessels. Open surgery used to be the only option available; however, laparoscopic resection has developed as an alternative. **Neoadjuvant therapy** based on **radiotherapy** is commonly used in many rectal cancer patients and the goal is to reduce the tumor size before surgery [54,55]. After tumor resection, **adjuvant therapy** is applied to lower the risk of cancer recurrence and it is based on **chemotherapy**. In the case of patients with Stage I disease no further treatment in addition to surgery is use because the local recurrence rate is low (about 3%) and the benefit from the treatment is very small. Stage II patients are not routinely recommended for adjuvant therapy and every case needs to be evaluated. Patients with Stage III colon cancer have a risk of recurrence ranging between 15% and 50% and adjuvant therapy is recommended in all cases. In the case of Stage IV patients with metastatic colorectal cancer, **palliative chemotherapy** is used to improve survival and quality of life. Curative resection of metastatic lesions (usually in liver or lung) before and during chemotherapy is also used for these patients since it can lead to 5-year survival rates of 35–58%. In many cases, initially unresectable tumors become resectable after systemic chemotherapy [54,55].

The chemotherapeutic agents with approved use in CRC are:

1. **5-fluorouracil (5-FU):** a thymidylate synthase inhibitor that impairs DNA replication. It is often used in combination with folinic acid (leucovorin). Capecitabine is a modified form of 5-FU administrated orally with lower percentage of adverse effects.
2. **CPT-11 or Irinotecan**: a topoisomerase I inhibitor, affecting DNA replication and triggering cell death.
3. **Oxaliplatin**: a platinum-based agent that forms inter and intra strand cross-links in the DNA.

4. **Drug combinations**: **FOLFOX** (5-fluorouracil (5-FU), leucovorin, and oxaliplatin); **FOLFIRI** (5-FU, folinic acid and irinotecan); **FOLFOXIRI** (5-FU, folinic acid, oxaliplatin and irinotecan); **CapeOx** (Capecitabine and oxaliplatin).
5. **Targeted therapy**: some new agents have been approved during last years. These agents are monoclonal antibodies against VEGF (**Bevacizumab**) and EGFR (**Cetuximab and Panitumumab**), among others.

3. Myosins

3.1 The Myosin superfamily

Myosins are molecular motor proteins that use the energy of ATP hydrolysis to move along actin filaments. They constitute one of the largest and most divergent protein families in eukaryotes since some studies have separated them into 35 classes [85], based on head domain sequence similarities and domain organization. Nevertheless, two big groups of myosins can be established: **conventional myosins,** which group into filaments and include muscle and non-muscle myosin II (MYO2), and **unconventional myosins**, so called because they do not participate in muscle contraction and group into filaments. It includes the rest of myosin classes [86]. Many of these classes exhibit a broad range of phylogenetic expression: Myo3 and 6 are only expressed in metazoans; Myo8 and 13 are found only in plants; Myo10 and 16 are expressed only in vertebrates and the remaining classes have been identified in only one or a few related species (Myo4, 12, 14, 17) [85,87].

In general, myosins consist of long polypeptides known as the heavy chain that can function as monomers, dimers or oligomers (**Figure 13**). It comprises three different domains: the N-terminal region, **motor or head domain** that binds to actin in a ATP-dependent manner; a **neck region** that consists of an extended α-helical containing a variable number of IQ motifs which bind calmodulin or calmodulin-like light chains which provides rigidity. The neck domain is also known as the "lever arm" as it moves as a rigid body amplifying the conformational changes of the motor domain after ATP hydrolysis and generating a step movement. The C-terminal part contains the **tail domain** or globular cargo binding domain (CBD) which is the most variable part, both in length and composition, and determines the functional specificity of the motor [86–89]. The ability to polymerize resides on the tail domain, that in some cases contains heptad-repeated sequences that form helical coiled coils, allowing heavy chains to dimerize forming two-headed motors that can function as processive transporters. Other myosins do not contain coiled-coil motifs; they are single-headed mainly functioning as mechanical tethers [87,88]. In addition to dimerization motifs, myosin tails also contain some other conserved domains responsible for protein-protein interactions with specific cargo receptors and/or additional functions such as lipid binding or kinase activity [86,87]. The heavy chain structure of some myosins can be observed in **Figure 13**.

Another important feature to take into account is the directionality of the motors on its movement along the actin filaments which possess an inherent polarity showing a plus (barbed) and minus (pointed) end. Most of the myosins move towards the plus ends of actin filaments, however, this ability can be regulated as observed in MYO9B that may move towards both, plus and minus ends. MYO6 has been shown to be a minus-end-directed motor [87,90].

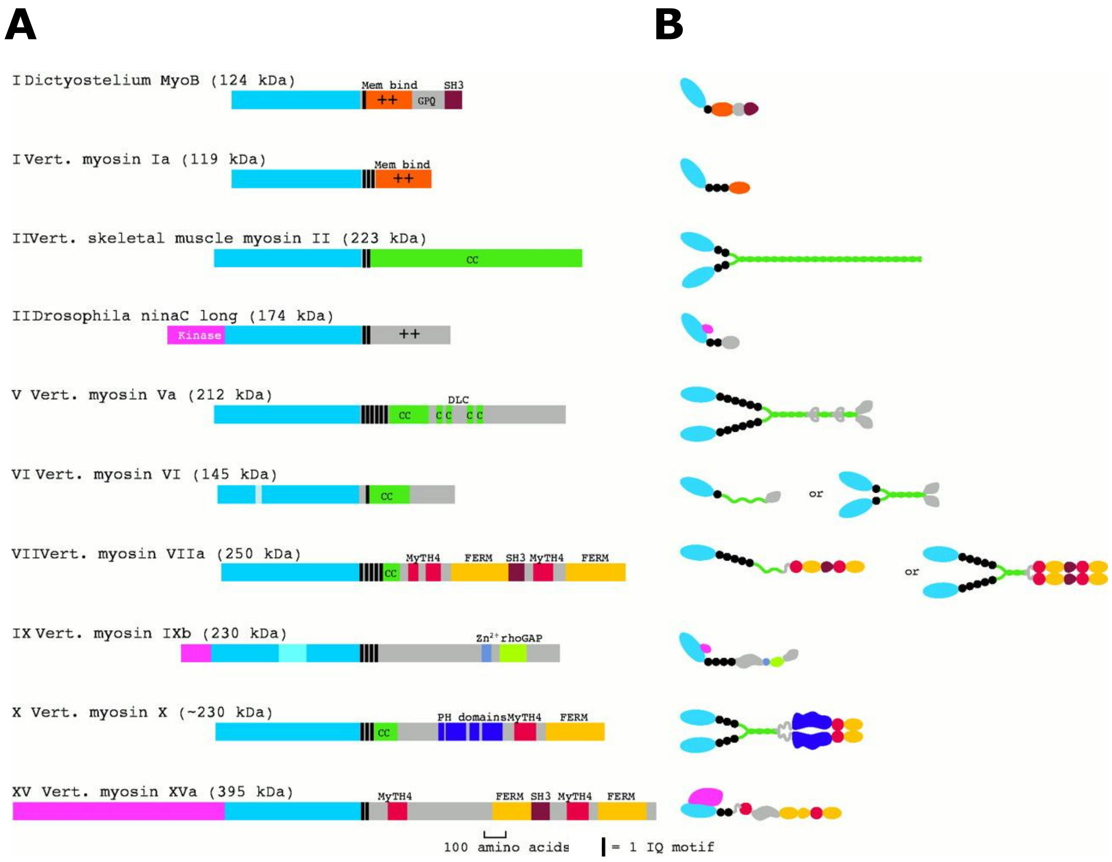

Figure 13. Myosin family of molecular motors. (A) Structure of the heavy chains of myosin classes. **(B)** Schematic representations of myosin structures. Class VI and class VII include myosins that may exist in both a dimeric and a monomeric form. Pink areas represent kinase domains. Source Krendel M. and Mooseker MS [87].

3.1.2 Functions and localization

Myosins are localized to different organs, cell types or intracellular regions based on their structural and functional peculiarities. Most of the myosins are cytoplasmic, where they usually localized to various specialized zones. Aditionally, some myosins also have nuclear localization. In any case, within a given cell multiple myosins are expressed, often showing overlapping subcellular localizations. They develop a wide variety of roles; some of them are described below and summarized in **Figure 14**.

Myosins in muscle contraction and cytokinesis - The first myosin was described in muscle extracts in 1864, now known as muscle myosin II or conventional myosin, and together with actin, make up the major contractile proteins of cardiac, skeletal and smooth muscle. Importantly, non-muscle myosin II molecules that resemble their muscle counterparts in both structure and function, are also present in all eukaryotic cells. Conventional MYO2 proteins contain long coiled-coil domains that allow multimerization. Dozens of myosin molecules are packed forming bipolar thick filaments that induce contraction by forcing two sets of actin filaments of opposite polarity to slide toward each other, causing shortening of the muscle fibers. Non muscle myosin II is also found in the division furrow of cells where, in a similar way, provides the force of contraction necessary to separate two daughter cells during cytokinesis [86,91].

Transport - As mentioned above, the myosin tail domains are the most divergent part, enabling motors to engage a broad range of different cellular adaptors and binding proteins. The interaction with a specific adaptor protein is generally responsible for the recruitment of the motor protein to a specific cellular compartment where it participates in many trafficking pathways and anchoring events [86] (**Figure 14**). One the most important interactors of different myosins are proteins from the Rab small GTPases family of the Ras superfamily, and their adaptor proteins [92,93]. One example is observed in melanocytes, where a complex containing MYO5A, RAB27A and the adaptor protein Slac2-a/melanophilin is involved in the transport of melanosomes (pigment containing vesicles) to the tips of dendritic extensions (dendrites) in these cells [94–96]. Another example is found in MYO19 which has been proposed to be responsible for mitochondria transport in mammalian neurons [97], or MYO6, that permits the correct targeting of megalin receptor to the base of the microvilli [98]. mRNA molecules can be also transported by myosin motor proteins as demonstrated by Gonsalvez *et al*. [99] in *Saccharomyces cerevisiae*, where MYO4P, a type V myosin, transports nearly 30 mRNAs from the mother cell to the tip of the bud.

Cell-signaling pathways - Myosins are also important players in cell signaling pathways and, in many cases, again through the interaction with Rab proteins. The most striking example is shown is Myo9b family, which contain an active GTPase activation domain (GAP) in their tail for the interaction with the G protein Rho [100]. Another example of the interaction with Rab proteins is observed in MYO5B. Its interaction with RAB11A controls ezrin phosphorylation and polarization in the enterocytes (described in more detail below) [101,102]. MYO5A has been shown to play a role in regulating apoptosis by binding proapoptotic protein BMF and sequesters it to actin filaments [103], and MYO3, and unusual myosin containing a protein kinase domain at its N-terminal region is involved in phototransduction in *Drosophila* [104].

Membrane trafficking - Myosins are also implicated in various types of membrane trafficking (**Figure 14**). Employing the actin filament cytoplasmic tracks, myosins carry out transport of endocytic and exocytic vesicles, local delivery of organelles and capture and retain organelles to specific subcellular regions [87]. In some cellular structures such as filopodia, microvilli or stereocilia, the plus end of the actin filament is orientated towards the membrane. Therefore, a specific plus-end directed myosin could participate in transport of vesicles or organelles to the membrane (exocytosis). On the other hand, a minus-end directed protein would participate in the transport of cargoes into the cell (endocytosis) or maintaining invaginations of the membrane [87,90]. As described above, MYO6 is a minus-end-directed motor and its role in endocytosis has been well characterized in various cell types. Whereas MYO6 in polarized epithelial cells associates with clathrin-coated vesicles [105], in nonpolarized cells MYO6 is recruited to endocytic nascent vesicles following the loss of clathrin coats, transporting them towards early endosomes with the help of various adaptor proteins [105].

Cell adhesion and migration - Non-muscle myosin II is an important regulator for cell migration and adhesion (**Figure 14**). Actin cytoskeleton reorganization and actomyosin contractility seems to constitute the main forces that control these processes. During cell migration, actin polymerizes in cellular lamellipodial protrusions on the leading edge of the cell and constitutes the force that powers cell movement. Although non-muscle myosin II does not play and important role in the physical organization of the lamellipodium, it may act in the directional coordination of the motility, preventing the formation of lateral lamellipodia. Non-muscle myosin II is also abundant in actin stress fibers in the rear of the cell, where it participates in the forward movement of the cell body and tail retraction [87,91] (**Figure 14**).

Actin-dependent motors also play an important role in cell adhesion (**Figure 14**). Transmembrane cell adhesion receptors (integrins for cell-extracellular matrix contacts and cadherins for cell-cell contacts) need to be linked to the actin cytoskeleton. This association is mediated by myosins that may bind to cell adhesion receptors transporting and clustering them to the actin-rich cortex. The concentration of adhesion receptors increases the strength of cell adhesion and activates intracellular signaling pathways that promote contact assembly [91,106]. Myosin motors are also involved in recycling of cell-adhesion receptors through their functions in end/exocytosis [107]. The role of myosins in cell adhesion has been well characterized for MYO7 and MYO10, both containing tail FERM domains (Band 4.1, ezrin, radixin, moesin) that mediate binding of cytoskeletal proteins to cytoplasmic domains of transmembrane proteins [87,89]. In addition, MYO6 functions are important for maintaining the integrity of cell monolayers and cell shape, possibly due to its role in regulation of E-cadherin stability through endocytosis [108].

Roles in protein, RNA and organelle localization - Myosin motor proteins are involved in determining intracellular localization of membranous and non-membranous organelles, protein complexes and RNA [87]. For example, myosin XVIIIA has been studied for its role in Golgi complex organization in HeLa cells where it anchors the membranous organelle to actin filaments [109]. Myo5 is localized in the centrosome, where it is proposed to facilitate chromosomal segregation in yeast [110]. MYO5A, previously mentioned for its role in transporting melanosomes, could also act tethering them to the tips of dendrites [94,111]; and MYO1A, a major protein of the intestinal brush border interacts and localizes disaccharides sucrose isomaltase to the microvilli [112]. Moreover, there are a number of myosins suggested to function during transcription within the nucleus by facilitating RNA polymerase movement, like myosin I [113], myosin II [114], and myosin VI [115]. The role of unconventional motors in RNA transport and localization was mentioned above.

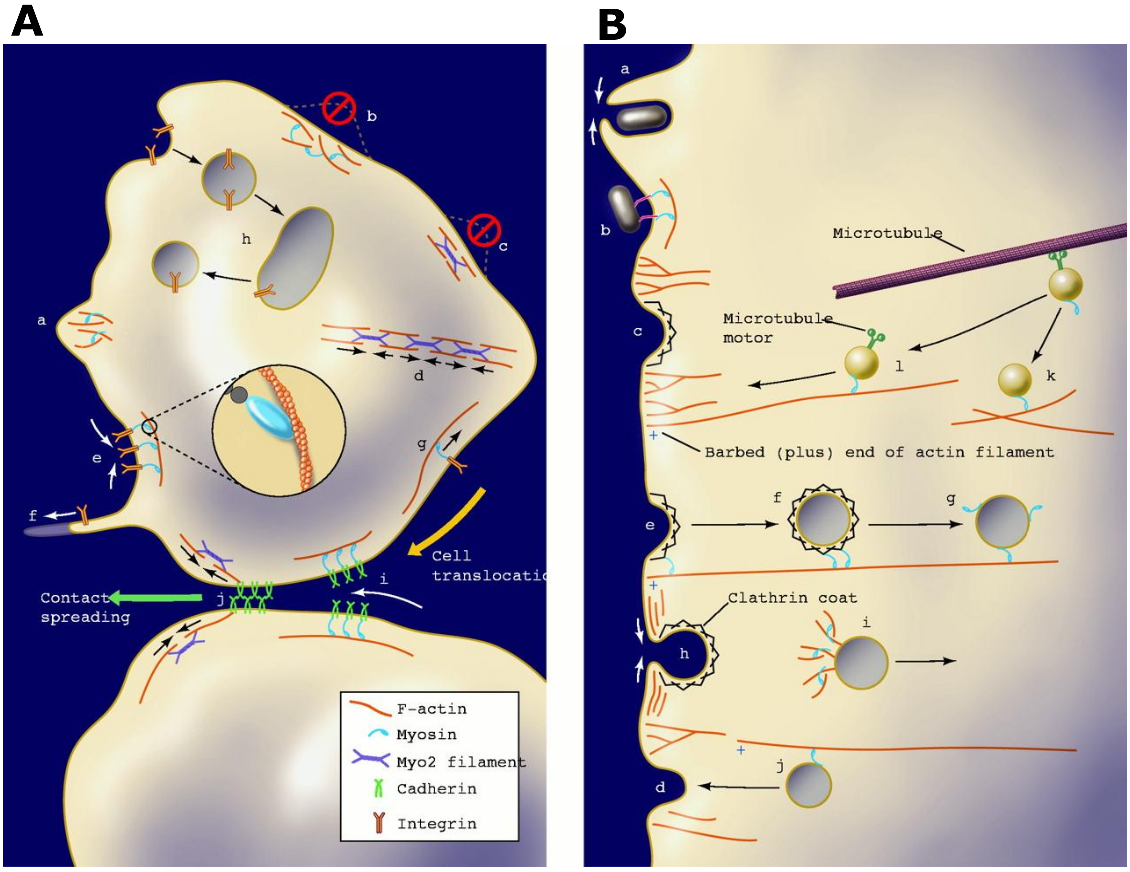

Figure 14. Intracellular functions of myosin motors. (A) Myosin functions in cell motility and cell adhesion. *a*, Lamellipodial protrusion driven by actin polymerization, with Myo1 family members contributing to the activation of actin nucleation. *b*, Limitation of lateral extension of lamellipodia by Myo1-dependent cortical tension. *c*, Limitation of lateral extension of lamellipodia by Myo2-driven contractility. *d*, Myo2-dependent tail retraction. *e*, Clustering of cell-substrate adhesion receptors. *f*, Elongation of filopodia due to Myo10-dependent transport of integrins to the filopodial tip. *g*, Myosin (Myo10 or Myo2) acting as a clutch coupling cell-substrate adhesion to the forward movement of the cell. *h*, Cell adhesion receptor endocytosis and recycling. *i*, Clustering of cell-cell adhesion receptors. *j*, Myo2-mediated "zippering up" of cell-cell junctions. **(B)** Roles of myosins in membrane traffic. *a*, Extension of pseudopods during phagocytosis (Myo1, Myo10). *b*, Adhesion of bacteria/food particles to the cell surface during phagocytosis (Myo7). *c–d*, Reorganization of cortical actin to allow invagination of a clathrin-coated pit (*c*) or fusion of an exocytic vesicle with the plasma membrane (*d*) (Myo1). *e*, Contribution of a minus-end-directed myosin (Myo6) to deformation of plasma membrane during clathrin-coated pit formation. *f–g*, Minus-end-directed transport of clathrin-coated (*f*) and uncoated (*g*) vesicles along actin filaments by Myo6. *h–i*, Membrane scission (*h*) and vesicle propulsion (*i*) driven actin polymerization with Myo1. *j*, Plus-end-directed transport of exocytic vesicles (Myo1). *k–l*, Switch between microtubule-dependent and actin-dependent transport, resulting in vesicle capture and anchoring (*k*) or short-range transport along actin filaments (*l*). Image modified from Krendel and Mooseker 2005 [87].

3.2 Myosin V family

3.2.1 General structure and functions

Myosin V heavy chain was first cloned from yeast [116] which have been further shown to express two class V myosins [117]. In vertebrates there are at least, three distinct subclasses of myosin V (Myo5A, Myo5B and Myo5C) with specific tissue distribution. Within the cell, they are usually abundant in the actin-rich periphery where they develop their main functions: they participate in the intracellular distribution of membranous cargoes and organelles, secretory vesicles, recycling endosomes, mRNA, lipids and proteins in a short-range transport along actin tracks. Kinesin and dyneins would provide similar functions in a long-range movement along microtubule tracks [118,119].

MYO5 proteins are high molecular weight proteins (~200 KDa) formed by approximately 1800 aminoacids encoded in around 40 exons (**Figure 15**). The **motor domain** contains the actin and nucleotide-binding sites and it is followed by a 24 nm helical **lever arm** containing six IQ motifs, with the consensus aminoacid sequence IQxxxRGxxxR. They bind 6 calmodulins or related light chains that have not retained functional calcium binding sites. Such comparatively long lever arm is consistent with myosin V molecules working as processive motors taking 50 or more ATP-dependent steps before dissociating from actin filaments. The step size is 36 nm, which matches the half-helical repeat of the actin filament, essentially allowing myosin V to walk ‘straight’ across the top of an actin filament [120]. The **tail domain** or **rod region** contains a heptad repeat seven amino acid motif responsible for the formation of an α-helical coiled-coil region involved in MYO5 dimerization. The rod region contains a PEST site (absent in MYO5C), a region enriched in proline (P), glutamic acid (E), serine (S) and threonine (T) residues that targets rapid proteolysis by proteases such as calcium-dependent protease calpain or the proteasome complex [121]. The coiled-coil structure follows the PEST site in MYO5A and MYO5B (**Figure 15**). This part of the tail contains exons A-F that are alternatively spliced in different tissues, originating various isoforms with different cargo specificities. Exon

Figure 15. The three human class V myosins and its molecular structure. (A) Schematic protein sequences of the three class V myosins. The IQ motifs (black), PEST site (dark grey) and representative exons (white) are delimited by the number of the aminoacid in the protein sequence. MYO5A shares a 63% identity on its aminoacidic sequence compared MYO5B and 51% compared to MYO5C. MYO5B and MYO5C share 52% identity among them. They mostly differ in their C-terminal domains. Note that MYO5C lacks PEST domain and MYO5B and MYO5C lack exon F. The information was obtained from NCBI and UniProt databases. BLAST® tool (NIH) was employed for the alignment. **(B)** Three dimensional structure of human class V myosins; N-terminal head domain (blue) neck region with six calmodulins (black), tail domain or rod region with the typical coiled-coil conformation is represented in grey, C-terminal globular tail domain (green). The molecular weight is of each protein is shown. Note that MYO5C is ~12KDa smaller than MYO5B and MYO5A due to its lack of PEST region. Adapted from Rodriguez *et al* 2002 [124].

3.2.2 Function regulation

The interaction of MYO5 with cargoes needs to be regulated in time and space. There are several mechanisms that control the process:

1. MYO5 proteins undergo a **conformational change** switching from an open-extended "active" form to a compact "inactive" form, as revealed by electron microscopy. In the inactive state, the protein has a folded structure in which the CBD interacts with the head domain [125–127] (**Figure 16**). These changes regulate motor mechano-enzymatic activity and have been shown to be Ca^{+2} dependent. Thus, nanomolar calcium concentrations unfold and activate the motor protein whereas micromolar calcium concentrations favor the compact conformation, probably by acting on calmodulin that remains strongly associated to the IQ motifs in the absence of calcium [125,127,128]. Moreover, cargo binding itself would also contribute to this conformational equilibrium as demonstrated by Li *et al.* 2005 [129]. Binding of the adaptor protein melanophilin, that recruits MYO5A to the melanosomes, plays significant role in the activation of myosin VA ATPase activity. Then, myosin motors could be potentially switched upon their binding to the cargo molecules, thus avoiding unnecessary ATP consumption (**Figure 16**).

bind directly to RAB proteins, or indirectly through **RAB effectors** [93], increasing the complexity of motor association with membrane trafficking systems. The nucleotide state of the G-protein involved in MYO5 recruitment to the cargo constitutes another regulation point. One example was already mentioned when describing melanosome transport. The linker Slac2-a/melanophilin only interacts with RAB27A on its GTP-bound form [95,96,131]. However, it remains unclear whether RAB proteins use MYO5 motors in distinct vesicle trafficking pathways or, alternatively, whether associations with MYO5 coordinate RAB proteins in the sequential regulation of different aspects of individual trafficking pathways.

4. **Alternative splicing of exons B, C, D and F** in the tail can help specify particular cargoes. For example, exon B is required for the interaction of MYO5A with dynein light chain 2 (DYNLL2). However, exon B of MYO5B does not resemble DYNLL2 binding regions and it likely does not interact with DYNLL2 [132,133]. MYO5B exon C is responsible for RAB8A coupling since Q1300L and Y1307C point mutations on this region abolish their interaction [101]. RAB8A also interacts with MYO5C but not with MYO5A [134]. Exon F, only present in MYO5A, is critical for association with melanophilin/Slac2 and RAB27A [122,129,135]. On the other hand, Exon D, highly conserved among all subclasses of myosin V determines its association with RAB10 [123]. RAB11A interacts with MYO5A and MYO5B via residues Y1714 and Q1748 in the globular tail domain, independently on their spliced form. These residues are not conserved for the case of MYO5C [101].

5. Another mechanism of regulation of cargo binding can be performed by **phosphorylation of specific residues**. For example, as shown in mitotic *Xenopus* melanophores, phosphorylation of a serine residue in the myosin tail by calcium/calmodulin-dependent protein kinase II results in dissociation of the motor from the cargo [136].

3.2.3 Myosin VA, distribution and functions.

MYO5A is primarily expressed in central nervous system (neurons, neuroendocrine cells) and skin (melanocytes) [119,131]. Alternative splicing is observed in different tissues. The isoform prevalent in brain contains exons A, B, C and E while that in melanocytes contains A, C, D, E and F [119].

MYO5A was first characterized in mice, encoded by the *dilute* locus. Mutations in the *dilute* (*Myo5A*) locus produced hypopigmentation in mice due to abnormal melanosome trafficking from melanocytes to keratinocytes, and neurological defects causing the death of the animal 2-3 weeks after birth [137]. Humans with homozygous mutations in *MYO5A* or proteins functioning as adaptors between MYO5A and the cargoes (RAB27 and melanophilin) develop Griscelly syndrome, a rare autosomal recessive disorder that associates hypopigmentation (partial albinism), and the occurrence of either neurological impairment or a severe immune disorder [131,138]. Further studies have demonstrated how dilute melanocytes failed in the accumulation of melanosomes in the periphery of the cell suggesting the relevance of MYO5A on this function. The melanosome transport is a cooperative (bidirectional) process that comprises a long-range microtubule-driven transport of the organelles from the center to the dendritic tips of the melanocytes, where they are captured and retained by MYO5A in the actin-rich periphery of the cell. Then, they are intercellularly transferred to adjacent keratinocytes. MYO5A motor protein acts preventing the centripetal microtubule-mediated transport of the organelles back to the center of the cell, which explains the phenotype observed in the dilute mice as a result of its inactivation [94,135]. Molecular characterization of this mechanism has involved a tripartite protein complex: small GTPase RAB27A protein interacts with the melanosome. Slac2-a/melanophilin protein binds specifically the GTP bound form of RAB27A and acts as a link-adaptor protein that connects the system with the globular tail of MYO5A. This mechanism is absolutely dependent on the presence of exon F in the motor protein [95,96].

A similar mechanism is observed in neuroendocrine cells (adrenal chromaffin cells and insulin-secreting cells). Secretory granules, storing hormones and neuropeptides, are transported along microtubules from the trans-golgi to the cell periphery, where they interact with the actin network and fully mature completely before exocytosis. Secretory granules in the cell periphery associate with the RAB27A GTPase that recruits the linker protein MYRIP (myosin-rab interacting protein)/Slac2-c and motor protein MYO5A. The complex Rab27a-Myrip/Slac2-c/Myo5a contributes to the retention of the secretory granules to the actin cortex prior exocytosis [139,140].

The central nervous system expresses a tissue-specific isoform of MYO5A that contains exon B, consisting of three aminoacids (DDK), and essential for binding dynein light chain 2 (DYNLL2). Its interaction alters the structure of the α-helical coiled coil and could act as an adapter between MYO5A and cargoes such as proapoptotic BMF [103] and the postsynaptic scaffolding protein GKAP (guanylate kinase domain-associated protein) [132,141]. On the other hand, the neurological disorders observed in *dilute* mice have been related with a depletion in the endoplasmic reticulum and a decreased Ca^{+2} release in the dendritic spines of cerebellar Purkinje cells. Further studies demonstrated how MYO5A accumulates at the ER tips pulling it into neuron spines. These observations indicate that MYO5A has a key role in the synapsis [131,142].

Myosin VA has been reported to participate in the assembly and maintenance of P-bodies (processing bodies), cytoplasmic foci involved in the storage and turnover of mRNA. It is also emerging that RNA and RNA-BPs (RNA-binding proteins) constitute another class of MYO5A cargo [143]. MYO5A has also been detected in the nucleus although its role has not yet been characterized [144].

3.2.4 Myosin VB, distribution and functions

Myosin VB was cloned from rat in 1996 by Zhao and colleagues that initially named it MYR6 (myosin from rat 6). It is mainly expressed in epithelial cells from the gastrointestinal tract (stomach, colon and small intestine), female and male reproductive tract organs (ovary, placenta, breast, epididymis…), thyroid glands and kidney [145,146] (**Figure 17**).

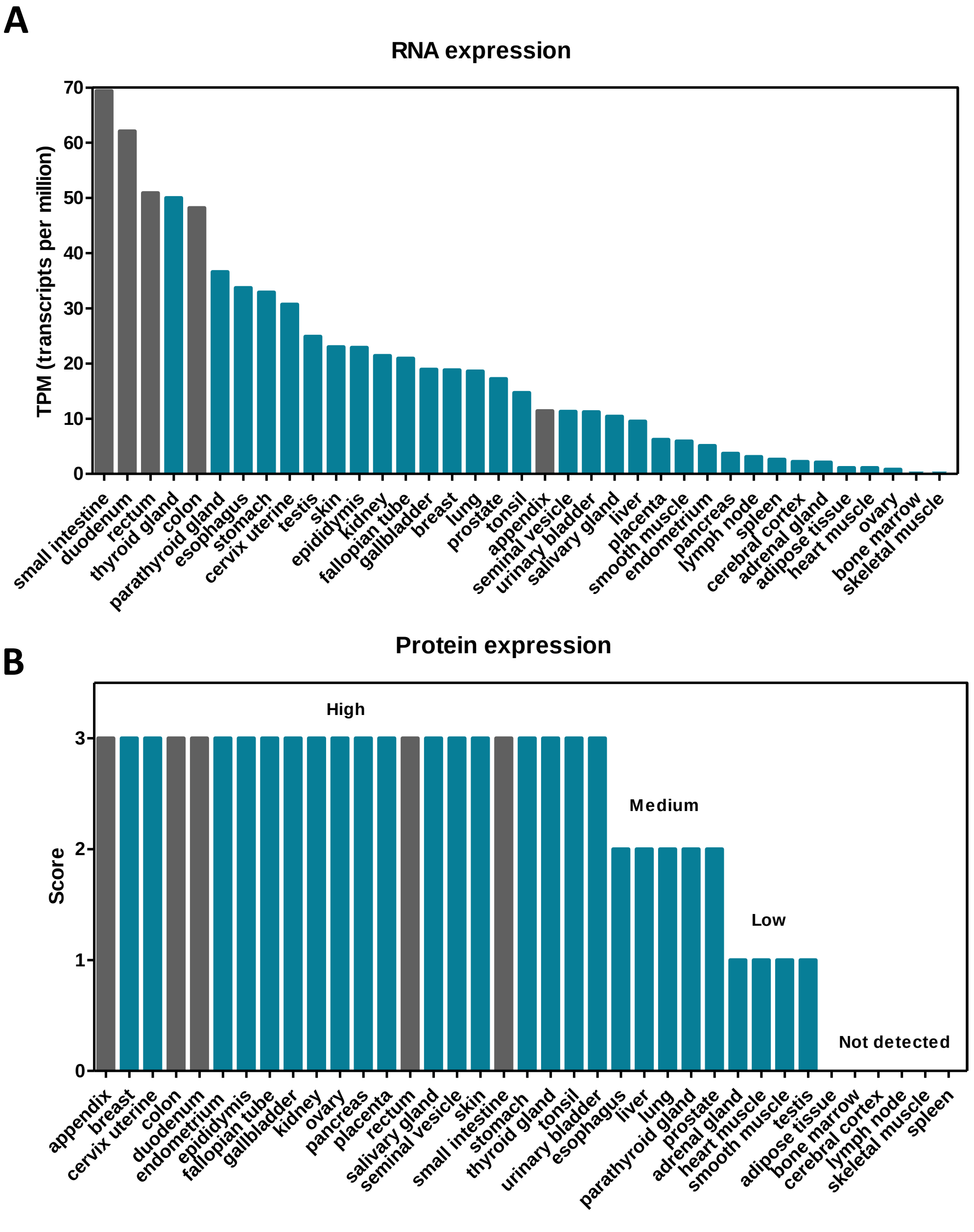

Figure 17. Myosin VB expression levels in normal tissues. (A) RNA-seq data showing myosin 5b expression levels in a panel of 37 normal tissues. The data is expressed as TPM (transcripts per million), corresponding to mean values of the different individual samples from each tissue (a minimum of two individual samples were analyzed). **(B)** Protein expression levels assayed by immunohistochemistry in a panel of 37 normal tissues. The score describes the intensity of antibody staining in a specific fraction of cells in the sample (in general epithelial and glandular cells) and is expressed as not detected (0), low (1), medium (2) or high (3). Samples from up to three different individuals were stained with two different antibodies (HPA040593 and HPA040902) and the mean score was calculated. Dark grey columns correspond to tissues from the small and large intestine. Pearson correlation between mRNA and protein expression was calculated (r=0.49, p=0.002, n=37). Information obtained from The human protein atlas [146].

1. Function in recycling endosomes trafficking

A number of investigations over the past several years have implicated MYO5B in the **regulation of recycling endosome trafficking** to the plasma membrane in both, non-polarized and polarized cells. After endocytosis, recycling of the internalized plasma membrane receptors, pumps, and channels is necessary for the maintenance of normal membrane composition. Internalized membrane and molecules can be degraded, entering the late-endosomal/lysosomal pathway, or transformed into recycling endosomes, tubule-vesicular membranous compartments that are transported back and fused to the membrane, connecting the endocytic and exocytic pathway. Recycling endosomes are thought to be specifically delivered to membrane regions that are undergoing growth and reorganization, and could be related to process such as epithelial cell-cell adhesion, epithelial polarity, cytokinesis or cell fate specifications. RAB11A is the best characterized marker for recycling endosomes [147]. Moreover, yeast-two hybrid and colocalization assays have clearly identified MYO5B as an interacting protein for RAB11A [101,148], that would act with the participation of a third protein, a downstream effector known as Rab11-Family Interacting Protein (RAB11-FIP2) which stabilizes the functional complex [148–150]. Another RAB11 family member, RAB25, also interacts with MYO5B and RAB11A-FIP2 as demonstrated by Lapierre *et al.* [148,149]. Both RAB11A and RAB25 recruit MYO5B and control the dynamic movements of apical membrane recycling system [151–153].

In non-polarized HeLa cells, overexpression of GFP-myosin VB tail (a powerful dominant-negative) was observed to retard the recycling of transferrin receptor (TFR) back to the plasma membrane, that was shown to accumulate in pericentrosomal vesicles. Several membrane proteins have been shown to traffic through a pathway controlled by RAB11A-MYO5B including EGF receptor in A431 squamous carcinoma cells [149], chemokine receptor CXCR2 in Hek293 cells [154], H^+/K^+-ATPase in gastric parietal cells [148,155], M4-muscarinic acetylcholine receptor (M_4) [156] and the glutamate receptor subunit GluR1 in central nervous system [157–159]. On the other hand, overexpression of the myosin VB tail in polarized MDCK (Madin-Darby canine kidney) cells stably expressing the polymeric immunoglobulin A receptor (pIgR) caused accumulation of basolaterally endocytosed dimeric immunoglobulin A (IgA) and pIgR in the pericentrosomal region, suggesting a deregulation in the transcytosis and apical recycling process. Unlike the pIgR that mediates the polarized secretion of dimeric IgA, the Fc receptor (FcRn) traffics IgG in both directions (apical and basolateral) across epithelial barriers. A similar study in MDCK cells demonstrated that RAB25-MYO5B regulates a sorting step that specifies transcytosis for FcRn in both directions without affecting its recycling. However, RAB11A-MYO5B, although dispensable for FcRn transcytosis, affects receptor-mediated recycling of IgG in the basolateral pathway only. This is the first study showing that RAB25-MYO5B participates in transport of cargo to basolateral membranes [160]. Basolateral recycling of transferrin is not affected by RAB11A neither RAB25 function in polarized MDCK cells [151].

All these data indicate that the molecular motor MYO5B is required for exocytosis in plasma membrane recycling systems in nonpolarized cells and apical recycling system in polarized cells [148]. Moreover, RAB11A and RAB25 with the participation of MYO5B regulate and coordinate the trafficking to the apical or basolateral domain of polarized cells, although the mechanism is not well understand yet.

2. Function in polarization

Over the last few years, many studies have shown a role of MYO5B in the **establishment of polarized function in epithelial cells**. Indeed, *MYO5B* mutations cause microvillus inclusion disease (MVID), a human neonatal diarrheal disease likely due to defects in apical polarization, brush border formation and transporter protein localization [161]. *Drosophila* photoreceptors, like many polarized epithelial cells, greatly amplify their apical membranes during terminal differentiation via targeted membrane delivery. The proteins Rab11, dRip11, and Myo5 mediate this morphogenic secretory traffic [162]. The participation of Myo5b interacting protein Rab11a also seems to be crucial during the polarization process of MDCK cells. The results indicate that the phosphorylation of Rab11-FIP2 on serine 227 by the kinase MARK2/EMK1/Par-1Balpha (MARK2) regulates lumen formation and composition of both, adherens and tight junctions, and is intimately involved in the regulation of polarity in epithelial cells [163,164]. Apical surface and lumen formation is also regulated by Rab11a that, on its active form, recruits Rab guanine nucleotide exchange factor (GEF) Rabin8, and its target Rab8, to subapical vesicles. Rab8a and Rab11a function through the exocyst, an octamer protein complex (Sec3, Sec5, Sec6, Sec8, Sec10, Sec15, Exo70, Exo84) that is implicated in the tethering of secretory vesicles to the plasma membrane prior to N-ethylmaleimide-sensitive factor (NSF) attachment protein receptor (SNARE)-mediated fusion [165]. Thus, Rab8a and Rab11a interaction with the Sec15 exocyst subunit and Anx2 (annexin 2) target Par3-aPKC (partitioning defective 3 (Par3), atypical protein kinase C (aPKC)) complex to the nascent apical surface areas. In the apical region they control Rho GTPase Cdc42 activation through its GEF Tuba [166]. Par6 protein functions as a key adaptor to link Par3/6-aPKC-Cdc42 polarity complex. This complex was already known to participate in cell division [167,168] and tight junctions formation [169] (see Figure 21B). However, this study shows a new role in the regulation of vesicular transport to the apical surface from Rab8a/Rab11a-positive vesicles and reveals an interaction between the machineries of vesicular transport and polarization [166].

The cooperation of Rab8a and Rab11a in apical trafficking supports the hypothesis that association with both GTPases may regulate MYO5B participation in apical membrane transport. Nevertheless, it was not clear how specific interaction with one or another Rab can regulate alternate trafficking pathways. Roland and colleagues [101] demonstrated that transferrin receptor trafficking in non-polarized HeLa cells was affected by perturbing RAB11A-MYO5B, but not RAB8A–MYO5B function, confirming previous results from Lapierre *et al.* [148]. Furthermore, in HeLa cells RAB8A and MYO5B colocalize to a tubular network containing EHD1 and EHD3, which does not contain RAB11A [134]. RAB8A anterograde vesicle transport through MYO5B have also been shown to be partially responsible for secreting Wnt in Paneth cells and fibroblasts from the intestinal crypt, mediated by the Wnt-specific transmembrane transporter GPR177 (G protein-coupled receptor 177). Thus, Rab8a knockout mice show a decrease Wnt/β-catenin signaling and impaired Paneth cell maturation (a Wnt-dependent event; see **Figure 20C**) [170,171]. These findings indicate that RAB8A and RAB11A define different recycling pathways that both use myosin VB. In contrast, in polarized MDCK cyst cultures, de novo lumen formation was dependent on Myo5b association with both Rab8a and Rab11a, but not Rab10 [101]. As explained by Bryant *et al.* [166], during MDCK lumen formation, Rab11a induces Rab8a activation by recruiting its GEF Rabin8. A similar mechanism is observed during primary ciliogenesis [172] and stretch-regulated exocytosis in bladder umbrella cells [173], suggesting a cascade RAB11A to RAB8A controlling this process. As both GTPases bind to different MYO5B regions, it would be of interest to understand whether simultaneous or sequential Rab binding regulates MYO5B function.

The **mechanism of the brush border formation and maintenance** in the highly polarized enterocytes has also been object of many studies. The polarity program is driven by serine/threonine liver kinase B1 (LKB1) activated by the pseudo-kinase STRAD, and the adaptor protein MO25. The complex triggers an asymmetric distribution of guanine nucleotide exchange factor PDZGEF to an apical phosphatidylinositol 4,5-bisphosphate (PtdIns(4,5)P2) landmark, and subsequent activation of the small G protein RAP2A, its effector TNIK and the kinase MST4, anchored to the cis-Golgi. Ultimately, MST4 phosphorylates Ezrin at T567 to trigger its open conformation, which induces brush border formation through linkage of the cortical membrane to the underlying actin cytoskeleton [13,174–176] (Figure 19).

Similar studies have related aPKC, AKT2, LOK and SLK kinases with ezrin phosphorylation, suggesting different variants of the same mechanism that could act at different stages of enterocyte maturation [13,177–179]. For example, aPKC was shown to be a major player during the early stages of intestinal cell differentiation and polarization [177]. Definitely, any mechanism phosphorylating ezrin at T567 must operate exclusively at the apical domain to achieve its full apical localization. AKT2, LOK and SLK are already localized at the apical plasma membrane domain, however, regulation of Golgi associated-MST4 and cytoplasmic aPKC trafficking to the apical membrane was not well understood at this point.

A new study from Dhekne *et al.* [102] demonstrated how these two kinases (MST4 and aPKC) codistributed both *in vivo* and *in vitro* with RAB11A small GTPase in subapical recycling endosomes. Knockdown of MYO5B or overexpression of a mutant form of RAB11A, unable to bind MYO5B, prevented the subapical enrichment of recycling endosomes as well as MST4 and aPKC without inhibiting LKB1-induced cell polarization process of apical enrichment of ezrin. However, ezrin T567 phosphorylation and microvilli formation was impaired. In addition, immunofluorescence analysis of the enterocytes of a MVID patient carrying homozygous *MYO5B* mutations showed that MST4 and aPKC were displaced with RAB11A from the apical domain to the supranuclear region. Finally, all these data support a model in which RAB11A and MYO5B maintain a subapical signaling platform in the form of recycling endosomes that position MST4 and aPKC contributing to the activation of ezrin, and therefore, controlling the dynamic organization of the intestinal brush border membrane (**Figure 18**).

polymerase I transcription complex and newly synthesized ribosomal RNA (rRNA) suggesting a possible role supporting rRNA transcription [144].

3.2.5 Microvillus inclusion disease

Microvillus inclusion disease or microvillus atrophy is a congenital autosomal recessive syndrome characterized by intractable, life-threatening, watery diarrhea that most commonly starts within the first days of life, and can cause the loss of up to 30% of body weight within 24 h. In some cases (<20%), MVID manifests at later times, within the first 3–4 months of life (known as late-onset MVID) [180–182]. It is consider as a very rare disease and the prevalence is unknown. Histological examination of intestinal samples revealed microvillus atrophy, presence of cytoplasmic microvillus inclusions and accumulation of periodic acid–Schiff (PAS)-positive cytoplasmic granules in intestinal epithelial cells (**Figure 19**). Small bowel transplantation or complete parenteral nutrition constitutes so far the only treatment options available [181–184]. No additional clinical signs are associated with MVID; in particular, there are no malformations or involvement of other organs such as liver or kidney, although many patients frequently develop cholestasis and liver disease as consequence of the long-term parenteral nutrition [182,184]. Inactivating mutations in *MYO5B* have been related with the majority of the cases of MVID (www.MVID-central.org) [161,185,186]. Interestingly, a recent study have shown that loss of the t-SNARE syntaxin 3 (STX3), an apical receptor involved in membrane fusion of apical vesicles in enterocytes, is responsible of a milder variant form of MVID [187].

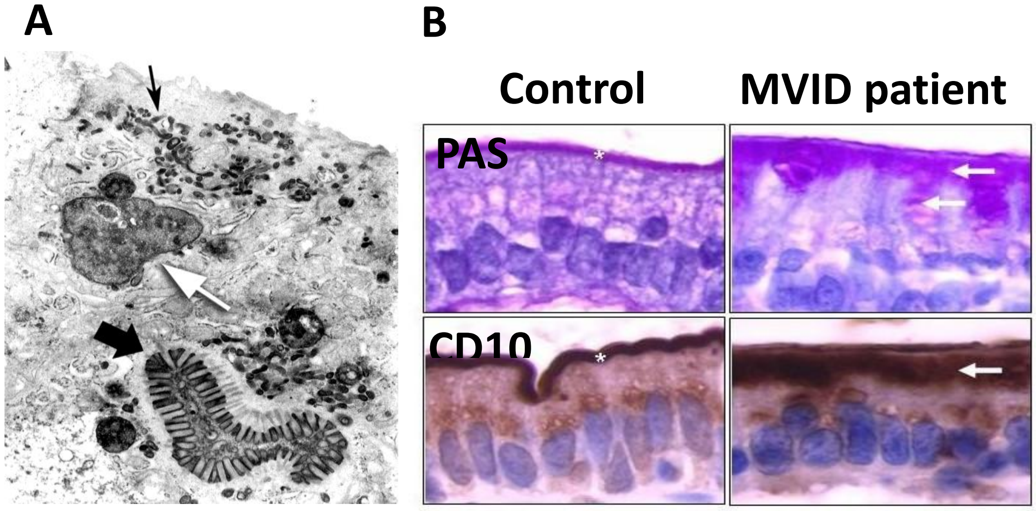

Figure 19. Microvillus inclusion disease. (A) MVID patient enterocyte showing denuded luminal surface, numerous electron-dense small, comma-shaped vesicles (possibly immature microvilli, arrow), and a large lysosome (white arrow). In a deeper location, a microvillus inclusion (broad dark arrow) is seen, surrounded by lysosomes and comma-shaped vesicles, 6000X. Obtained from Iancu *et al.*[188] **(B)** Duodenal section of a MVID patient stained for PAS and CD10. Both markers are observed at the apical pole of the cell (white arrow) instead at the brush border (asterisk). Modified from Ruemmele *et al.*[182]

Many studies have tried to understand MVID pathogenesis developing different *in vitro* models, often using the Caco2 cell line. Caco2 cells, originally derived from a colon adenocarcinoma, undergo a process of spontaneous differentiation when cultured in confluence, that after two or three weeks leads to the formation of a monolayer of polarized cells, coupled by tight junctions, and expressing several morphological and functional features of small intestinal enterocytes [189]. Thus, *MYO5B* depletion in Caco2 cells disrupted cell polarity as reflected by loss of surface microvilli, formation of microvillus inclusions [185], and mislocalization of apical brush border proteins (villin, CD10 and CD36) and basolateral transporter proteins (H+/K+-ATPase, TFR) to the cytoplasm. Altered distribution of certain endosomal/lysosomal constituents including RAB11A and RAB8A from the subapical surface was also observed, in good agreement with the results obtained on the histological analysis of MVID biopsies [190]. In a similar study, overexpression of MYO5B mutant form that cannot bind RAB8A promoted loss of microvilli whereas the formation of microvillus inclusions seems to be caused by the loss of MYO5B interaction with RAB11A. Microvillus inclusions result from the internalization of segments of apical membrane: since the normal apical recycling process is MYO5B-RAB11A-dependent, microvillus inclusions may reflect the effects of mutant MYO5B molecules on this process. On the other hand, the apical SNARE complex including STX3 facilitates fusion of the target membrane and vesicles that have been trafficked into close apposition by the RAB11A-regulated effector protein MYO5B. In general, defects in the apical recycling endosomes pathway seem to cause the gross change in cell polarity and mucosal integrity observed in MVID patients. [187,191].

A recent study performed by Vogel *et al*. [192] has described a selective role of MYO5B and STX3 for apical cargo exocytosis in polarized epithelial cells that partially explains the pathophysiology of the disease and helps to better understand the RAB11A/RAB8A cascade previously explained. Thus, apically destined cargo such as sodium/hydrogen exchanger 3 (NHE3), cystic fibrosis transmembrane conductance regulator (CFTR) or glucose transporter 5 (GLUT5) are transported via RAB11A/RAB8A and MYO5B toward the vicinity of the apical plasma membrane, where the exocyst tethers cargo vesicles and, subsequently, the v-SNARE–like SLP4A and the apical t-SNARE STX3 mediate vesicle fusion. V-SNARE VAMP7 and MUNC18-2 proteins also participate in the complex and act as direct components of the fusion machinery (**Figure 20A**). Loss of MYO5B or STX3 disrupts this selective apical exocytosis and could then explain some of the phenotypes observed; NHE3 is essential for intestinal sodium homeostasis, and NHE3 knockout mice suffer from intractable diarrhea. Moreover, GLUT5 mislocalization likely contributes to intestinal malabsorption. On the other hand, the brush border enzymes dipeptidyl peptidase IV (DPPIV) and sucrase-isomaltase (SI) appeared correctly localized although some MVID cases as well as *RAB8A* and *RAB11A* knockout mice showed intracellular enrichment of these enzymes [171,193]. The route that these enzymes use to reach the apical membrane is not yet clear (**Figure 20A**).

Interestingly, another study carried out with four MVID patient samples has found a complete depletion of the polarity complex proteins PAR6, aPKC and CDC42 from the apical side of the enterocytes and redistribution to either the cytoplasm or the basal pole of the cells. The same result was observed for ezrin and p-ezrin. These observations suggest a complete polarity inversion that was also reproduced in 3D dimensional grown Caco2 cells forming cysts after [194] depletion. Ezrin, p-ezrin and aPKC were also observed mislocalized in two MVID patients in an independent study [102]. The polarity complex (PAR3, PAR6, aPKC and CDC42) was already mentioned to participate in cell division [167,168] and tight junctions formation [169]. Moreover, CDC42 regulates proliferation, polarity, migration, and differentiation of intestinal epithelial cells in mice and defects in CDC42 signaling results in a MVID-like phenotype [195]. Haploinsufficient mice for both *Cdc42* and *Rab8a* in the intestine demonstrated abnormal crypt morphogenesis and epithelial transporter physiology, showing a cooperative role that control cytokinesis and apical domain establishment [196]. Overall, these results point out CDC42 as a master regulator of epithelial homeostasis and give some new clues in the study of the molecular pathology of MVID (**Figure 20**).

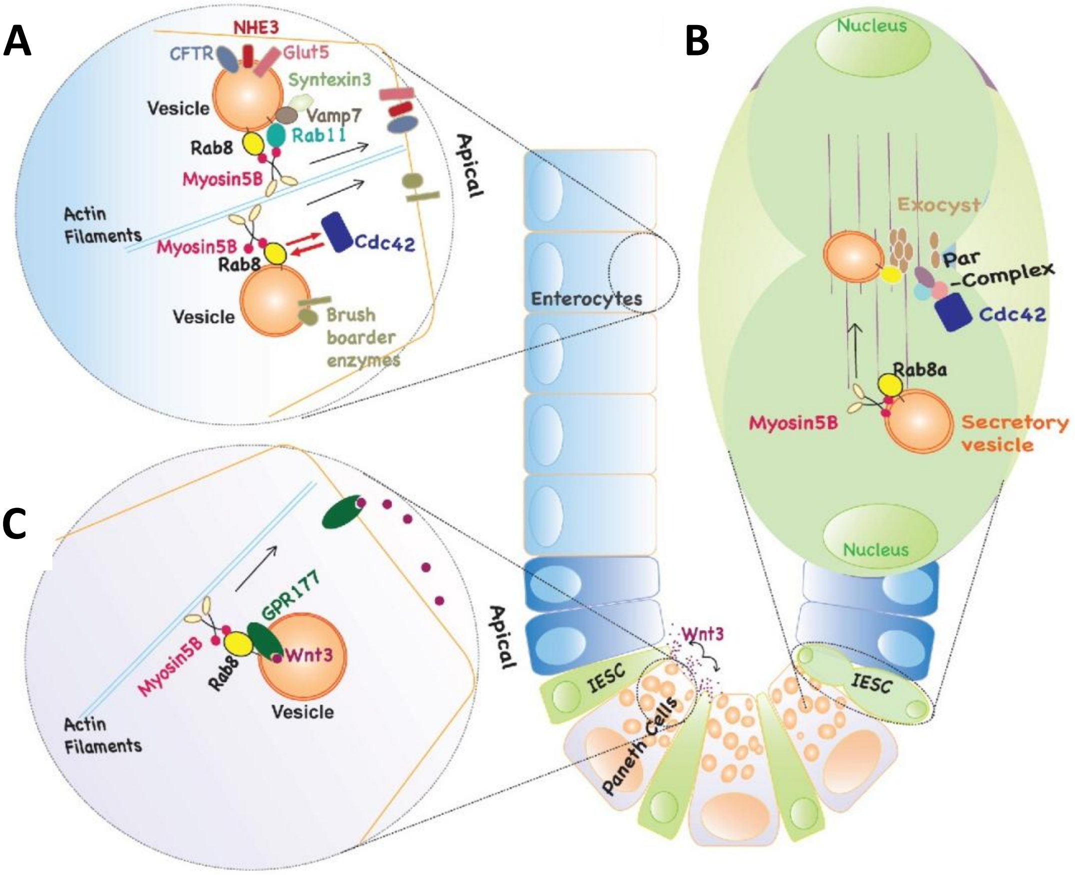

Figure 20. RAB8A, RAB11A and MYO5B regulate multiple aspects of intestinal epithelial homeostasis. (A) RAB8A and RAB11A mediate the transport of apical cargoes in enterocytes, including GLUT5, NHE3 and CFTR, by recruiting MYO5B. The tethering of these cargo-containing vesicles to apical plasma membrane depends on RAB11A interacting with VAMP7/STX3. Apical trafficking of brush border enzymes, including DPPIV, AP, and SI is mediated by RAB8A with little involvement of MYO5B or STX3. CDC42 navigates apical transport of RAB8A vesicles to plasma membrane. **(B)** CDC42-PAR polarity complex is required for the division and differentiation of stem cells. RAB8A positive vesicles driven by MYO5B are important for the proper localization of the complex. **(C)** In Paneth cells and crypt fibroblast (Wnt secreting cells), RAB8A-MYO5B facilitates WNT3 secretion through G protein-coupled receptor 177 (GPR177) transport to plasma membrane. Obtained from Zhang *et al.*[197].

The lack of animal models for MVID has hampered deepening in a better knowledge of the molecular mechanisms of the disease [198]. Interestingly, intestine-specific knockout mice models for Rab8a and Rab11a have been developed [171,193]. Rab8a knockout mice died 3-4 weeks after birth. Their intestines showed mislocalization of the apical markers AP, SI, oligopeptide transporter 1 (PepT1) and DPPIV. Intestine-specific Rab11a knockout animals died within 2 weeks after birth and also showed mislocalized apical AP and DPPIV. DPPIV was observed in lysosomes in both cases. Moreover, both models displayed shortening of microvilli and microvillus inclusions. All these features, which coincide with MVID phenotype, ultimately lead to malnutrition and the death of the mice. The results obtained demonstrate a functional relationship between Rab11a, Rab8a and Myo5b in vivo. Another MVID model in Zebrafish has also been recently proposed [199].

3.2.6 Myosin VC, distribution and functions

The third member of the class V myosin was first described in 2001 [124]. It is abundant in many secretory and glandular (exocrine) tissues including pancreas, prostate, mammary, stomach, colon and lung where it is expressed chiefly in epithelial cells. Initial studies in HeLa cells showed that MYO5C partially colocalizes with a subset of recycling compartments that contain transferrin receptor and RAB8. These compartments were not associated with RAB11A suggesting that are distinct from the RAB11A compartment associated with MYO5B [124,148]. Consistent with its role in exocrine secretion, MYO5C has been identified in zymogen granules from pancreas [200] and mature secretory granules in lacrimal gland acinar cells [201]. These observations were latter confirmed in a study where MYO5C was found to colocalize with two different endogenous markers of secretory granules, RAB27B and RAB3D. These imaging data, obtained in MCF-7 cells, provide strong evidence that this class V myosin functions in the trafficking of exocrine secretory granules [202]. Although MYO5C is not particularly abundant in melanocytes, it has also been related with melanosomes biogenesis and secretion functioning as an effector of melanosome-associated RAB32 and RAB38 GTPases [203].

It is clear that myosin VC develops a similar function in cargo transporter and trafficking as its counterparts MYO5A and MYO5B, although it is not processive on single-actin filaments. MYO5C does not share the ability to take multiple steps on actin filaments. When actin is organized as a single filament, MYO5C shows step-size variability and backwards steps (~40% of total steps). Molecular studies of the motor domains showed that it remains bound to actin for less than half of its ATPase cycle, implying that their kinetics are incompatible with processivity [204,205]. The step-size variability of its back stepping behavior were attributed to structural features in the lever arm/rod region that would make it more flexible. Then, how can MYO5C carry out its role in trafficking? Apparently, this motor protein has been tuned and specialized to transport on actin bundles. This property is due to the flexibility of its lever arm that has greater access to the lateral acting binding sites in the bundle. Secretory granules are likely transported by "teams" of MYO5C that move together along the bundles, which are restricted to the apical membrane and provide the only track suitable for continuous motion [205].

3.2.7 Myosins and Cancer

The tumorigenic process comprises aspects where myosins are known to have a crucial function (cell polarity and adhesion, formation of protrusions, cell migration and invasion, etc…). Then, it is not striking that some members of the myosin superfamily are implicated in the pathogenesis of specific tumors [206]. This fact has been widely reviewed by Li and Yang [207]. Myosins alterations lead to cytokinesis failure, chromosomal and centrosomal amplification, multipolar spindle formation and activating various processes of tumor invasion and metastasis such as cell migration, adhesion, protrusion formation, loss of cell polarity and suppression of apoptosis. Therefore, myosin alterations contribute to neoplastic transformation at different stages that can be framed in terms of the more general pathways that drive tumor progression, described above as "hallmarks of cancer" [206].

The relationship between MYO5A and cancer has been partially studied. At least two of the binding partners of MYO5A are proteins with known connections to cancer. One is the tumor suppressor gene PTEN [208], and the other is BMF, a pro-apoptotic protein [103]. MYO5A interaction with PTEN has been shown to contribute to the regulation of neuronal size by modulating

PTEN signaling pathways and MYO5B may also play a redundant role in PTEN regulation. Nevertheless, whether regulation of PTEN by MYO5 contributes to cancer progression remains still unknown [208]. In the case of BMF-MYO5A complex, it has been shown how overexpression of a MYO5A tail fragment that sequesters BMF, resulted in enhanced apoptosis of melanoma cells and decreased melanoma growth in mice [209]. Moreover, myosin VA was shown to be up-regulated by SNAIL, which promotes cancer cell invasion [210]. Regarding MYO5B, earlier studies have demonstrated that its inactivation participates in gastric cancer tumorigenesis, promoting proliferation, invasion and motility [211]. Since the mechanism has not been yet determined it is not clear whether the loss of MYO5B is a consequence or cause of human gastric cancers. A similar result was found studying MYO5B protein adaptor RAB11-FIP2, whose overexpression promoted gastric cancer migration possibly mediated by hypoxia [212]. Importantly, loss of RAB25, another MYO5B interacting protein, has been recently characterized as a novel tumor suppressor on colonic neoplasia and reduced expression of this small GTPase is associated with shorter patient survival [213,214]. Moreover, *MYO5B* inactivation by promoter methylation also contributes to the oncogenic process of acute lymphoblastic leukemia [215] and *MYO5B* gene is located in chromosome 18q21, the genomic region most frequently deleted in colorectal tumors [216].

A earlier study carried out by our group has shown how the brush border myosin IA has tumor suppressor activity in colorectal cancer [217] pointing out that colorectal cancer can be promoted by the loss of intestinal epithelial polarity. The importance of MYO5B in the maintenance of the brush border has been widely explained in this introduction and is revealed in MVID. In conclusion, loss of polarity and differentiation as well as deregulation in vesicle trafficking, where MYO5B plays a crucial role, are key events in cancer [218] . However, the direct connection between MYO5B and colorectal cancer has not been established yet.

AIMS OF THE STUDY

The role of unconventional myosin VB in the polarization and correct function of the enterocyte has been well established [101,102] and is reflected in MVID [185]. However, the molecular mechanisms underlying the disease are not understood yet, mainly due to the lack of animal models. In addition, the loss of polarization and differentiation are key events in the progression of colorectal cancer, processes were other unconventional myosins, such as myosin IA, are implicated [217].

Therefore, the specific aims of this study were:

- Generation and characterization of a constitutive *Myo5B* knockout and intestine-epithelium specific *Myo5b* knockout mice.

- To study the functional relevance of MYO5B overexpression and inactivation in the oncogenic process of colorectal tumors using inducible *in vitro* cell line models and *in vivo* subcutaneous xenografts.

- To evaluate the association between MYO5B tumor levels and survival or clinicopathological features of colorectal cancer patients.

MATERIALS AND METHODS

Generation of *Myo5b* knockout mice. *Myo5b*$^{tm1a(KOMP)Wtsi}$ targeted ES cells (C57BL/6, agouti, clone EPD0526_3_A11) were obtained from the KOMP repository at UC Davis [219,220]. After expansion, cells were injected into donor blastocysts and transplanted into pseudopregnant females. Chimeric male offspring were mated to C57BL/6 females to confirm germ line transmission. Mice genomic DNA was obtained as described below and genotypes were confirmed by PCR using pairs of different primers described in **Figure 21** and Table 2. The initial *tm1a* allele generates a null allele through splicing to a lacZ trapping element, including the mouse En2 splice acceptor and the SV40 polyadenylation sequence **(Figure 21 and 22A)**. Heterozygous *Myo5b*$^{tm1a(KOMP)Wtsi}$ mice were intercrossed to obtain animals homozygous for the targeted *Myo5b* allele (knockout mice). The wild-type and knockout embryos and newborns obtained were employed for the phenotype studies.

Generation and induction of *Vil-Cre*$^{ERT2;}$ *Myo5b*$^{tm1c/tm1c}$ mice. *Myo5b*^{tm1c} mice with conditional *Myo5b* knockout were generated by crossing two *Myo5b*$^{tm1a(KOMP)Wtsi}$ heterozygous females with a C57BL/6 Tg(CAG-Flpo)1Afst (Flp deleter) [221] male (**Figure 22A**). The recombination of the trapping element was verified by DNA sequencing and the wild-type animals for the Flp transgene were selected and breed. For intestinal-epithelium specific *Myo5t*$^{tm1c/tm1c}$ mice were crossed to a C57BL/6 Tg(Vil-cre/ERT2)23Syr (*Vil-Cre*^{ERT2}) mice [222], carrying a tamoxifen inducible Cre recombinase expressed under the control of the Villin promoter which allows gene deletion in all epithelial cells of the intestine, providing spatial and temporal control of the knockout (**Figure 22A**) Homozygous and heterozygous *Myo5t*^{tm1c} mice that were wild type for the *Vil-Cre*^{ERT2} transgene were used as control animals. A pair of different primers was used for genotyping (**Figure 21 and Table 2**). Cre enzyme was induced by a single intraperitoneal (i.p.) injection of 4 mg/25g weight of tamoxifen (Sigma-Aldrich) dissolved in corn oil (10 mg/mL) (Sigma-Aldrich) in both *Vil-Cre*^{ERT2}; *Myo5t*$^{tm1c/tm1c}$ and control animals. The 8–10 weeks-old mice were weighted every day and sacrificed

Plasmids. pINDUCER toolkit was used to generate cell lines with doxycycline-inducible overexpression or downregulation of MYO5B [223]. ***Overexpression cell line models:*** *MYO5B* sequence, containing exon D, was obtained from ensemble (ENST00000285039.11) and mCherry sequence was added to the 5′ end (N-terminal end of the protein). The full sequence was generated by gene synthesis (Biomatik) and cloned into a pUC57 backbone. Then, the sequence was transferred to pINDUCER20 through gateway cloning (Life technologies). A MYO5B mutant form containing the truncating mutation C866A found in a MVID patient [185] coding for Ser289X was generated using Quick Change II Site-Directed mutagenesis Kit (Agilent technologies) and transferred to pINDUCER20. The primers used were Myo5b-C866A-F and Myo5b-C866A-R (**Table 2**). Empty vector containing only mCherry was generated by cutting out *MYO5B* sequence and cloned into pINDUCER20. ***Downregulation cell line models:*** three different shRNA sequences against MYO5B, previously described in the literature, were used: shRNA#2 [190]; shRNA#3 [190]; shRNA#4 [102]. As non-targeting control a sequence against firefly luciferase was selected (**Table 2**). Then, mir30-shRNA were designed using RNAi oligo retriever web server (http://cancan.cshl.edu/RNAi_central/RNAi.cgi?type=shRNA) and cloned into pINDUCER10 following the protocol described by Paddison *et al*. [224]. ***Knockout cell line model:*** For this purpose, CRISPR/Cas9 technology was used. The sgRNA sequence targeting *MYO5B* exon 5 was designed using CRISPR design tool (http://crispr.mit.edu:8079/). The sgRNA was selected according to its on-target score (98 on a scale ranging from 0 to 100) and low probability of off-targets (**Table 3**). The predicted sequence was cloned into pSpCas9(BB)-2A-GFP (pX458, Addgene #48138) following the protocol described by Zhang's Lab (http://www.genome-engineering.org/crispr/?page_id=23). ***Other plasmids:*** pEGFP-Rab11a-WT vector was kindly provided by Dr. Sven CD. Van Ijzendoorn. pMD.G2 and psPAX packaging vectors for lentivirus production were obtained from addgene (#12259 and #12260 respectively).

Table 3. sgRNA sequence used for CRISPR/Cas9 on Caco2-BBE cells and its possible offtargets.

Exon	On-target score (0-100)	sgRNA sequence (5' to 3')	PAM	Off-target score (0-100)	Locus/ UCSC gene	Protein
5	98	ATGCGCTATTTCGCCACCGT	TGG	0.4	chr16: +17511478/ NCR*	-
				0.4	chr15: -48631824/ NCR*	-
				0.3	chr15: -52567815/ NM_018728	MYO5C
				0.2	chr1: -39318925/ NCR*	-
				0.2	chr5: -159478229/ NM_003314	TTC1 (G protein-coupled receptor interactor protein)
				0.1	chr13: +81396676/ NCR*	-
				0.1	chr4: +158257880/ NM_001083620	GRIA2 (glutamate ionotropic receptor AMPA type subunit 2)
				0.1	chrX: +125300468/ NCR*	-
				0	chr7: +158735254/ NCR*	-
				0	chr8: +74285882/ *NCR	-
				0	chr12: +5020750/ NM_000217	KCNA1 (potassium voltage-gated channel subfamily A member 1)

*NCR: not coding region

Cell lines and generation of isogenic *in vitro* models. All cell lines used in this study were maintained on Dubelco's Modified Eagle's Medium (DMEM; Life technologies) containing 10% fetal bovine serum (FBS; Sigma-Aldrich) and 1x antibiotic-antimycotic (Life Technologies; 10,000 U penicillin, 10,000 µg of streptomycin, and 25 µg/ml of amphotericin B) at 37°C/5% CO2. ***Overexpression cell line models:*** RKO and SW837 colon cancer cell lines were stably transduced with pINDUCER20-mCherry-MYO5B or pINDUCER20-EV (mCherry) lentiviral-containing particles. Production lentivirus and infection was carried out as follows: the first day, TLA-HEK293T cells were plated in a 10-cm plate (3x10^6 cells/plate) to achieve ≃80% confluence on the following day. The second day (24 h after seeding), TLA-HEK293T cells were transfected with 10 µg of the lentiviral vector, 3.5 µg and 2.75 µg of the packaging vectors pMD.G2 and psPAX2 respectively, using PEI (4 µg PEI: 1 µg total DNA; Polyscience). The following day (≃16 h after transfection), the media was replaced with 7 ml of 5% FBS DMEM media containing 5 mM sodium butyrate. From this point on, biosecurity level-2 conditions were applied. On the fourth and fifth day, supernatant containing the viral particles was collected and filtered with 0.45 µm PVDF filters (Millipore). RKO and SW837 were seeded at low density and infected overnight with the corresponding lentivirus (dilution 1:4 in fresh DMEM complete medium) in the presence of 4 µg/mL polybrene (Sigma-Aldrich-Aldrich). Two days after infection selection medium containing G418 (0.75 mg/mL and 0.5 mg/mL for RKO and SW837 respectively; Life Technologies) was applied to the cells. After selection, resistant cells were sorted to enrich the population of positive mCherry cells and MYO5B overexpression was confirmed by western blot. ***Downregulation cell line models:*** SKCOI and LS174T-W4 (overexpressing inducible STRAD/LKB1 pathway) [225] colon cancer cells were stably transduced with lentivirus carrying pINDUCER10-shRNA2, shRNA3, shRNA4 against *MYO5B* and shNT control, previously produced as described. Cells were selected with puromycin (0.75 µg/mL and 3 µg/mL respectively; Life Technologies). After selection, knockdown was confirmed by western blot. ***Knockout cell line model:*** Caco2 brush border enhanced subclone (Caco2-BBE colon cancer cells) [226] were transfected with pX458-sgRNA employing GeneJet reagent (SignaGen). GFP positive cells were sorted, seeded at low density on a 10 cm plate (~$2x10^4$ cells/plate) and grown until individual colonies were visible. Then, individual clones were picked and expanded. After DNA sequencing and characterization by western blot, nine knockout clones were further expanded and mixed ($5.5x10^6$ cells of each clone) to generate a policlonal knockout population. The mixed cells were seeded, expanded for other two days and frozen. Cells with low passage were used for all the experiments.

DNA extraction and sequencing. ***DNA extraction from mice:*** Genomic DNA extraction was performed from ear or tail clips following HotShot protocol [227]. Flp recombination in heterozygous *Myo5b*^{tm1c} mice was verified by sequencing after PCR amplification with Myo5b-F2 and Myo5b-R2 primers (**Figure 21 and Table 2**). After PCR, residual primers and nucleotides were removed from the reaction product by adding ExoSAP mix (0.1U Exonuclease I, Fermentas and 0.056 U Shrimp Alkaline Phosphatase, Roche). Samples were sent to Macrogen for sequencing. ***DNA extraction from cells:*** DNA from Caco2-BBE clones was extracted using DNAzol® (Invitrogen) according to manufacturer's instructions. Exon5 region CRISPR targeted was amplified using Myo5b-ex5-F and Myo5b-ex5-R primers (**Table 2**). ExoSAP and sequencing was conducted as previously described.

RNA extraction and quantitative real-time PCR (qPCR). Total RNA was extracted with TRIZOL® (Invitrogen) according to the instructions of the manufacturer and retro-transcribed using the High Capacity cDNA Reverse Transcription Kit (Applied Biosystems). Real time PCR reactions were performed in triplicate on a ABI PRISM 7500 Real-Time System (Applied Biosystems) using the SYBR green method or TaqMan Gene Expression Assay for the 18S house-keeping gene. MYO5B mRNA was amplified using the primers described in **Table 2**. The relative mRNA levels were calculated using the comparative ΔCt method as previously described [217].

mRNA expression microarray analysis. The levels of expression of more than 47,000 genes, including *MYO5B*, were investigated using GeneChip Human Genome U133 Plus 2.0 Array (Affymetrix) in a subset of 32 colorectal cancer cell lines. Data analysis was performed as described [228].

Protein extraction and quantification. To obtain whole protein cell lysates, cells were washed once with ice-cold PBS and harvested with a rubber sterile scraper. Cell pellets were collected in a micro tube by centrifugation at 2000 g for 5 min at 4°C and resuspended in radioimmunoprecipitation (RIPA) lysis buffer (0.1% SDS, 1% NP40 and 0.5% Na-deoxycholate in PBS) supplemented with protease inhibitors (Complete™, Mini, EDTA-free Protease Inhibitor Cocktail, Roche). After 30 min of incubation on ice, cells were sonicated for 10 sec 3 times at 20-50 kHz on ice, then the lysates were centrifuged at 16000 g for 20 min at 4°C for clarification and the supernatants were transferred into new microtubes and stored at -80°C. Protein content was assessed with a BCA™ Protein Assay Kit (Thermo Scientific). The protocol is the following: 2μl of test sample diluted in distilled water (final volume 25 μl) were mixed with 200 μl of BCA mixture in a 96 well plate. A series of BSA protein standards diluted in distilled water was run alongside with the protein lysates to establish a standard curve. The plate was incubated in the dark at 37ºC for 30 min prior to the measurement. The absorbance was read at 620 nm on a plate reader (Sunrise^{TM} model, TECAN Group Ltd.). Protein concentrations were determined by comparison with the BSA standard curve.

Western blot. ***Gel separation:*** Separation of proteins was performed by one dimensional SDS-PAGE electrophoresis assay as follows. Proteins were thawed on ice and 30-50µg were mixed with loading dye (25 mM Tris pH 6.8, 8% SDS, 40% Glycerol, 0.02% bromophenol blue, 400 mM mercaptoethanol) and denatured at 95°C for 5 minutes before being loaded into a polyacrylamide gel (4% stacking gel, 8% to 12% gradient running gel). The electrophoresis chamber was filled with 1x running buffer (0.025 M Tris, 0.19 M Glycine, 3.46 SDS mM). The current was set to 120V and proteins were left to migrate until the loading dye reached the lower edge of the gel. ***Transfer:*** After the protein separation step, the gels were removed from the glass plates and equilibrated in 1x transfer buffer (0.023 M Tris and 0.19 M Glycine) for 10 minutes at room temperature. For the transfer to a polyvinylidene difluoride (PVDF, Amersham) membrane, a wet blotting transference system was used. The membrane and filters were stacked as a "sandwich" together with filter papers and sponges. This setup was run at 100 V for 110 min in a chamber filled with ice-cold 1x transfer buffer. ***Blocking and Blotting:*** After protein transfer, the membrane was blocked with blocking buffer (5% skim milk in PBS-0.1% Tween) for 1 hour in order to prevent unspecific binding of the antibodies. The membrane was then incubated overnight at 4°C with the primary antibody at the concentration indicated on **Table 4**. Unbound antibody was removed by washing 3x 10 min with PBS-0.1%Tween. The membrane was then incubated for 1 h at room temperature with a secondary antibody conjugated with horseradish peroxidase at the concentration indicated in **Table 4**. ***Detection:*** Detection of the protein was achieved using Enhanced Chemiluminescence system (ECL, GE Healthcare), a light-emitting non-radioactive substrate for the horseradish peroxidase. Briefly, membranes were incubated with an equal volume of detection reagent A and reagent B for 1 min. Then, an X-ray film (AGFA) was exposed to the membrane to detect the chemiluminescent signal, and after automated film development the bands were visualized.

Flow citometry analysis. mCherry expression in RKO-EV/MYO5B/SP-MYO5B, SW837-EV/MYO5B/SP-MYO5B and RFP expression in SKCOI-sh2, sh3, sh4, shNT and LS174T-W4-sh2, sh3, sh4 and shNT was analyzed by flow citometry (BD LSRFortessa™). Briefly, overexpression and downregulation cell lines were treated or not with doxycycline (Dox; 0.1 µg/mL and 1 µg/mL respectively) for 48h prior tripsinization. Cells were then resuspended in PBS with 1 µg/mL of DAPI (Sigma-Aldrich-Aldrich).

Colocalization studies. To assess colocalization of mCherry-MYO5B and EGFP-RAB11A, TLA-HEK293 cells were seeded on gelatin-coated glass coverslips and cotransfected with 800 ng pINDUCER20-EV/pINDUCER20-MYO5B/pINDUCER20-MYO5B-S289X and 800 ng pEGFP-RAB11A-WT using PEI (Polyscience). The cells were treated with 0.1 µg/mL of Dox for 48 h. Then, the cells on coverslips were fixed with 4% paraformaldehyde (Sigma-Aldrich), permeabilized with 0.1% Triton X-100 and stained with DAPI (Sigma-Aldrich). Coverslips were mounted with ProLong® Gold antifade reagent (Life technologies) and observed under the confocal microscope (FV1000 Olympus).

Proliferation assay using Sulforhodamine B (SRB) method. SRB dye stains protein content and the absorbance measurement at 510 nm can be used for cell density calculation. ***Overexpression cell line models:*** $1x10^3$ RKO-EV/MYO5B/SP-MYO5B and $8x10^3$ SW837-EV/MYO5B/SP-MYO5B cells were seeded on a 96-well microtiter plate (8 replicates/cell line and condition). Dox (0.1 µg/mL) was added in the moment of the seeding and 50 µL of fresh medium with or without Dox was added at day 4. One plate was fixed with 30% Trichloroacetic Acid (TCA; Fisher Scientific) every 24h for 7 days. The plates were then stained with 0.4% SRB (Sigma-Aldrich) in 1% acetic acid for 30 min under agitation and washed with 1% acetic acid.

SRB precipitates were dissolved in 10 mM Tris pH10. Absorbance was measured at 510nm and plotted versus time. The experiments were carried out in triplicate. ***Downregulation and knockout cell line models:*** SKCOI-sh2, sh3, sh4 and shNT (12x10^3 cells) were seeded on a 96-well microtiter plate (8 replicates/cell linen and condition). To induce knockdown, the cells were pretreated with or without Dox (1 µg/mL) 72 h prior seeding. 50 µL of fresh medium with or without Dox was added at day 4. Caco2-BBE parental and knockout cell lines (4x10^3 cells) were seeded as described and 50 µL of fresh medium was added at day 4. Three independent experiments were carried out.

Clonogenicity assay. ***Overexpression cell line models:*** 5x10^2 RKO-EV/MYO5B/SP-MYO5B or SW837-EV/MYO5B/SP-MYO5B cells were seeded into 6-well plates with medium containing or not Dox (0.1 µg/ml) and allowed to attach and grow as individual colonies. The medium was replaced once per week (with or without Dox as corresponding). Once the colonies were visible, the plates were fixed with 1 mL methanol:acetic acid (3:1) for 5 min and stained with crystal violet (Acros organics) 1% in methanol for 10 min. The number of macroscopically visible colonies was scored blinded from the sample identity using ImageJ (https://imagej.nih.gov/ij/). At least, three independent experiments were carried out in triplicate. ***Downregulation and knockout cell line models:*** 5x10^2 SKCOI-sh3, sh3, sh4 and shNT were pretreated with or without 1 µg/ml Dox for 72 h and seeded into 6-well plates. Medium was renewed weekly with or without Dox, as corresponding. For Caco2-BBE, 2x10^3 parental and KO cells were seeded and medium was replaced once per week. At least, three independent experiments were carried out in triplicate.

Soft-agar colony formation assay. ***Overexpression cell line models:*** 2×10^5 RKO-EV/MYO5B/SP-MYO5B cells or 1×10^5 SW837-EV/MYO5B/SP-MYO5B were resuspended in complete DMEM medium containing 0.3% agar with or without 0.1 µg/ml Dox and plated onto 6-well plates on top of 0.6% agar in DMEM medium with or without 0.1 µg/ml Dox. For RKO, complete DMEM supplemented with 20% FBS was used instead. Cultures were grown until colonies were visible. The colonies were stained with nitro blue tetrazolium chloride (1 mg/ml; Sigma-Aldrich) and the number of macroscopically visible colonies was scored employing ImageJ. At least, three independent experiments were carried out in triplicate. ***Downregulation and knockout cell line models:*** SKCOI and Caco2-BBE cells did not show growth in soft agar.

Migration assay (Wound-Healing method). ***Overexpression cell line models:*** 2.25x10^6 RKO-EV/MYO5B/SP-MYO5B cells were seeded into 6-well plates with or without Dox (0.1 µg/ml) and allowed to grow until they reached 90% confluence. Then, the cell monolayer was scratched with a sterile micropipette tip and the wound region was allowed to heal by cell migration. The area that remained clear of cells at different time points within 48 h was quantified blinded from sample identity with Image J and compared with the area of the wound at time zero. Four independent experiments in triplicates were performed. SW837 cell line did not show migration capacity under this experimental setting. ***Downregulation and knockout cell line models:*** SKCOI-sh2, sh3, sh4 and shNT were pretreated with or without 1 ug/ml Dox for 72h prior seeding. Then, 2.5x10^6 cells were seeded and migration was quantified as described. Four independent experiments were carried out in triplicate. Caco2-BBE cell line did not show migration capacity under this experimental setting.

Migration assay (Boyden chamber method). ***Overexpression cell line models:*** SW837-EV/MYO5B/SP-MYO5B cells were pretreated with or without 0.1 µg/ml Dox for 48 h prior seeding. Then, 1x10^5 cells in 200 µL of DMEM supplemented with 1% FBS were seeded on the upper compartment of a Boyden chamber (Becton Dickinson; 8 µm pore size). 500 µL of DMEM supplemented with 10% FBS were added on the lower compartment, as chemoattracktant. The cells were allowed to migrate for 48 h at 37°C in 5% CO2. Then, the cells that remained in the upper part of the chamber were wiped out with a cotton swab, whereas the cells that had migrated to the lower surface of the filter were fixed in cold methanol for 5 min and stained with 5% crystal violet (Acros organics). The total number of migrated cells was determined by direct counting under the microscope (20X). Three independent experiments in triplicates were performed.

Matrigel invasion assay. The ability of cells to invade through Matrigel-coated filters was determined using a 24-well Boyden chamber (Becton Dickinson; 8 µm pore size) covered with 100 µl of 1 mg/mL Matrigel (Becton Dickinson). ***Overexpression cell lines:*** RKO-EV/MYO5B/SP-MYO5B and SW837-EV/MYO5B/SP-MYO5B cells were pretreated with or without 0.1 µg/ml Dox 48h prior seeding. Then, $6x10^4$ RKO cells were seeded in 100 µl DMEM containing 1 %FBS in the upper compartment of the chamber (on top of the matrigel layer). $1x10^5$ SW837-EV/MYO5B cells were seeded embedded in 100 µl of matrigel and 100 µl DMEM containing 1%FBS was added on top after polymerization. After incubation for 48 h at 37°C in 5% CO2, the cells that were unable to penetrate the filter were wiped out with a cotton swab, fixed and stained as previously described. The total number of invading cells was determined by direct counting under the microscope (20X). At least, three independent experiments in triplicates were carried out.

Differentiation and enzymatic activity assays. RKO-EV/MYO5B, SW837-EV/MYO5B and Caco2-BBE-parental/KO cells were grown for 21 days in confluence to induce spontaneous differentiation. Medium with or without 0.1 µg/mL Dox, as corresponding, was replaced every 2 days. Cellular pellets for protein extraction were collected at days 0, 2, 5, 7, 14 and 21 post-confluence. SKCOI-sh2, sh3, sh4 and shNT cells (previously pretreated with 1 µg/mL Dox for 72h) were seeded and grown for 72h with or without 1 µg/mL Dox in presence of 5 mM sodium butyrate, to induce differentiation. Total protein cellular lysates were obtained by extraction with mannitol buffer (50 mM D-mannitol, 2 mM Tris and 0.1% Triton X-100) containing protease inhibitors (Complete™, Mini, EDTA-free Protease Inhibitor Cocktail, Roche). Alkaline phosphatase (ALP), sucrase-isomaltase (SI) and dipeptidyl peptidase-4 (DPPIV) activity was assessed as follows. *For ALP activity assay:* 25 µg of protein (in a volume of 50 µl of mannitol buffer) were mixed with 150 µl of p-Nitro Phenyl Phosphate (NPP, Fisher

Scientific) and incubated at 37 ºC for 15 min in the dark. The absorbance was measured at 405 nm. *For SI activity assay:* 25 µg of protein in 12.5 µl of mannitol buffer were incubated with an equal volume of substrate (maltose 0.056 M in mannitol buffer, pH 6.0) at 37 ºC for 60 min. Heating at 100 ºC for 2 min stopped the reaction and the precipitate was resuspended on 250 µl of TGO buffer (horseradish peroxidase 5 mg (Sigma-Aldrich), glucose oxidase 4 mg (Sigma-Aldrich), ɑ-dianisidine 10 mg (Sigma-Aldrich) and 0.2 % Triton X-100 in a final volume of 100 ml of Tris 0.5 M, pH 7.0) and the absorbance measured at 450 nm. *For DPPIV activity assay:* 50 µg of protein in 90 µl of mannitol buffer were added to 10 µl of 1.4 M glycine-NaOH pH 8.7 and incubated in the presence of 100 µl of substrate (glycyl-L-proline-p-nitroanilide, final 1.5 mM; Santa Cruz) at 37 ºC for 30 min. The reaction was stopped with 800 µl of 32% TCA and samples were centrifuged at 1700 rpm for 10 min. Then, 50 µl of supernatant were added to 50 µl of cold 0.2% sodium nitrite and incubated at 4 ºC for 10 min. Next, 50 µl of 0.5% ammonium sulfamate were added and after 2 min of incubation, 100 µl of 0.05% n-(1-naphthyl)-ethanediamine (Sigma-Aldrich) were added and incubated at 37 ºC for 30 min in the dark. The absorbance was read at 548 nm. All these experiments were carried out three independent times in triplicate.

Dome formation in Caco2 cells. Caco2-BBE-parental and MYO5B knockout cells were grown for 21 days in confluence in 6-well plates. The number of domes was directly counted at different time points, blinded from the sample identity using an inverted microscope (10X). Three independent experiments in triplicate were performed.

Polarization experiments . The determination of the number of polarized LS174T-W4 [225] cells was determined as follows: LS174-W4 parental, sh3, sh4 and shNT cells were pretreated with 1 µg/mL Dox for 72 h to induce MYO5B knockdown. Then, cells were tripsinized and seeded on gelatin-coated glass coverslips and maintained with 1 µg/mL Dox to induce polarization. Plates were then incubated for 48 h and then fixed in 4% PFA (Sigma-Aldrich), permeabilized with 0.1% Triton X-100 and stained with

ALEXA488 labeled phalloidin (0.1 µM; Cytoskeleton) and DAPI (Sigma-Aldrich). Coverslips were mounted with ProLong® Gold antifade reagent (Life technologies). Polarization was scored using a fluorescent microscope (Olympus BX61). At least 500 polarized and unpolarized cells were scored blinded from the sample identity in three independent experiments carried out in triplicates. The percentage of polarized cells (polarized versus total number of cells) was calculated.

Subcutaneous Xenograft mouse model. All animal experiments were carried out under protocols approved by the Institutional Ethical Committee and the appropriate governmental agency. A minimum of 12 NOD/SCID animals (Harlan laboratory) 7-8 weeks old were injected with $3x10^6$ RKO-EV (left flank) and RKO-MYO5B (right flank); $1.5x10^6$ SW837-EV (left flank) and SW837-MYO5B (right flank); $10x10^6$ SKCOI-shNT (left flank) and SKCOI-sh4 (right flank) resuspended in 100 µl of PBS. In the case of SKCOI-sh4/shNT, the cells were pretreated with 1 µg/mL Dox for 72 h and the cells were resuspended in 100 µl of cold PBS with 50% matrigel (Becton Dickinson) for injection. The animals were then randomized in two groups (of a minimum of 6 animals), one receiving Dox *ad libitum* in drinking water (1 mg/ml Dox and 2.5% sucrose; Sigma-Aldrich) or a control group (2.5% sucrose). In the case of Caco2-BBE-parental and MYO5B knockout cells, the animals were injected with $6x10^6$ parental cells (left flank) and $6x10^6$ KO cells (right flank) in 100 µl of PBS. Tumor size was measured using a caliper three times per week. Tumor volume was calculated with the formula: V = (L × W2) × 0.5, where L is the length and W is the width of a xenograft. At end-point, the tumors were excised and processed to establish formalin-fixed paraffin-embedded samples for immunohistochemistry analysis.

Transmission electron microscopy. Duodenal samples were collected from *Myo5b* wild type and *Myo5b* knockout embryos at day 20 of gestation (E20; at least 3 animals per genotype). Samples were fixed with 2.5% glutaraldehyde and 2% paraformaldehyde and processed following standard procedures. Ultra-thin sections were mounted on copper grids, contrasted with uranyle acetate/lead citrate double-staining, and observed in a Jeol

JEM-1400 (Jeol LTD, Tokyo, Japan) transmission electron microscope equipped with a Gatan Ultrascan ES1000 CCD camera. The brush border architecture was evaluated on a minimum of 12 enterocytes per animal. Microvilli length (actin rootlet and actin core bundles) and microvilli density (microvilli/µm) were measured using ImageJ software. Duodenum biopsy sample from a MVID patient carrying a homozygous *MYO5B* nonsense mutation (c.4366C>T, p.1456X) was obtained after removal of the diseased intestine during the transplantation procedure [229]. The sample was fixed in 2% glutaraldehyde in phosphate buffer, rinsed in 6.8% sucrose in phosphate buffer, and postfixed in a solution of 1% osmium tetroxide in 0.1 mol/L sodium cacodylate buffer containing 11.2% potassium ferrocyanide. Samples were dehydrated with ethanol and processed according to standard procedures upon embedding. Ultra-thin sections were mounted on copper grids and contrasted with uranyle acetate and lead citrate double-staining.

Histology. *Myo5b* wild type and knockout E20 embryos were obtained and sacrificed on ice-cold PBS. Newborns were collected within 6 hours of birth, and sacrificed. Both embryos and newborn mice were weighted and measured using a caliper. Blood samples were obtained from tail clips of newborn mice in the moment of being sacrificed. Glucose levels were measured with a Glucocard G+ meter (Menarini diagnostics). The Small and Large intestines were dissected from embryos or newborn mice and then fixed overnight with 10% neutral buffered formalin (DiaPath). Adult *Vil-Cre*$^{ERT2;}$ *Myo5b*$^{tm1c/tm1c}$ and control mice were sacrified 5 days after tamoxifen administration. Their Small and Large intestines were obtained and fixed overnight with 10% neutral buffered formalin (DiaPath). Tumor samples from xenograft were extracted after sacrificing and fixed overnight in 10% neutral buffered formalin (DiaPath). After fixation, all the samples were transferred to a tissue cassette and dehydrated by serial immersion in 50%, 70%, 96% and 100% ethanol. Excess ethanol was removed by incubation in xylene three times for 1 h at room temperature and cassettes were then immersed in 65 ºC paraffin overnight. Tissues were further included in paraffin blocks. Then, 4 µm sections of all tissues were cut and placed on poly-L-Lysine coated microscope slides, incubated at 54 ºC for 1 h and deparaffined by immersion in xylene (2x5 min) and hydrated by serial immersion in 100 % ethanol (2x5 min), 96% ethanol (5 min), 70% ethanol (5 min), 50% ethanol (5 min) and distilled water prior staining. In parallel, formalin-fixed duodenal samples obtained from newborns and adult *Vil-Cre*$^{ERT2;}$ *Myo5b*$^{tm1c/tm1c}$ and control mice were cryoprotected in 15 % sucrose in PBS overnight, then transferred to 30 % sucrose solution overnight. Samples were then immersed in OCT (VWR) and frozen on dry-ice for cryosectioning.

Immunohistochemistry and immunofluorescence. For MYO5B, E-cadherin, β-catenin and BrdU immunostaining, the NovoLink polymer detection system (Novocastra Laboratories) was used. Immunostaining was carried out in 4 µm tissue sections, after deparaffination and antigen retrieval with 10 mM citrate buffer pH 6.0 in a pressure cooker for 4 min. Slides were counterstained with Mayer's haematoxylin and mounted with DPX mounting medium (Panreac Quimica). The primary antibodies used are described in **Table 4**. For Ezrin and Transferrin receptor immunostaining, epitopes were retrieved at 100°C for 20 minutes in 10 mM citric acid, 0.05% Tween 20 pH 6. For 5'-nucleotidase, epitopes were retrieved with 10 mM Tris Base, 1 mM EDTA Solution, 0.05% Tween 20, pH 9. Non-specific binding sites were blocked with 5% FCS and 1% BSA in PBS overnight. Primary antibodies were diluted in blocking solution with 0.05% Tween 20 at 37 °C for 2 h followed by 1 h incubation with Alexa-Fluor-488-conjugated (Ezrin and 5'-nucleotidase) or Alexa-Fluor-543-conjugated secondary antibody (Transferrin receptor). Primary antibodies used and corresponding dilutions are described in **Table 4**. Nuclei were stained with DAPI and slides were mounted with DAKO mounting medium. For alkaline phosphatase activity detection, slides were incubated with staining solution for a maximum of 1 h at 37ºC. Then, slides were counterstained with Mayer's haematoxylin and mounted with DPX mounting medium (Panreac Quimica). Staining solution contains 0.4 mg/mL 5-Bromo-4-chloro-3-indolyl phosphate p-toluidine (Sigma-Aldrich), 0.5 mg/mL of nitro blue tetrazolium (Sigma-Aldrich), 100 mM $MgCl_2$ (Sigma-Aldrich), 2 mM Levamisole hydrochloride (Santa Cruz Biotechnology), 5 mM Sodium azide (Sigma-Aldrich) and 0.15

mM of 1-methoxy-5-methylphenazinium methyl sulphate in 100 mM Tris pH 9.5 (Sigma-Aldrich). Periodic acid-Schiff staining was performed after deparaffination. Briefly, the slides were immersed in 0.5 % periodic acid solution (Sigma-Aldrich) for 5 min, washed in distillated water and placed in Schiff reagent (Sigma-Aldrich) for 15 min. Then counterstain with haematoxylin and mounted. For F-Actin staining, 10 µm thick duodenal cryosections were stained with rhodamine phalloidin (Cytoskeleton), nuclei were counterstained with DAPI and slides were mounted with ProLong® antifade reagent (Invitrogen). Fluorescence microscopy pictures were taken with a confocal microscope (FV1000 Olympus).

Table 4. Antibodies used in the study.

Antibody	Source	Reference clone	Host	Application (dilution)
MYO5B	Atlas Antibodies	HPA040902	Rabbit	WB[1] (1:500)
MYO5B	Atlas Antibodies	HPA040902	Rabbit	IHC[2] (1:800)
MYO1A	Proteintech	17499-1-AP	Rabbit	WB[1] (1:500)
Sucrase Isomaltase	DSHB	HBB2/614/88	Mouse	WB[1] (1:10)
E-cadherin	BD Bioscience	610181	Mouse	WB[1] (1:1000)
E-cadherin	BD Bioscience	610181	Mouse	IHC[2] (1:000)
β-catenin	BD Bioscience	610154	Mouse	IHC[2] (1:100)
Ezrin	Tebu Bio	R12-2760-2	Rabbit	IHC[2] (1:100)
TfR	Invitrogen	H68-4	Mouse	IHC[2] (1:100)
5’-Nucleotidase	Abgent	-		IHC[2] (1:50)
BrdU	Developmental studies	G3G4	Mouse	IHC[2] (1:15)
Polyclonal Swine Anti-Rabbit Immunoglobulins/HRP	Dako	P0217	Goat	WB[1] (1:5000)
Polyclonal Swine Anti-Mouse Immunoglobulins/HRP	Dako	P0447	Goat	WB[1] (1:5000)
Alexa Fluor® 488 conjugate	Invitrogen	A1134	Goat	IF[3] (1:1000)
Alexa Fluor® 594 conjugate	Invitrogen	A11032	Goat	IF[3] (1:700)

[1]WB: western blot; [2]IHC: immunohistochemistry; [3]IF: immunofluorescence

Quantification of BrdU positive cells. Pictures of the BrdU immunohistochemistry from intestine of E20 wild type and Myo5b knockout embryos, as well as from adult *Vil-Cre*$^{ERT2;}$ *Myo5b*$^{tm1c/tm1c}$ and control mice were obtained. Then, the number of positive BrdU cells in at least 9 crypts per mice was scored using ImageJ, blinded from the animal identity. The percentage of BrdU positive cells was determined dividing by the total number of cells per crypt.

Quantification of the total number of cells per villi or crypt. Pictures of the hematoxilin and eosin staining from the intestines of E20 wild type and Myo5b knockout embryos, as well as from adult *Vil-Cre*$^{ERT2;}$ *Myo5b*$^{tm1c/tm1c}$ and control mice were obtained. Then, the total number of cells in a minimum of 9 villi or crypts per animal was scored using ImageJ, blinded from the animal identity.

Clinical Samples. Samples from colorectal cancer patients with locally advanced disease (Dukes C) were collected at collaborating medical institutions in Spain and Finland as previously described [230]. Informed consent for genetic analysis of the tumor sample was obtained from each patient, according to protocols approved by the human investigations and Ethical Committee in the appropriate Institution. For tissue microarray preparation, areas containing a high proportion of tumor cells were selected after histological examination of haematoxylin and eosin stained tumor sections. Triplicate 0.6-mm cores from every sample were arrayed in a fresh paraffin block using a Beecher Instrument tissue arrayer (Silver Spring, MD). Unstained 4-mm sections from the tissue microarray were mounted on slides coated with 3-aminopropyl-triethoxy-silane (Sigma-Aldrich). A total of 155 patients Duke C colorectal tumors were used for immunohistochemical assessment of MYO5B levels. The mean follow up of the patients was 9.2 years (ranging from 6.8 to 11.2 years).

Tissue Microarray (TMAs) analysis. MYO5B staining levels were scored using a semiquantitative scale from 0 (absence of MYO5B immunostaining) to 3 (highest immunostaining). MYO5B expression was evaluated blinded from the clinical data. For Kaplan-Meyer plots, MYO5B levels were dichotomized as low or high MYO5B using an average score cutoff value calculated with cutoff finder web server (http://molpath.charite.de/cutoff/). The clinicopathological features of the patients are shown in **Table 5**.

RESULTS

1. MYO5B in the physiology of the normal intestinal epithelium

1.1 Generation and validation of *Myo5B* knockout mice.

We have developed the first animal model with conditional inactivation of *Myo5b.* For this purpose a knockout first strategy was used combining the advantages of both a reporter-tagged and a conditional mutation [219,220]. Thus, homologous recombination was used to introduce a targeting cassette including the mouse En2 splice acceptor and the SV40 polyadenylation sequences after exon 4 of *Myo5B*, which is predicted to generate a null allele through splicing to a lacZ ‵‵gene trap′′ element (Tm1a null allele, **Figure 22A**). The targeted allele with conditional potential (Tm1c conditional allele) was obtained after crossing the animals with Flp deleter mice [221]. The Flp recombinase removes the gene-trap cassette reverting the mutation to wild type and leaving loxP sites on either side of the critical exon (**Figure 22A**). The recombination was verified by DNA sequencing (data not shown). To generate an intestinal-epithelium specific allele with conditional potential, the animals were crossed with $Vil\text{-}CRE^{ERT2}$ mice [222] that express a tamoxifen-inducible form of the Cre recombinase under the control of the intestine specific *Villin* promoter (**Figure 22A**). Two homozygous and two heterozygous $Myo5b^{tm1c}$ mice that were wild type for the $Vil\text{-}CRE^{ERT2}$ transgene were used as control. As expected, mice homozygous for the trapped allele ($Myo5b^{tm1a(KOMP)Wtsi/tm1a(KOMP)Wtsi}$; henceforth referred to as *Myo5b* knockout mice) showed no myosin VB expression in their small and large intestine compared to their wild type littermates (**Figure 22B-E**). No differences in the MYO5B staining were observed between homozygous and heterozygous $Myo5b^{tm1c}$ control mice 5 days after tamoxifen administration (data not shown), therefore animals with both genotypes were included in the same group, henceforth referred to as control mice. As expected, Myo5b expression in the small and large intestine of adult $Vil\text{-}CRE^{ERT2}$; $Myo5b^{tm1c/tm1c}$ (henceforth referred to as Myo5B intestinal-epithelium specific knockout mice, iKO) is lost after tamoxifen injection (**Figure 22F-I**).

1.2 Gross phenotype of *Myo5B* knockout and *Myo5B* intestine-specific knockout mice.

The gross phenotype of knockout embryos and newborn mice as well as epithelium intestine-specific knockout adult mice was characterized. Wild type, heterozygous or *Myo5b* knockout embryos at day 20 of gestation (E20) showed no difference in their size or weight (**Figure 23A-B**). Animals were born at Mendelian ratios (n=99; Chi-square test, p=0.14; **Figure 23C**), but *Myo5b* knockout mice invariably died within the first 12h after being born (**Figure 23C**). No differences were observed between wild type and knockout newborn mice in their body size (**Figure 23E**) or the gross histology of the gastrointestinal tract or other organs studied, including the lungs, liver, central nervous system, heart, pancreas and spleen. No cyanotic episodes or respiratory distress was observed in *Myo5b* knockout mice. However, newborn *Myo5b* knockout mice showed reduced bodyweight compared to wild type and heterozygous mice (**Figure 23F**). In the case of epithelium intestine-specific knockout adult mice a progressive reduction in their body weight was also observed from the day of tamoxifen administration (**Figure 23G**). The reduction was significant compared to control animals from day 3 post-injection, reaching an average accumulated weight loss of 17.1 % at day 5 post-injection (**Figure 23G**). Moreover, knockout newborn mice showed signs of diarrhea and wrinkled skin, possibly due to dehydration (**Figure 23H**). Although newborn *Myo5b* knockout mice showed no suckling defects (presence of a milk spot; **Figure 23H**), they had significantly reduced blood glucose levels compared to wild type and heterozygous littermates (**Figure 23I**). Epithelium intestine-specific knockout adult animals also showed diarrhea (**Figure 23J-K**) and signs of dehydration as revealed by a decreased skin turgor. The intestine was totally empty of solid content or feces and displayed an accumulation of liquid content (**Figure 23K**). All these results are consistent with the watery diarrhea and absorption defects observed in patients with MVID [181] and likely contributed to the death of the animals.

Figure 23. Phenotype of *Myo5b* knockout and *Myo5b* intestine-specific knockout mice. Size **(A)** and weight **(B)** of E20 embryos by *Myo5b* genotype. **(C)** Genotype of 99 mice born from crossing heterozygous *Tm1a* male and female mice. **(D)** Percentage of these 99 mice that were alive 12h after birth. Size **(E)** and weight **(F)** of newborn mice by *Myo5b* genotype. Newborn wild type **(G)** Percentage of body weight changes of the adult control and intestine-specific (iKO) adult mice after tamoxifen administration (4 mg/ 25g at day 0). **(H)** Newborn mice showing the presence of the milk spot (white arrowhead), wrinkled skin (black arrowhead) and evidence of diarrhea (arrow). **(I)** Histogram showing average blood glucose levels in *Myo5b* wild type, heterozygous and newborn mice. **(J)** Adult iKO mouse showing diarrhea (arrow) at day 5 post-injection. **(K)** Adult control and iKO mice sacrificed at day 5 post injection. iKO mouse showed evidence of diarrhea (arrow) and accumulated fluids in the intestine compared to control mice (asterisk). The mean (± SEM) is shown in all histograms. N= number of animals per group. $^{*}p<0.05$; $^{***}p<0.001$; Student’s t-test.

1.3 Mislocalization of apical brush border proteins in the enterocytes of *Myo5b* knockout and *Myo5b* epithelium intestine-specific knockout mice.

The intestinal enterocytes of *Myo5b* knockout newborn mice showed the characteristic cytoplasmic accumulation of periodic-acid Schiff (PAS) staining observed in MVID patients [182,183] (**Figure 24A-B**). Moreover, proteins normally expressed in the apical membrane of intestinal enterocytes were also mislocalized; alkaline phosphatase (ALP; **Figure 24C-D**), was accumulated in the subapical region of the cell whereas 5'-nucleotidase (5’NT; **Figure24 E-F**) and ezrin (**Figure24 G-H**) mislocalized to the basolateral membrane or the cytoplasm. Ezrin-coated vesicles were also found in the cytoplasm. Transferrin receptor was accumulated in the basal cytoplasm of enterocytes from *Myo5b* knockout mice (**Figure 24I-J**), while other basolateral markers such as E-cadherin (**Figure 24K-L**) and β-catenin (**Figure 24M-N**) were unaffected. Notably, in some epithelial cells of *Myo5b* knockout mice, ezrin (**Figure 24G-H**) and actin (**Figure 24O-P**) were found in circular cytoplasmic structures, closely resembling microvillus inclusions. Importantly, these structural defects were also observed in E20 embryos (**Figure 25**).

The enterocytes of *Myo5b* intestine-specific knockout adult mice showed a similar distribution pattern of the brush border and basolateral markers to that found in *Myo5b* knockout embryos and newborn mice. First, the accumulation of periodic-acid Schiff (PAS) staining in the subapical region was observed and was particularly strong in the apical part of the villi (**Figure 26A-B**). The apical brush border protein alkaline phosphatase (ALP) mislocalized to the subapical region and occasionally to intracitoplasmic rounded structures (**Figure 26C-D**). Actin staining was observed highly reduced from the apical brush border region in the enterocytes of *Myo5b* intestine-specific knockout mice compared to control mice (**Figure 26E-F**). In general, actin staining revealed a less compact structure with enterocytes that are protruding from the epithelial monolayer (**Figure 26E-F**). In addition, DAPI staining of the nuclei indicates that the monolayer of epithelial cells is generally disorganized in *Myo5b* intestine-specific knockout mice compared to control mice, reflecting a loss of polarity. Microvillus inclusions were also found (**Figure 26E-F**). Localization of the basolateral protein markers E-cadherin and β-catenin was also studied. E-cadherin was found redistributed from the apical region of the enterocytes to the basal pole in *Myo5b* intestine-specific knockout mice compared to control mice (**Figure 26G-H**). However, not significant changes in the localization of β-catenin were found (**Figure 26I-J**).

1.4 Structural defects in the brush border of enterocytes of *Myo5b* knockout mice.

Transmission electron microscopy (TEM) analysis of the intestinal epithelium of *Myo5b* knockout E20 embryos revealed widespread microvilli atrophy (shorter microvilli) and reduced packing with areas with few/absent microvilli in the apical surface of the enterocytes (**Figure 27A-C and I**). However, the length of the microvilli actin rootlet did not show differences (**Figure 27A-B**). In some cells, an abnormal localization of microvilli to the lateral plasma membrane was also observed (**Figure 27E-F).** In addition, microvillus inclusion bodies were detected in the cytoplasm of the enterocytes (**Figure 27H-I**). Vesicles were frequently observed at the apical plasma membrane in *Myo5b* wild type mice but not in the *Myo5b* knockout animals, where a characteristic accumulation of vesicles could be observed underneath the terminal web (**Figure 27A** and **F-G**). These ultrastructural abnormalities closely resemble the phenotype observed in the intestinal epithelium of patients with MVID (**Figure 28D-F**) [183,188].

2. MYO5B in colorectal cancer

2.1 Generation of colon cancer cell lines with inducible MYO5B expression.

To explore the role of MYO5B in colorectal cancer, we have engineered novel isogenic cell line systems with doxycycline inducible MYO5B expression employing the pINDUCER lentiviral toolkit [223]. As recipients, we chose two colorectal cancer cell lines; RKO (microsatellite instability phenotype (MSI), mutant for *BRAF* and *PI3KCA*) and SW837 (microsatellite stable phenotype (MSS), mutant for *KRAS*, T*P53* and *APC*). Both cell lines show low endogenous levels of MYO5B as measured at the mRNA (microarray and qPCR, **Figure 29A-B**) and protein level (**Figure 29C**). MYO5B mRNA expression was determined using microarray analysis with two different probes and validated by qPCR (Person's $r>0.8$ and $p<0.0001$ **Figure 29D**). RKO and SW837 parental cell lines were stably transfected with a vector expressing human MYO5B fused to mCherry at its N-terminal end (mCherry-MYO5B) or the corresponding empty vector control (mCherry). After selection and FACS/sorting enrichment, the cell lines generated were analyzed by flow cytometry detecting an 80% and 81% of mCherry positive cells for RKO-EV and RKO-MYO5B (**Figure 30A**) and 94.1% and 72% for SW837-EV or SW837-MYO5B respectively (**Figure 30B**). A bimodal distribution of mCherry-MYO5B was observed in both RKO-MYO5B and SW837-MYO5B cell lines. These "superpositive" populations were sorted and expanded as independent cell lines called RKO or SW837-superpositive-MYO5B (henceforth referred as RKO-SP-MYO5B or SW837-SP-MYO5B). After flow citometry analysis a 97.8% and 87% of positive mCherry cells was detected for RKO-SP-MYO5B and SW837-SP-MYO5B respectively (**Figure 30A-B**). Dox-dependent expression of MYO5B was confirmed by western blot in a range of Dox concentrations (**Figure 30C-D**) for both cell lines; 100 ng/mL of Dox was selected as the appropriate concentration to use for further experiments in both cases. Transgene overexpression was determined at different times after 100 ng/mL Dox exposure and maximum MYO5B expression was observed at 36 h in both cell lines (**Figure 30E-F**).

The MYO5B expected intracellular localization is mainly cytoplasmic since it is an actin interacting protein involve in membrane recycling [101]. The proper localization of MYO5B in the isogenic models generated was confirmed by *"in vivo"* fluorescence microscopy, observing a cytoplasmic localization of the protein for both RKO-MYO5B/SP-MYO5B and SW837-MYO5B/SP-MYO5B, whereas a uniform cellular distribution was observed for the corresponding EV controls (**Figure 31A-B**). Moreover, MYO5B functionality was validated by colocalization with its well-established interacting protein RAB11A in HEK293 cells (**Figure 31C-E**). RAB11A showed a intracytoplasmic dotted pattern that did not colocalize with mCherry (EV control, **Figure 31C**) or MYO5B mutant negative control (S289X) with a premature STOP codon in the head region (**Figure 31D**). However, colocalization between the full-length MYO5B and RAB11A was detected (**Figure 31E**).

2.2 Generation of colon cancer cell lines with inducible MYO5B downregulation and MYO5B knockout.

To explore the role of MYO5B in colorectal cancer isogenic cell line systems with doxycycline inducible expression of a bicistronic transcript (turbo RFP-shRNA) for MYO5B downregulation were engineered, using the pINDUCER lentiviral toolkit [223]. SKCO1 (MSS, mutant for *APC* and *KRAS*) and LS174T-W4 (MSI, mutant for *KRAS, PI3KCA* and *CTNB1*) [225] were used as recipients since they show high endogenous levels of MYO5B, measured at the mRNA and protein level (**Figure 29**). Parental cell lines were stably transfected with vectors containing three different shRNA sequences (shRNA-2, shRNA-3 and shRNA-4) and a non-target control (shRNA-NT). After puromycin selection, the percentage of RFP positive cells was established by flow citometry, obtaining: 98.1% (SKCO1-sh2), 95.7% (SKCO1-sh3), 93.6% (SKCO1-sh4) and 64% (SKCO1-shNT) (**Figure 32A**). In the case of LS174T-W4: 77% (LS174T-W4-sh2), 90% (LS174T-W4-sh3), 75% (LS174T-W4-sh4) and 72% (LS174T-W4-shNT) (**Figure 32B**). Downregulation was confirmed by western blot after treatment of the different cell lines with 1 µg/mL Dox for 72 and 96h (**Figure 32C-D**). Note that LS174T-W4-sh2 did not show downregulation.

Caco2 subclone known as brush border enhanced (Caco2-BBE cells; MSS, mutant for *APC*, *CTNB1* and *P53*) [231] were selected for MYO5B knockout using CRISPR/Cas9. Parental Caco2-BBE cells were transiently transfected with pX458-sgRNA against MYO5B. Transfected GFP positive cells were sorted, seeded at low density and allowed to grow as individual clones. After expansion, 21 clones were analyzed by DNA sequencing of the targeted exon 5 (**Figure 32E**) and MYO5B protein levels by western blot (**Figure 32F**). A total of 17 clones (80.9%) showed MYO5B mutations and loss of MYO5B protein, whereas 1 clone was heterozygous (4.7%) and 3 clones had no MYO5B mutations (14.3%). Only nine of the knockout clones that showed a clear DNA sequence with insertions/deletions of less than 20 bp were selected and pooled together. The absence of MYO5B protein expression in the polyclonal knockout (henceforth referred as knockout, KO)

2.3 Loss of MYO5B increases proliferation of the intestinal epithelium and colon cancer cells *in vivo*

The intestinal epithelium shows the fastest renewal rate among all the tissues in the body. The intestinal crypts contain proliferating cells that migrate upwards into the villi and gradually differentiate. To further characterize the role of MYO5B in cell proliferation of the normal intestine, *Myo5b* knockout mice were used. Pregnant females at day 20 of gestation were intraperitoneally injected with 100 mg/Kg BrdU two hours before being sacrificed. The embryos were obtained and the number of BrdU positive cells in the intestinal epithelium was determined by anti-BrdU immunostaining. The results showed a significant increase in the percentage of BrdU-positive cells in the intervillus regions (that are further replaced by crypts) of the knockout embryos compared to the wild-type littermates (**Figure 33A-C**).Moreover, the total number of cells per villi and intervillus region was counted and no differences were observed compared to their wild type littermates (**Figure 33D-F**). The same experimental layout was carried out with adult *Vil-Cre* ^{ERT2}*;MYO5B*$^{tm1c/tm1c}$ mice injected with 4 mg of tamoxifen 5 days before. The intestine-specific *Myo5b* knockout mice showed significant hyperproliferation in their crypts compared to control mice (**Figure 33G-I**). Moreover, they showed smaller villi (reduction in the total number of cells per villi) and enlarged crypts (as observed by an increase in the number of total cells per crypt; **Figure 33J-L**), compared to control mice.

Figure 33. Effects of *Myo5b* knockout on the proliferation of normal intestinal epithelium. (A-B) BrdU immunostaining of small intestine sections of a WT **A)** and KO **B)** embryo. **(C)** The average (±SEM) percentage of proliferating cells (BrdU positive) is shown for both WT and KO embryos. **(D-E)** Hematoxilin and eosin staining of small intestine sections of a WT **D)** and KO embryo **E)**. **(F)** The average (±SEM) of the total number of cells per villi and intervillus region (that will further be replaced by crypts) is shown for both WT and KO embryos. **(G-H)** Representative BrdU immunostaining for a control **G)** and intestine-specific, iKO **H)** adult mouse. **(I)** The average (±SEM) percentage of proliferating cells (BrdU positive) cells for both control and iKO adult mice. **(J-K)** Hematoxilin and eosin staining of small intestine sections of a control **J)** and iKO **K)** adult mouse. **(L)** The average (±SEM) of the total number of cells per villi and crypt is shown for both control and iKO adult mice. Cnt indicates control. Scale bar is 25 µm. N represents number of animals per group. *p<0.05; ***p<0.001; Student's t-test.

Uncontrolled cell growth represents a critical initial event for cancer development [45]. There are numerous studies demonstrating the opposing relationships between differentiation and proliferation, two processes that are tightly regulated in rapidly proliferating normal tissues. Many of the genetic alterations found in cancer cells abrogate the precise balance between these two processes, favoring cell division [45,232]. The isogenic and knockout models previously described were employed to study the role of MYO5B in the proliferation capacity of colon cancer cells *in vitro*. First, the effect of the doxycycline-controlled reintroduction of MYO5B into RKO and SW837 cell lines was assessed. The results show no differences in their proliferation capacity, measured by the sulforhodamine B staining method as a surrogate for cell number (**Figure 34A-B**). The downregulation of MYO5B in SKCO1 cells using doxycycline-inducible shRNAs did not show differences in their proliferation rate (**Figure 34C**). Moreover, MYO5B knockout in Caco2-BBE cells did not affect their proliferation rate, confirming the result obtained for the other cell lines (**Figure 34C**).

Figure 35. Effects of MYO5B on the clonogenicity and anchorage-independent growth of colon cancer cells. (A-B) Number of colonies counted in the clonogenic assay for the MYO5B overexpressing cell lines RKO **A)** and SW837 **B)** with their corresponding EV controls with and without 100 ng/mL Dox. **(C)** Number of colonies counted in the clonogenic assay for SKCO1 derivative cell lines with inducible MYO5B knockdown and the corresponding NT control, with and without 1 µg/mL Dox. **(D)** Number of colonies counted in the clonogenic assay for Caco2-BBE cells knockout for MYO5B compared to the parental control. **(E-F)** Anchorage independent growth of the cells in soft agar is shown for MYO5B overexpressing cell lines RKO **E)** and SW837 **F)** with the corresponding EV controls. The mean (±SEM) of at least three independent experiments carried out in triplicates is shown. n/s is not significant, $p>0.05$ Student's t test.

Next, the effects of MYO5B in tumor growth were investigated *in vivo* using a subcutaneous xenograft model of the different cell lines generated. RKO and SW837 cells stably expressing MYO5B or empty vector control were subcutaneously injected in the left or right flank, respectively, of NOD/SCID immunodeficient mice. The animals were randomized in two groups that were treated or not with 1 mg/mL Dox. No differences were observed in the growth of the xenografts formed by these cell lines in the animals treated with doxycycline versus control mice (**Figure 36A-B**). Similarly, Caco2-BBE cells knockout for MYO5B and parental control cells did not show differences in their growth as subcutaneous xenografts (**Figure 36D**). In contrast, SKCO1 cells expressing shRNA4 against MYO5B or a non-target control shRNA showed significant differences in the tumor growth of the cells upon doxycycline treatment (**Figure 36C**).

2.4 MYO5B regulates polarization and differentiation of colon cancer cells.

MYO5B is involved in the polarization and differentiation of normal intestinal epithelial cells and its inactivation has been shown to cause the complete loss of the polarized structure of the enterocytes causing MVID. Moreover, loss of polarization and differentiation is important in the initial stages of intestinal tumorigenesis [217] and is a hallmark of advance metastatic carcinomas [233]. To study the functional role of MYO5B in polarization of colon cancer cells, we stably knocked down MYO5B levels in LS174T-W4 cells. This cell line has been transduced with inducible STRAD pseudokinase that, upon doxycycline exposure, results in LKB1/STK11 activation and complete polarization of the cells with the formation of a brush border (**Figure 37A**) [225]. We found a reduction in the percentage of polarized cells using two different shRNA sequences against MYO5B, compared to the shNT control (**Figure 37B**). The reduction is significant in the case of sh4 (**Figure 37B**). This result indicates a role of MYO5B in the polarization capacity of colon cancer cells.

Several colon cancer cell lines can undergo spontaneous enterocytic differentiation when grown in confluence [234]. One of the best characterized models is the colon carcinoma derived cell line Caco2 [235] where the spontaneous differentiation process leads to the formation of a monolayer of cells expressing several morphological and functional characteristics of the mature enterocyte. Caco2-BBE (brush border enhanced) cells have been reported to form a faithful replica of the enterocyte brush border in both structure and composition [231]. Employing our MYO5B knockout Caco2-BBE cells we tried to elucidate the role of this protein in the polarization of colon cancer cells. First, we grew 3-D cultures of Caco2-BBE cells in a matrigel matrix. The cells divide and group into cyst structures developing a brush border oriented towards the lumen of the cyst (**Figure 37C-D**). Confocal images of F-actin stained 3-D cysts show defects in the ability of the cells to polarize and form a lumen (**Figure 37D-E**), compared to the parental cell line. Moreover, the cells present microvillus inclusions and redistribution of F-actin consistent with polarity defects (**Figure 37E**).

Then, Caco2-BBE cells were allowed to differentiate for 20 days in confluence. During this process, the confluent monolayer of cells form domes or “semicysts” structures, due to vectorial electrolyte transport resulting in fluid accumulation in localized areas of the monolayer (**Figure 37F**) [236]. The number of domes was directly counted under the microscope at different time points during the differentiation process, observing a significant decrease in the number of these structures in the MYO5B knockout cells compared to parental control cells (**Figure 37G**).

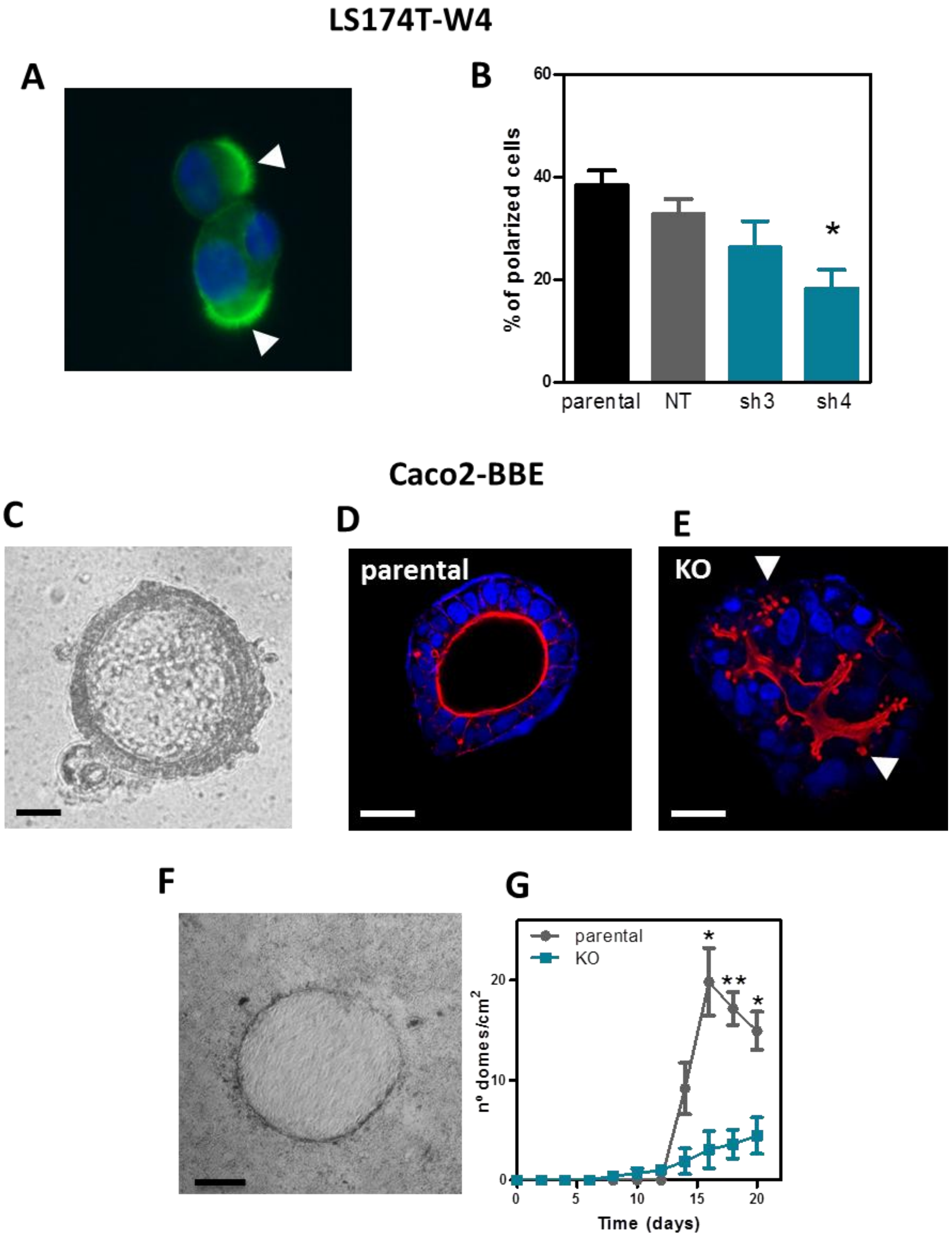

Figure 37. Effects of MYO5B inactivation in the polarization of colon cancer cells. (A) Representative image of F-actin staining (green) in a polarized LS174T-W4 parental cell . The brush border is indicated with a white arrowhead. **(B)** The average percentage of polarized LS174T-W4 cells was determined after MYO5B downregulation with two different shRNAs (sh3 and sh4) and compared to shNT. The knockdown was induced with 1 µg/mL Dox for 72 h. Then, cells were tripsinized and seeded on glass coverslips and allowed to polarize for a other 48 h in presence of Dox. Polarized cells were defined by the characteristic accumulation of actin in one pole of the cell as shown in **A). (C-D)** 3-D Caco2-BBE cultures in matrigel. The cells polarize in cyst structures observed like bubbles in transmission light microscopy **C)**. Actin and DAPI staining of cysts is shown for parental Caco2-BBE **D)** and KO **E)** cells. Scale bar represents 30 µm. **(F-G)** Caco2-BBE cells form domes or semicysts structures **F)** that were counted and plotted versus time for parental and KO Caco2-BBE cells **G)** Scale bar represents 200 µm. The mean (±SEM) of at least three independent experiments carried out in triplicates is shown*$p<0.05$; **$p<0.01$ by Student’s t-test.

We have also investigated the role of MYO5B in colon cancer cells differentiation by measurement the enzymatic activity of alkaline phosphatase (ALP), Dipeptidyl peptidase-4 (DPPIV) and Sucrase Isomaltase (SI). These three proteins are well-established brush border markers of enterocyte differentiation [217,237–239]. Thus, RKO and SW837 isogenic models with inducible MYO5B overexpression, as well as Caco2-BBE cells knockout for MYO5B were maintained in confluent culture for 21 days and the activity of these markers was monitored over this time course. As expected, the activity of these three hydrolases progesively increased with time in confluent culture. ALP activity was observed slightly increased in the case of SW837 cells overexpressing MYO5B at day 21, compared to the control without Dox (**Figure 38A**). No changes could be observed for RKO cell line (**Figure 38B**). None of the other two markers, SI and DPPIV, showed an increase in their activity for RKO and SW837 control or MYO5B overexpressing cell lines (data not shown). For Caco2-BBE cells, ALP and SI activity was observed significantly reduced in the case of MYO5B knockout cell line, compared to parental (**Figure 38C-D**). DPPIV did not show changes in Caco2-BBE cells (**Figure 38E**). To further confirm the role of MYO5B in differentiation, protein extracts were obtained from Caco2-BBE MYO5B knockout and parental cells at different time points of the differentiation process. Western blot (**Figure 38F**) confirmed MYO5B knockout and showed no changes in the levels of MYO5B protein along the differentiation process. However, SI levels increased after differentiation in the case of parental cell line. Strikingly, much reduced SI protein could be detected for the case of knockout cells, validating the previous observation in SI activity measurement (**Figure 38D-F**). Brush border myosin IA protein levels also increased during the differentiation process in parental control cells whereas MYO1A levels did not follow the same pattern in MYO5B knockout cells (**Figure 38F**) E-cadherin protein levels slightly increased at day 14 and 21 of the differentiation process in both MYO5B knockout and parental Caco2-BBE cells. However, no differences between them were observed (**Figure 38F**).

Exposure to butyrate, a short-chain fatty acid produced by the colonic bacterial fermentation, is known to induce cell growth inhibition and differentiation in colon cancer cells through its capacity to inhibit histone deacetylases [217,240,241]. Thus, SKCO1 cells with inducible MYO5B downregulation along with the NT control were induce to differentiate employing this approach. A >10 fold increase in ALP activity was observed in SKCO1 cells after sodium butyrate treatment (5 mM) for 72h. However, ALP activity levels did not show differences between the MYO5B Knockdown and control cells (**Figure 38G**). SI and DPPIV activity were not increased after sodium butyrate treatment (data not shown).

Figure 38. Effects of MYO5B inactivation on the differentiation of colon cancer cells. (A-B) Alkaline phosphatase (ALP) activity levels at different time points during the differentiation process of SW837-MYO5B and SW837-SP-MYO5B **A)**; RKO-MYO5B and RKO-SP-MYO5B **B)** and the corresponding EV controls, with or without 100n g/mL Dox. **(C-E)** Activity levels of ALP (a representative experiment is shown) **C)**, sucrase isomaltase (SI) **D)** and dipeptidyl peptidase 4 (DPPIV) **E)** during the differentiation process of Caco2-BBE knockout for MYO5B and parental control. **(F)** Western blot showing MYO5B, SI, MYO1A and E-cadherin protein levels at different time points of the differentiation process for Caco2-BBE MYO5B knockout and parental control cells. β-tubulin is used as loading control. The arrow indicates MYO5B band. Cnt indicates control (SKCO1 cell line). **(G)** Induced alkaline phosphatase activity after sodium butyrate treatment (5 mM for 72 h) of SKCO1 cells with inducible MYO5B downregulation (1 µg/mL Dox) and shNT control. ALP activity is represented as fold increase relative to un-induced controls. The mean (±SEM) of three independent experiments carried out in triplicates is shown. *p<0.05; **p<0.01; n/s is not significant p>0.05 by Student's t-test.

In addition, using a cohort of 153 Dukes C colorectal cancer cases, we found that the levels of MYO5B protein expression assessed by immunohistochemistry with a MYO5B specific antibody (**see Figure 41A-B**) were significantly lower in poorly differentiated tumors (G3) compared to moderately differentiated (G2) and differentiated colorectal tumors (G1), further indicating that MYO5B regulates the differentiation of colorectal cancer cells (**Figure 39**).

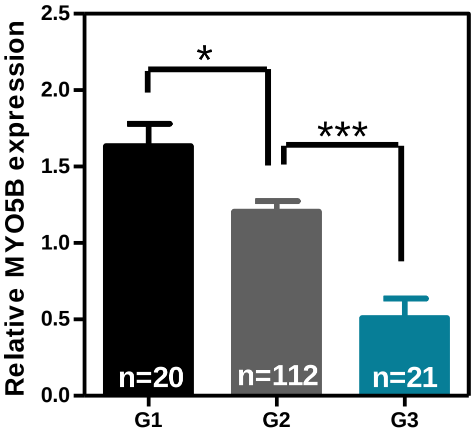

Figure 39. MYO5B tumor expression and grade of differentiation of primary colorectal tumors. The levels of MYO5B immunostaining (Atlas antibody, HPA040902) in a tissue microarray containing triplicate tumor samples from 153 patients with Dukes C colorectal cancer were quantified blinded from the clinical patient data. The histogram shows the average intensity (±SEM) of MYO5B immunostaining in tumors that are well (grade 1, G1), moderately (grade 2, G2) and poorly (grade 3, G3) differentiated. *p<0.05; ***p<0.001 by Student's t-test.

2.5 Effects of MYO5B in the migration and invasion capacity of colon cancer cells.

In the tumorigenic evolution of a cancer, the reorganization and reassembly of the actin cytoskeleton is a key step for invasive cell behavior, such as the dissolution of cell–cell contacts and motility [242]. The migration capacity of our isogenic models after the reintroduction of MYO5B was studied using a wound-healing assay. RKO cells did not show differences on their motility after MYO5B overexpression (**Figure 40A**). Consistent with previous reports, SW837 cells showed limited motility under these conditions [239]. However, when a boyden chamber assay was used to assess migration a significant reduction was observed after reintroduction of MYO5B (**Figure 40B**). Knockdown of MYO5B in SKCO1 cell line did not affect the motility of the cells measured by wound-healing assay (**Figure 40C**).

In addition, the invasive capacity of the two MYO5B overexpressing cell lines was studied using a matrigel transwell invasion assay (**Figure 40D-E**). RKO cell line showed decreased invasion after reintroduction of MYO5B compared to the non-induced controls and the reduction was not significant in the case of SW837 cells (**Figure 40D**).

2.6 MYO5B protein levels associate with patient survival

We have used a tissue microarray containing triplicate tumor samples from 155 patients with Dukes C colorectal cancer to investigate possible associations between MYO5B levels and patient survival. The levels of MYO5B protein in these tumors were determined by immunohistochemistry and the specificity of the antibody used was confirmed on formalin-fixed, paraffin-embedded samples from the xenografts generated with RKO and SKCO1 cell lines, with inducible MYO5B overexpression or downregulation respectively (**Figure 41A-B**). Moreover, the specificity was also validated in intestinal samples of the MYO5B knockout model described (**Figure 22B-I**). The staining levels of each sample were scored using a semiquantitative scale from 0 (absence of MYO5B immunostaining), 1 (low immunostaining), 2 (moderate immunostaining) and 3 (high immunostaining), and were evaluated blinded from the clinical data of the patients (**Figure 41C**).

For Kaplan-Meyer plots, MYO5B levels were dichotomized as low if average immunostaining score was <0.4 and high if it was ≥ 0.4. To select this cutoff value, the survival difference in the high and low MYO5B groups for every possible cutoff value observed in this series was assessed with cutoff finder web server, and the value that maximized the survival differences was selected. A significant association was observed between MYO5B expression and disease-free (Logrank test $p<0.001$) or overall survival (Logrank test $p<0.019$) (**Figure 41D-E**). When the tumor levels of MYO5B were considered as a continuous variable by using Cox regression we confirmed the association with disease-free (Cox test $p=0.034$) and overall survival (Cox test $p=0.05$). As mentioned before, a significant association between MYO5B tumor levels and degree of tumor differentiation (grade) was found (Fisher test $p<0.0001$, **Table 5**). No correlation with other clinicopathological features of Dukes C colorectal cancer patients was observed (**Table 5**).

Finally, to validate MYO5B tumor levels as an independent prognostic marker in colorectal cancer we selected only the patients with grade 2 tumor differentiation. MYO5B tumor expression levels were dichotomized as previously explained and Kaplan-Meyer curves were plotted. A significant association between MYO5B levels and disease-free survival was observed (cutoff value 0.4; Logrank test p=0.02; **Figure 41F**). The association between MYO5B levels and overall survival of the patients was not found significant (cutoff 0.4; Logrank test p=0.43; **Figure 41G**).

Table 5. Clinicopathological features of Dukes C patients.

	Total	High MYO5B	Low MYO5B	p value
Sex, n (%)				
Female	76	63 (48.5)	13 (52)	0.83[1]
Male	79	67 (51.5)	12 (48)	
Age (years), mean±SD	65.3	64.9+/-12.9	67.6+/-11.9	0.47[2]
Site, n (%)				
Colon	94	76 (59)	18 (72)	0.23[1]
Rectum	60	53 (41)	7 (28)	
Degree of differentiation, n (%)				
Good	20	20 (15.7)	0 (0)	<0.0001[1]
Moderate	113	99 (77.9)	14 (56)	
Poor	19	8 (6.3)	11 (44)	
Mean follow up (years), mean±SD	9.2	9.2+/-1.1	9.4+/-1.2	0.42[3]
Alive	65	59 (45.4)	6 (24)	0.05
Dead	90	71 (54.6)	19 (76)	
Adjuvant treatment, n (%)				
Yes	73	59 (47.6)	14 (58.3)	0.38[1]
No	75	65 (52.4)	10 (41.7)	
Microsatellite instability, n (%)				
MSI	20	16 (12.4)	4 (16)	0.74[1]
MSS	134	113 (87.6)	21 (84)	
TP53 status, n (%)				
Wild type	18	17 (48.6)	1 (25)	0.6[1]
Mutant	21	18 (51.4)	3 (75)	
KRAS status				
Wild type	33	30 (65.3)	3 (60)	1[1]
Mutant	18	16 (34.7)	2 (40)	
Allelic loss of chromosome 18q, n (%)				
LOH	43	36 (41)	7 (50)	0.57[1]
No LOH	59	52 (59)	7 (50)	

[1] Fisher test; [2] Mann Whitney test; [3] Student's T-test.

Figure 41. Survival of colorectal cancer patients with high and low MYO5B levels in their tumors. (A-B) The specificity of the antibody (Atlas antibody, HPA040902) was validated staining formalin-fixed, paraffin-embedded tumors from xenografts generated with RKO derivate cell line overexpressing MYO5B **A)** and SKCO1 with stable MYO5B knockdown **B). (C)** The levels of MYO5B protein were assessed by MYO5B immunohistochemistry in a cohort of 155 Dukes C colorectal tumor samples. A representative image is shown **(D-E)** Kaplan-Meier plots showing the disease-free **D)** and overall survival **E)** of 155 Dukes C colorectal cancer patients as a function of tumor MYO5B levels. **(F-G)** Kaplan-Meier plots of patients with low grade tumors showing the disease-free **F)** and overall survival **G)** as function of tumor MYO5B levels for patients with low grade tumors. P values are from the Logrank test. N indicates the number of patients.

To further study the role of MYO5B in the progression of colon cancer, we have used immunohistochemical staining of MYO5B on sections from a tissue microarray (TMA) containing normal tissues, adenomas, primary tumors and regional lymph node samples from a cohort of 89 Dukes C colorectal cancer patients, and found that the levels of MYO5B are significantly reduced in the tumors compared to normal tissues (**Figure 42**). Moreover, regional lymph node metastasis also showed a significant reduction in the MYO5B staining compared to the primary tumor (**Figure 42**).

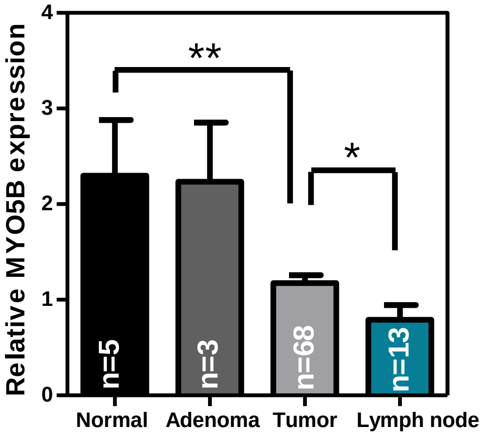

Figure 42. MYO5B expression levels are reduced in local metastasis compared to the primary colorectal tumors. Average intensity of the MYO5B immunostaining (±SEM) in the normal mucosa, adenoma, primary tumors and lymph node metastases in a cohort of 89 Dukes C colorectal cancer cases. N represents number of patients per group. *p<0.05; **p<0.01 by Student's t-test.

DISCUSSION

Myosin VB is a molecular motor protein that uses the energy of ATP hydrolysis to move along actin filaments transporting different cargoes. This protein is abundant in epithelial cells, mainly from the small and large intestine, where it participates in recycling endosome trafficking to the plasma membrane [145]. This function is accomplished through the interaction with the small GTPases RAB11A, RAB25, RAB11-family interacting protein (RAB11A-FIP2) and RAB8A [148–150] . The relationship between MYO5B and the establishment of polarization in epithelial cells is also well known [101,151]. This process has been shown to be orchestrated from RAR8A/RAB11A-positive subapical vesicles that constitute a signaling platform for different proteins controlling the process: i.e., Par3/6-aPKC-Cdc42 polarity complex, related to Madin-Darby canine kidney (MDCK) cell polarization and cyst formation [166,169] or aPKC, AKT2, LOK, SLK and MST4 kinases, which participate in Ezrin phosphorylation and brush border formation in enterocytes [102,243]. During the polarization process, MYO5B is recruited by RAB8A and RAB11A to the vesicle and constitutes the motor for their transport and localization to the subapical region of the cell. MYO5B provides spatial control of the process, being directly implicated in the polarization mechanism.

1. Generation and validation of a MYO5B knockout murine model.

In the present study, we have developed and characterized the first animal model with targeted inactivation of *Myo5b* (data published in Scientific Reports [244], attached in Annex). The animal model was designed based on the "knockout first strategy" [219], a versatile design that generates an initial null allele (tm1a) with conditional potential after Flp recombination of the trapping cassette (tm1c; **Figure 22A**). Further cross of the conditional *Myo5b*^{tm1c} allele with *Vil-CRE*^{ERT2} mice allowed us to get a tamoxifen-inducible intestinal-epithelium specific knockout model. Both *Myo5b*$^{tm1a(KOMP)Wtsi/tm1a(KOMP)Wtsi}$ and tamoxifen-induced *Vil-Cre*^{ERT2};

Myo5b$^{tm1c/tm1c}$ showed absent Myo5b staining in the epithelial cells of the small and large intestine, validating the model. Apart of the complex crossing strategy that was designed and followed, it is important to mention the complicated genotyping needed at every step. In addition to the set of primers provided by the KOMP consortium, design of new pairs that allowed confirmation of the genotypes was also needed in some cases. Moreover, Flp recombination did not function as expected in a first attempt since the *Myo5b*$^{tm1c/tm1c}$ obtained did not show a wild type reverted phenotype and died soon after birth, similarly to homozygous *Myo5b*$^{tma1(KOMP)Wtsi}$ mice. DNA sequencing of exon 5 confirmed Flp recombination but it is probable that an error during the process could have affected a key sequence flanking *Myo5b* exon 5, impairing subsequent mRNA splicing. For this reason, only data of the constitutive tm1a mice was reported in the Scientific Reports publication. A second cross with Flp deleter mice was needed to get a correct tm1c wild type reverted allele. Due to the delay caused by this problem, the role of Myo5b in colorectal cancer could not be fully studied *in vivo* to be included in this thesis.

2. Characterization of MYO5B knockout mice as the first MVID animal model.

The role of myosin VB protein in polarization is demonstrated in microvillus inclusion disease (MVID), a congenital autosomal recessive syndrome characterized by life-threatening watery diarrhea [181,182]. Germline mutations in *MYO5B* are associated with the majority of the cases of MVID [161,185,186] (www.MVID-central.org). The lack of animal models has hampered a better knowledge of the molecular pathogenesis of the disease and most of the research during the last decade has been done using intestinal biopsies and *in vitro* models. Thus, we have characterized a mouse model with targeted *Myo5b* inactivation as the first model for MVID. First, studying our constitutive *Myo5b* knockout mice we have observed all the typical features detected in patients with early onset MVID, the most common form of this disease accounting for >80% of the cases [183]. *Myo5b* deficient mice showed no overt defects during embryonic development, having normal size and weight. However, newborn *Myo5b* knockout mice showed watery diarrhea and died during the first 12 h of life, likely due to dehydration and/or reduced nutrient availability secondary to absorption defects, as exemplified by the low blood glucose levels observed, although the contribution of each of these symptoms to the death of Myo5b deficient mice cannot be conclusively determined. The body weight reduction observed in *Myo5b* knockout mice (8% in approximately 6 h) is consistent with the fluid loss reported in early onset MVID patients [182]. In previous studies, the perinatal mortality of *Klf4* or *Scd2* newborn knockout mice was attributed to a 5–10% reduction of body weight due to transepidermal water loss [245,246]. In humans, this rapid rate of dehydration would result in hypovolemic shock leading to death, as observed in *Myo5b* knockout mice. On the other hand, newborn mice have previously been shown to go through a transitory phase of severe hypoglycemia (about 10 mg/dL within 2 h of birth) until glucose levels are restored due to gluconeogenesis and eventually nutrient absorption of maternal milk [247–249]. Consistent with the phenotype observed in *Myo5b* knockout animals, the incapacity of newborn mice to overcome the postnatal hypoglycemia has been shown to be fatal within 18 h [248]. A recent study has shown that apical fructose-transporter (GLUT5) is localized via RAB11A/RAB8A and MYO5B towards the vicinity of the apical plasma membrane of enterocytes [250]. Furthermore, in MVID patients, sodium glucose transporter 1 (SGLT1) is lost, as shown by immunostaining [191]. Thus, the hypoglycemia found in the newborns likely reflects intestinal malabsorption related with defects in the intestinal transport of monosaccharides. In addition, although no reproducible defects have been reported in other organs of MVID patients and no histological abnormalities were observed in the *Myo5b* knockout mice, additional studies of the function of other organs and the possible contribution to the death of Myo5b deficient mice are warranted. Similarly to Myo5b knockout newborns, intestinal-epithelium specific $Vil\text{-}Cre^{ERT2}$; $Myo5b^{tm1c/tm1c}$ adult mice developed severe diarrhea after tamoxifen injection that originated an average weight loss of 17.9 % in five days. The animals showed clear signs of dehydration at the moment of being sacrificed. All these result are also consistent with the clinical observations in early onset MVID patients [182].

At the histological level, the villous atrophy observed in MVID patients was also detected in our epithelium-intestinal specific knockout mice that showed reduced villi. This feature was not found in our E20 embryos or newborns, suggesting that this phenotype is secondary to environmental cues. For example a prolonged absence of nutrients in the gastrointestinal tract has been associated with varying levels of villous atrophy [251,252]. Moreover, crypt hyperplasia was observed in both E20 knockout embryos and epithelium-intestinal specific knockout adult mice. More recently, two other MVID models have been published. Scheneeberger *et al.* reported an intestine-specific conditional *Myo5b* deficient mice targeting exon 4, whereas Weis *et al.* presented a "knockout first" approach for germline, constitutively inestinal targeted and inducible intestinal targeted deletion of *Myo5b*. Comparably to ours, both animal models showed severe diarrhea and weight loss. Moreover, villous atrophy and crypt hyperplasia was also observed.

At the ultrastructural level, all the defects detected in the intestinal epithelium of MVID patients [180,181] were also observed in the enterocytes of *Myo5b* knockout newborn mice including the characteristic subapical accumulation of periodic acid-Schiff (PAS) granules, microvillus atrophy and microvillus inclusion bodies. Other apical and basolateral protein markers, such as alkaline phosphatase, ezrin and transferrin receptor (TfR) were also observed mislocalized, in good agreement with what has been also reported in the other two MVID mice models [253,254]. Collectively, this study provides the first formal demonstration of the inactivation of *Myo5b* as the cause of microvillus inclusion disease. Moreover, these results indicate that the absence of a functional myosin VB protein, rather than the presence of pathogenic myosin VB mutations [191], is responsible for the intestinal defects observed in MVID patients. In addition, the presence of ultrastructural defects in the enterocytes of Myo5b-deficient E20 embryos indicates that this phenotype is tissue-autonomous and does not depend on environmental cues.

The *Myo5b* knockout model described here closely phenocopies human early-onset microvillus inclusion disease and will be instrumental for the characterization of the molecular mechanisms downstream of myosin VB responsible for the phenotype observed in the patients. Moreover, it constitutes an ideal system to preclinically test the efficiency of possible new therapeutic approaches for these patients, including pharmacological or gene therapy using for example autologous reimplantation of intestinal epithelium grown *ex vivo* following restoration of functional myosin VB [255].

3. MYO5B regulates polarization and differentiation of colon cancer cells.

Epithelial cells exhibit asymmetric distribution of protein, lipid and RNA macromolecules, a property called cell polarity, which organizes the plasma membrane into apical and basal compartments [256]. Loss of apical–basal polarity is an early event in epithelial cancers and can occur at preinvasive stages. When polarity is disrupted, cells may become unresponsive to growth inhibitory signals and may circumvent differentiation, senescence or apoptosis [257,258]. Interestingly, several proteins that regulate apical-basolateral polarity such as Crumb protein complex (CRB-PALS1-PATJ), Par3/6-aPKC-Cdc42 polarity complex, Scrib complex (SCRIB-LGL-DLG) and liver kinase B1 (LKB1) include well known tumor suppressors and proto-oncoproteins and also exhibit crosstalk with signalling pathways that control cell growth and proliferation, including WNT, MAPK and mTOR signaling [256–260]. For example, mutations in LKB1, a master regulator of brush border formation [102,225], causes Peutz-Jeghers syndrome, in which patients develop gastrointestinal polyps and are predisposed to cancer in multiple tissues, including the colon [261,262]. The correct localization of proteins on the apical and basolateral surfaces is dependent on an intracellular network of vesicles that move along microtubule and F-actin filamentous highways [218,256]. Alterations in these fundamental pathways can also lead to losses in cellular polarity during the earliest stages of carcinogenesis [258,259]. Vesicular trafficking is mainly regulated by two classes of proteins, namely syntaxins

(STX, members of the SNARE family of proteins) and RAB small GTPases [218,257,263]. Indeed, loss of STX3 causes a variant of MVID [187] and RAB8A and RAB11A deficient mice also display MVID-like phenotypes, highlighting the role of vesicle trafficking in cell polarity [171,193]. Furthermore, RAB25 promotes intestinal neoplasia in mice and is associated with human colon adenocarcinoma [213,214]. Additionally, vesicle movement can be also influenced by other small GTPases such as RAC, CDC42 and RHO, which modify the structure of cytoskeletal elements, or molecular motor proteins including unconventional myosins. The work presented in this thesis demonstrates that unconventional myosins are not only passive players on this complex mechanism and can constitute a direct link to the early stages of carcinogenesis. Indeed, previous data in our laboratory have demonstrated the tumor suppressor role of the brush border unconventional myosin IA in colon carcinogenesis, whose inactivation also leads to a decrease differentiation and loss of polarity [217]. Interestingly, myosin IA is mislocalized in human MVID intestine and in a model of MYO5B depleted Caco2-BBE cells [264]. Moreover, total MYO1A protein levels, which normally increase during the differentiation process [217], are reduced upon deletion of *MYO5B* in Caco2-BBE cells, in agreement with previous reports [264].

As explained above, LKB1 kinase is a key regulator of brush border formation and has tumor suppressor activity in the intestine [261,262] which likely depends on its role in polarity regulation [265]. However, LKB1 mutations are rare in sporadic colorectal tumors and epigenetic inactivation is not frequently observed [266,267] suggesting that alternative mechanisms exist in intestinal tumor cells to disrupt epithelial cell polarity and differentiation during the earlier stages of the tumorigenic process. As demonstrated in LS174T-W4 colon cancer cells with inducible LKB1 [225], MYO5B loss impairs polarization probably by affecting subcellular localization of key mediators of this process downstream of LKB1, such as MST4 and atypical kinase C iota (aPKC-i) [102,191]. Interestingly, active aPKC-i is increased five fold in a model of MYO5B knockdown in Caco2-BBE cells [268], and elevated constitutive activity of aPKC-i promotes colon, lung, liver, breast, pancreas, ovarian and prostate carcinogenesis and correlates with poor patient prognosis [269–271]. Other studies have also related aPKC-i mislocalization from the apical membrane with poor prognosis in ovarian cancer patients [272] or the pathological type of breast tumors [273]. Polarity of differentiated Caco2-BBE cells was also defective as shown by a decrease number of domes and the presence of microvillus inclusions in the MYO5B knockout cells. As explained before, domes are the result of vectorial electrolyte transport that in enterocytes is carried out by Na^+/H^+ exchanger 3 (NHE3) and the $Cl^-/HCO3^-$ exchanger downregulated in adenoma (DRA), among others. Both trasnporters have been shown to be downregulated and mislocalized in Caco2-BBE cells with stable MYO5B knockdown as well as in MVID samples [250,264], which could explain the impaired dome formation of our knockout cells. The presence of microvillus inclusions and reduced brush border revealed by F-actin staining has been also shown is other models of MYO5B downregulation in Caco2 cells [185,191,264].

The activity of brush border enzymes is also a good marker to assess the polarity/differentiation of colon cancer cells. Our results demonstrate that loss of MYO5B significantly affects alkaline phosphatase (ALP) and sucrose isomaltase (SI) activity in Caco2-BBE cells. Dipeptidyl peptidase IV (DPPIV) activity is also reduced in fully differentiated knockout cells, although no significant differences are found probably due to the high variability of the measurements. All these three markers have been shown to be mislocalized in MVID and MYO5B knockdown Caco2 cells, which could explain the reduced protein activity found here [171,191,193,244,274–276]. Moreover, DPPIV total protein levels are reduced after MYO5B depletion as shown by Dhekne *et al.* [102] and Knowles *et al.* [191], similarly to our findings for sucrase isomaltase. Kravtsov and colleagues [264] have demonstrated that DRA and NH3 expression are reduced at the mRNA level in MYO5B knockdown Caco2-BBE cells, suggesting a role of MYO5B controlling their expression. A similar mechanism could explain the reduction in SI expression. On the other hand, other studies showed that DPPIV partially localizes to the lysosomal compartment after MYO5B loss, indicating a possible shunting to the lysosomes for degradation as a consequence of an impaired apical recycling [191,274]. These results are controversial and new data is needed to further elucidate the role of MYO5B on gene expression regulation, probably by studying SI expression at the mRNA level. The reintroduction of MYO5B in RKO and SW837 cell lines only showed a slight increase in the ALP activity of SW837-MYO5B, which is not reproduced in SW837-SP-MYO5B. RKO is a very undifferentiated colon cancer cell line as reflected in the relative ALP activity detected (~1.5) that was only half of that observed for SW837 or Caco2-BBE cells (~3). The reintroduction of MYO5B in these cell lines is probably not enough to robustly induce a cell differentiation program and additional factors are also needed. Flow cytometry analysis revealed a bimodal distribution of the cells overexpressing mCherry-MYO5B transgene that was reproducible for both RKO and SW837. However, this pattern was not detected for EV controls. Taking into account that this finding could be of biological significance, both populations were sorted and used as independent cell lines (MYO and SP-MYO5B) for both RKO and SW837. However, no major changes between them were detected for any of the phenotypes studied.

On the other hand, the histone deacetylase inhibitor sodium butyrate was used to induce differentiation on SKCO1 cells, although not significant changes were observed after MYO5B depletion. This short-fatty acid has been shown to constitute a potent inductor of ALP activity, with an increase that can reach >40 fold compared to control SKCO1 cells after 120 h of treatment [241]. It is possible that MYO5B knockdown effect in these cells is not sufficient to interfere with the strong differentiation effects of sodium butyrate. Moreover, some studies have pointed out that the mechanism of butyrate-induced differentiation versus spontaneous differentiation in colon adenocarcinoma cells is different. In fact, butyrate exposure originates apoptosis in colon cancer cells which is rarely observe during spontaneous differentiation [277–279]. The approach used is likely not suitable for our purpose and the assay will need to be perform after spontaneous differentiation of SKCO1 cells to confirm the result.

Collectively, our results indicate a role of MYO5B in the differentiation of colon cancer cells which is in good agreement with previous observations.

In addition, we have also found that MYO5B protein levels highly correlate with the differentiation grade of primary colorectal tumors, a well-known stage-independent prognostic factor in cancer [53].

4. MYO5B loss causes intestinal crypt hyperplasia, a precancerous stage.

The establishment and maintenance of apical-basal polarity in the context of the proliferative tissue is a key feature of intestinal epithelium morphogenesis. To maintain proper tissue organization, epithelial cells divide within the plane of the epithelium (known as planar polarity). Disruption of this process lead to misorienting cell divisions and multilayering [280]. Importantly, mitotic defects may lead to the generation of genome instability and could eventually contribute to the early cancer stages [256,281]. *Myo5b* inactivation in mice causes hyperproliferation in the intestine, which constitutes an example of the relationship between loss of polarity and defects in cell division. Interestingly, a similar phenotype is observed in Cdc42 deficient mice [282] which also developed gross hyperplasia, crypt enlargement and microvilli inclusions. The authors suggest that defective regulation of epithelium polarity and/or the dynamics of adherens junctions, controlled by Cdc42, serve as an early event that affects the proliferative capability and migration of intestine epithelial cells. As demonstrated by Bryant *et al*. [166] , Par3/6-aPKC-Cdc42 complex drives epithelial cell polarization and associates with both RAB8A and RAB11A which control CDC42 apical activation by recruiting its GEF Tuba. RAB8A and RAB11A are able to recruit MYO5B motor protein which directs the apical localization of the vesicles containing this protein complex and constitutes a link between the polarization machinery and vesicle transport [166,197,283]. In fact, Cdc42, Par6 and aPKC polarity proteins were found mislocalized and accumulated in the cytoplasm or the basal pole of enterocytes in patients with MVID [102,191,194], as well as in a 3D grown MYO5B depleted Caco2 cells [194]. Total CDC42 as well as active CDC42 were also reduced in a similar model of MYO5B downregulation in Caco2 cells [191].

Therefore, the loss of MYO5B could result in reduced CDC42 activity and mislocalization and could explain the similar phenotypes observed in both knockout mouse models, including the hyperplasia of the normal intestine. The relationship between the CDC42 small GTPase and cancer has also been studied but its role is not yet clear. Warner *et al* indicated that loss of Par3/6-aPKC-Cdc42 polarity complex organization or localization in the presence of inhibited apoptosis could contribute to epithelial cells hyperproliferation, which parallels early tumor development [284]. In contrast, other study showed that early-stage intestinal cells with single *APC* or *CTNNB1* mutations activate CDC42 to facilitate tumor cell survivability and microadenoma formation [285].

Intestinal stem cells are the only intestinal cells undergoing asymmetric division into a new stem cell plus a committed daughter cells. The daughter cells are rapidly cycling cells, also called transit amplifying cells, that undergo a limited number of cell divisions before terminally differentiate [25]. Most if not all of the polarity regulators within the Par3/6-aPKC-Cdc42 or its downstream effectors participate in spindle orientation during cell division and participate in the correct positioning of the apical surface [168,286]. This process seems to be of crucial importance during intestinal stem cell division as observed in Cdc42 deficient mice which showed an increase proliferating stem and progenitor cells [282]. In a similar mouse model, both Cdc42 and Rab8a have been also shown to be critical for intestinal stem cell division, survival and differentiation into Paneth cells, and the authors suggest that defects on the stem cell niche can cause MVID [283]. In addition, Rab8a controls the anterograde transport and secretion of Wnt containing vesicles in Wnt producing cells, as demonstrated in a Rab8a knockout mice model [287]. Wnt ligand is crucial for Paneth cell maturation. Furthermore, Rab8a knockout crypts also showed an expansion on Lgr5+ cells [170,197]. An early maturation of crypt Paneth cells have been reported in the Myo5b knockout mice model developed by Weis *et al*. [253]. Paneth cells constitute the niche of the proliferative intestinal stem cell population [28], however, no alteration on intestinal stem cells have been reported in a Myo5b deficient mice model so far. The analysis of the stem cell population in Myo5b deficient mice would be of great interest since many studies suggest that the stem cells can constitute the cell of origin for a range of solid tumors, including colorectal cancer [288]. Importantly, there are evidences indicating that spindle orientation in gut epithelial stem cells is lost in precancerous cells and could contribute to the oncogenic effect of adenomatous polyposis coly (*APC*) mutations in the intestinal epithelium [281,289].

We have studied the clonogenicity and proliferation rate of our isogenic and knockout models both *in vitro* and *in vivo*, observing that MYO5B does not play a significant role in these processes. Importantly, all the cell lines employed are derived from human colon or rectum primary adenocarcinomas and metastasis and represent a model of highly advance disease. All of them bear mutations in important tumor suppressor genes and/or oncogenes, such as *APC*, *TP53* or *KRAS* which drive their high proliferation rates and anchorage-independent growth. In contrast, our *Myo5b* knockout mice demonstrates that Myo5b inactivation causes hyperplasia of the the normal intestine, which would represent a precancerous stage that is not faithfully modeled by the *in vitro* models. Therefore, these data confirm a role of MYO5B in the precancerous stage, originating hyperplasia of the normal intestine.

5. MYO5B is involved is the migration and invasion capacity of colon cancer cells

The loss of differentiation and epithelial architecture is a hallmark of advanced solid tumors and is related to poor patient prognosis [233,290]. This process is represented by the epithelial to mesenchymal transition (EMT) where the cells loss their intercellular adhesions and polarity, acquiring a mesenchymal phenotype with increased motility and invasion capacity. At the molecular level, this complex process is characterized by the increased expression of mesenchymal markers like N-cadherin, Vimentin and SNAIL1, SNAIL2 (SLUG), TWIST, ZEB1 and ZEB2 transcription factors, that downregulate cell-cell adhesion molecules such as E-cadherin. During tumor progression, undifferentiated cells that underwent EMT are able to infiltrate the surrounding tissues and ultimately metastasize to distant sites [233,291].

Interestingly, an impaired vesicle trafficking probably mediates many aspects of cell invasion and metastasis. For example, losses in cell polarity can lead to inappropriate delivery of degradative metalloproteinases to the cell surface, promoting cell invasion and transformation [292]. In addition, defective trafficking may cause the redistribution of cell adhesion molecules, such as integrins, within cells leading to proliferative and motility responses [293]. Altered delivery of junctional components could also elicit changes in the permeability of the mucosa and exposure of the basolateral surface to the luminal factors, immune cells and inflammatory cytokines. For example, the loss of RAB25 in Caco2 cells leads to an aberrant surface presentation and decrease expression of β1 and α5-integrin as well as changes in both adherens and tight junctions which finally promoted the motility of the cells [294,295]. No changes in the motility of SKCO1 cells with stable MYO5B knockdown or RKO cell after MYO5B reintroduction were observed. Individual losses in structural cell polarity components do not generally lead to carcinogenesis and need the combination with other secondary perturbations. Thus, the loss of either β1-integrin or RAB25 does not by itself lead to cancer but the combination with other perturbations can reveal tumor suppressor functions [213,296]. This fact could explain the unaffected motility of SKCO1 cells after MYO5B downregulation. Moreover, it could be also possible that the factors or pathways controlling motility are already affected in this specific cell lines and the loss of MYO5B does not add any change to this phenotype. On the other hand, the reintroduction of MYO5B in SW837.cells significantly reduced their motility but no changes in the invasion capacity of these cells were found. In contrast, RKO cell line showed a reduced invasion capacity after MYO5B reintroduction. As previously explained, the correct delivery of metalloproteinases to the cell surface is of importance during cell invasion. According to our findings, it is possible that MYO5B has also a role controlling this pathway. In addition, these results are in agreement with previous observations in gastric cancer that have related MYO5B inactivation with an increased motility and invasion on gastric cancer cells [211]. Interestingly, the inactivation of RAB11A-FIP2 is also related to gastric cancer cells invasion, indicating that impaired apical recycling endosomes trafficking could be important for this mechanism [212]. In addition, both studies also showed reduced MYO5B and RAB11A-FIP2 proteins in gastric lymph node metastasis. The results presented here also demonstrate a reduction in the levels of MYO5B in the intestinal lymph node metastasis compared to the primary tumors, further indicating that MYO5B is involved in the progression of colorectal tumors.

6. MYO5B is an independent marker of prognosis in colorectal cancer patients.

Identification of prognostic factors is a prerequisite for uniformed decisions regarding the treatment and predicting the outcome of patients with colorectal cancer. The pathologic stage, defined by the tumor-node-metastasis (TNM) or the Dukes's systems (see **Table 1**) represents the most important prognostic factor. This system is based on the degree of penetration of the tumor through the intestinal wall and the presence of metastasis in regional lymph nodes or distant organs. Nevertheless, patients diagnosed with histopathologically indistinguishable tumors of the same stage can widely vary in their disease recurrence and survival. Several protein and genetic markers have been described in an attempt to refine prognostic information and predict the benefit derived from systemic treatment. This could help to avoid the toxicities associated with systemic therapy in those patients who will not benefit from this treatment. Microsatellite instability and loss of heterozygosity at chromosome 18q are the two best-defined molecular prognostic markers [297]. *TP53, KRAS* and *BRAF* mutations as well as SMAD4 expression levels have been also identified as prognostic markers in colorectal cancer [298–300]. However, even for more widely studied markers, there is often little consensus about their true clinical value: the prognostic effect of molecular markers described many years ago, is only now entering prospective clinical trials [58,299]. In this scenario, the need for additional colorectal cancer biomarkers that would allow better stratification of patients with different prognosis is warrantied.

A new biomarker for predicting outcome should fulfill different criteria: provide stronger prognostic information than the offered by existing staging systems; provide information independent of the existing systems; provide prognostic data within specific subgroups defined by existing criteria, i.e., within a Dukes' stage. Recently, unconventional myosin 1A tumor levels have been reported as a novel prognostic marker for colorectal cancer [217]. In this thesis, the prognosis predictive value of MYO5B was tested in patients diagnosed with locally advanced Dukes' C colorectal cancer and the levels of MYO5B were found to be significantly associated with both disease-free ($p<0.001$) and overall survival ($p=0.019$) of the patients. Importantly, MYO5B levels are also predictive of the disease-free survival in grade 2 patients ($p=0.02$), indicating that the prognostic value is both grade and stage-independent. If confirmed in larger and independent patient cohorts, these data indicates that MYO5B levels could be used in the clinic as a novel biomarker with important implications for patient management. MYO5B levels assessed by immunostaining could predict the probability of recurrence after surgery and significantly contribute to the stratification of patients to assess the real need for adjuvant chemotherapy.

CONCLUSIONS

Myosin VB motor protein is involve in apical endosomes recycling and contribute to epithelial cells polarization. Mutations in *MYO5B* have been shown to be the cause of Microvillus inclusion disease. However, the molecular pathology of this congenital diarrheal disorder is not well known, mainly due to the lack of animal models. Additionally, imbalances in dynamic vesicle trafficking processes and loss of polarization/differentiation also have important roles in cancer during tumor initiation and cell invasion. Myosin VB inactivation has been reported to regulate the motility and invasion of gastric cancer cells but its role in colorectal cancer has not been investigated before. In this study we report the first mouse model with constitutive and intestinal-epithelium specific inactivation of *Myo5b*. Moreover, the functional relevance of the loss of MYO5B in colorectal cancer was investigated. Concluding, the main findings of this study are as follows:

- Constitutive or intestinal-epithelium specific inactivation of Myo5b in mice recapitulates the phenotype observed in early-onset Microvillus inclusion disease patients and constitutes the first mouse model of the disease and formal demonstration of MYO5B inactivation as the cause of MVID.
- Inactivation of myosin VB in the intestinal epithelium of mice leads to crypt hyperplasia, suggesting a role of MYO5B in the precancerous stage of colorectal cancer.
- Inactivation of myosin VB impairs polarization and differentiation of colon cancer cells.
- Inactivation of myosin VB does not affect the survival, anchorage-independent growth or proliferation of colon cancer cells, but results in increased motility and invasion.
- Low MYO5B tumor levels are associated with shorter disease-free and overall survival of patients with locally advanced colorectal cancer.

This study contributes to better understand the pathogenesis of Microvillus inclusion disease. In addition, these results indicate a possible role of MYO5B in the initiation and progression of colorectal cancer.

BIBLIOGRAPHY

1. Moore, K. & Dalley, A. *Clinically oriented anatomy*. (2006).
2. Helander, H. F. & Fändriks, L. Surface area of the digestive tract - revisited. *Scand. J. Gastroenterol.* **49,** 681–9 (2014).
3. Standring. *Gray's anatomy: The Anatomical Basis of Clinical Practice*. (2009).
4. Young, B., Lowe, J. S., Stevens, A. & Health, J. W. *Wheather's Functional Histology*. (2006).
5. Deplancke, B. & Gaskins, H. R. Microbial modulation of innate defense: goblet cells and the intestinal mucus layer. *Am. J. Clin. Nutr.* **73,** 1131S–1141S (2001).
6. Kim, J. & Khan, W. Goblet Cells and Mucins: Role in Innate Defense in Enteric Infections. *Pathogens* **2,** 55–70 (2013).
7. Gunawardene, A. R., Corfe, B. M. & Staton, C. A. Classification and functions of enteroendocrine cells of the lower gastrointestinal tract. *Int. J. Exp. Pathol.* **92,** 219–31 (2011).
8. Clevers, H. The Intestinal Crypt, A Prototype Stem Cell Compartment. *Cell* **154,** 274–284 (2013).
9. Clevers, H. & Batlle, E. SnapShot: The Intestinal Crypt. *Cell* **152,** 1198–1198.e2 (2013).
10. Bastide, P. Sox9 regulates cell proliferation and is required for Paneth cell differentiation in the intestinal epithelium. *J. Cell Biol.* **178,** 635–48 (2007).
11. Sobotta, J. *Sobotta. Human anatomy atlas*. (2012).
12. Massey-Harroche, D. Epithelial cell polarity as reflected in enterocytes. *Microsc. Res. Tech.* **49,** 353–362 (2000).
13. Crawley, S. W., Mooseker, M. S. & Tyska, M. J. Shaping the intestinal brush border. *J. Cell Biol.* **207,** 441–451 (2014).
14. Delacour, D., Salomon, J., Robine, S. & Louvard, D. Plasticity of the brush border - the yin and yang of intestinal homeostasis. *Nat. Rev. Gastroenterol. Hepatol.* **13,** 161–74 (2016).
15. Hartsock, A. & Nelson, W. J. Adherens and tight junctions: structure,

function and connections to the actin cytoskeleton. *Biochim. Biophys. Acta* **1778,** 660–9 (2008).

16. Mittal, R. & Coopersmith, C. M. Redefining the gut as the motor of critical illness. *Trends Mol. Med.* **20,** 214–23 (2014).

17. Crosnier, C., Stamataki, D. & Lewis, J. Organizing cell renewal in the intestine: stem cells, signals and combinatorial control. *Nat. Rev. Genet.* **7,** 349–59 (2006).

18. Heath, J. P. Epithelial cell migration in the intestine. *Cell Biol. Int.* **20,** 139–146 (1996).

19. Pinto, D. & Clevers, H. Wnt control of stem cells and differentiation in the intestinal epithelium. *Exp. Cell Res.* **306,** 357–363 (2005).

20. van der Flier, L. G. & Clevers, H. Stem cells, self-renewal, and differentiation in the intestinal epithelium. *Annu Rev Physiol* **71,** 241–260 (2009).

21. Humphries, A. & Wright, N. a. Colonic crypt organization and tumorigenesis. *Nat. Rev. Cancer* **8,** 415–24 (2008).

22. Medema JP, V. L. Microenvironmental regulation of stem cells in intestinal homeostasis and cancer. *Nature* **474,** 318–26 (2011).

23. Barker, N. *et al.* Identification of stem cells in small intestine and colon by marker gene Lgr5. *Nature* **449,** 1003–1007 (2007).

24. Sato, T. *et al.* Single Lgr5 stem cells build crypt–villus structures in vitro without a mesenchymal niche. *Nature* **459,** 262–265 (2009).

25. Umar, S. Intestinal stem cells. *Curr. Gastroenterol. Rep.* **12,** 340–8 (2010).

26. Buczacki, S. J. A. *et al.* Intestinal label-retaining cells are secretory precursors expressing Lgr5. *Nature* **495,** 65–69 (2013).

27. Pinto, D. & Clevers, H. Wnt, stem cells and cancer in the intestine. *Biol. Cell* **97,** 185–196 (2005).

28. Sato, T. *et al.* Paneth cells constitute the niche for Lgr5 stem cells in intestinal crypts. *Nature* **469,** 415–418 (2011).

29. de Lau, W. *et al.* Lgr5 homologues associate with Wnt receptors and mediate R-spondin signalling. *Nature* **476,** 293–7 (2011).

30. He, T. C. *et al.* Identification of c-MYC as a target of the APC pathway. *Science* **281,** 1509–12 (1998).

31. McCormick, F. & Tetsu, O. Beta-catenin regulates expression of cyclin D1 in colon carcinoma cells. *Nature* **398,** 422–426 (1999).

32. Wielenga, V. J. *et al.* Expression of CD44 in Apc and Tcf mutant mice implies regulation by the WNT pathway. *Am. J. Pathol.* **154,** 515–23 (1999).

33. Pino, M. S. & Chung, D. C. The Chromosomal Instability Pathway in Colon Cancer. *Gastroenterology* **138,** 2059–2072 (2010).

34. Madison, B. B. *et al.* Epithelial hedgehog signals pattern the intestinal crypt-villus axis. *Development* **132,** 279–89 (2005).

35. He, X. C. *et al.* BMP signaling inhibits intestinal stem cell self-renewal through suppression of Wnt-beta-catenin signaling. *Nat. Genet.* **36,** 1117–21 (2004).

36. Haramis, A.-P. G. *et al.* De novo crypt formation and juvenile polyposis on BMP inhibition in mouse intestine. *Science* **303,** 1684–6 (2004).

37. van der Flier, L. G. & Clevers, H. Stem Cells, Self-Renewal, and Differentiation in the Intestinal Epithelium. *Annu. Rev. Physiol.* **71,** 241–260 (2009).

38. Pellegrinet, L. *et al.* Dll1- and dll4-mediated notch signaling are required for homeostasis of intestinal stem cells. *Gastroenterology* **140,** 1230-1240–7 (2011).

39. Snippert, H. J. *et al.* Intestinal crypt homeostasis results from neutral competition between symmetrically dividing Lgr5 stem cells. *Cell* **143,** 134–144 (2010).

40. Robert A. Weinberg. *The Biology of cancer*. (2007).

41. Stewart, B. W., Wild, C. P. *World cancer report 2014*. (2014).

42. Ferlay, J. *et al.* Cancer incidence and mortality patterns in Europe: Estimates for 40 countries in 2012. *Eur. J. Cancer* **49,** 1374–1403 (2013).

43. Plummer, M. *et al.* Global burden of cancers attributable to infections in 2012: a synthetic analysis. *Lancet Glob. Heal.* **4,** e609–e616 (2016).

44. Hanahan, D. & Weinberg, R. A. The Hallmarks of Cancer. *Cell* **100,** 57–70 (2000).

45. Hanahan, D. & Weinberg, R. A. Hallmarks of cancer: The next

generation. *Cell* **144,** 646–674 (2011).

46. O. Warburg, K. Posener, E. N. Negelein: Ueber den Stoffwechsel der Tumoren. *Biochem. Z.* **152,** 319–344 (1924).

47. Haggar, F. a, Boushey, R. P. & Ph, D. Colorectal Cancer Epidemiology : Incidence , Mortality , Survival , and Risk Factors. *Clin. Colon Rectal Surg.* **6,** 191–197 (2009).

48. Cheng, L. & Lai, M.-D. Aberrant crypt foci as microscopic precursors of colorectal cancer. *World J. Gastroenterol.* **9,** 2642–9 (2003).

49. Preston, S. L. *et al.* Bottom-up histogenesis of colorectal adenomas: origin in the monocryptal adenoma and initial expansion by crypt fission. *Cancer Res.* **63,** 3819–25 (2003).

50. Shih, I.-M. *et al.* Top-down morphogenesis of colorectal tumors. *Proc. Natl. Acad. Sci.* **98,** 2640–2645 (2001).

51. McDonald, S. a C., Preston, S. L., Lovell, M. J., Wright, N. a & Jankowski, J. a Z. Mechanisms of disease: from stem cells to colorectal cancer. *Nat. Clin. Pract. Gastroenterol. Hepatol.* **3,** 267–274 (2006).

52. Schwitalla, S. *et al.* Intestinal Tumorigenesis Initiated by Dedifferentiation and Acquisition of Stem-Cell-like Properties. *Cell* **152,** 25–38 (2013).

53. Compton, C. C. Colorectal Carcinoma: Diagnostic, Prognostic, and Molecular Features. *Mod. Pathol.* **16,** 376–388 (2003).

54. Brenner, H., Kloor, M. & Pox, C. P. Colorectal cancer. *Lancet* **383,** 1490–1502 (2014).

55. Weitz, J. *et al.* Colorectal cancer. *Lancet* **365,** 153–65 (2005).

56. Fearon, E. R. & Vogelstein, B. A genetic model for colorectal tumorigenesis. *Cell* **61,** 759–67 (1990).

57. Rao, C. V & Yamada, H. Y. Genomic instability and colon carcinogenesis: from the perspective of genes. *Front. Oncol.* **3,** 130 (2013).

58. Walther, A. *et al.* Genetic prognostic and predictive markers in colorectal cancer. *Nat. Rev. Cancer* **9,** 489–499 (2009).

59. Rustgi, A. K. The genetics of hereditary colon cancer. *Genes Dev.* **21,** 2525–2538 (2007).

60. Fearon, E. R. Molecular genetics of colorectal cancer. *Annu. Rev. Pathol.* (2011). doi:10.1146/annurev-pathol-011110-130235

61. Gryfe, R. Inherited colorectal cancer syndromes. *Clin. Colon Rectal Surg.* **22,** 198–208 (2009).

62. Vilar, E. & Gruber, S. B. Microsatellite instability in colorectal cancer-the stable evidence. *Nat. Rev. Clin. Oncol.* **7,** 153–162 (2010).

63. Kuismanen, S. A., Holmberg, M. T., Salovaara, R., de la Chapelle, A. & Peltomäki, P. Genetic and epigenetic modification of MLH1 accounts for a major share of microsatellite-unstable colorectal cancers. *Am. J. Pathol.* **156,** 1773–9 (2000).

64. Markowitz, S. & Bertagnolli, M. Molecular Basis of Colorectal Cancer. *N. Engl. J. Med.* **361,** 2449–2460 (2009).

65. Pancione, M., Remo, A. & Colantuoni, V. Genetic and epigenetic events generate multiple pathways in colorectal cancer progression. *Patholog. Res. Int.* **2012,** (2012).

66. Trautmann, K. *et al.* Chromosomal Instability in Microsatellite-Unstable and Stable Colon Cancer. *Clin. Cancer Res.* **12,** 6379–6385 (2006).

67. Bettington, M. *et al.* The serrated pathway to colorectal carcinoma: current concepts and challenges. *Histopathology* **62,** 367–86 (2013).

68. Snover, D. C. Update on the serrated pathway to colorectal carcinoma. *Hum. Pathol.* **42,** 1–10 (2011).

69. Kim, M. S., Lee, J. & Sidransky, D. DNA methylation markers in colorectal cancer. *Cancer Metastasis Rev.* **29,** 181–206 (2010).

70. Issa, J.-P. Colon Cancer: It's CIN or CIMP. *Clin. Cancer Res.* **14,** 5939–5940 (2008).

71. Wood, L. D. *et al.* The Genomic Landscapes of Human Breast and Colorectal Cancers. *Science (80-.).* **318,** 1108–1113 (2007).

72. Muzny DM, Bainbridge MN, Chang K, Dinh HH, Drummond JA, Fowler G, Kovar CL, Lewis LR, Morgan MB, Newsham IF, Reid JG, Santibanez J, Shinbrot E, Trevino LR, Wu YQ, Wang M, Gunaratne P, Donehower LA, Creighton CJ, Wheeler DA, Gibbs RA, Lawrence MS, Voet D, T. E. Comprehensive molecular characterization of human colon and rectal cancer. *Nature* **487,** 330–7 (2012).

73. Goss, K. H. & Groden, J. Biology of the Adenomatous Polyposis Coli

Tumor Suppressor. *J. Clin. Oncol.* **18,** 1967–1979 (2000).

74. Korinek, V. *et al.* Constitutive transcriptional activation by a beta-catenin-Tcf complex in APC-/- colon carcinoma. *Science* **275,** 1784–7 (1997).

75. Green, R. A. & Kaplan, K. B. Chromosome instability in colorectal tumor cells is associated with defects in microtubule plus-end attachments caused by a dominant mutation in APC. *J. Cell Biol.* **163,** 949–61 (2003).

76. Giles, R. H., van Es, J. H. & Clevers, H. Caught up in a Wnt storm: Wnt signaling in cancer. *Biochim. Biophys. Acta* **1653,** 1–24 (2003).

77. Sparks, A. B., Morin, P. J., Vogelstein, B. & Kinzler, K. W. Mutational analysis of the APC/beta-catenin/Tcf pathway in colorectal cancer. *Cancer Res.* **58,** 1130–4 (1998).

78. Jin, L.-H. *et al.* Detection of point mutations of the Axin1 gene in colorectal cancers. *Int. J. cancer* **107,** 696–9 (2003).

79. Webster, M. T. *et al.* Sequence variants of the axin gene in breast, colon, and other cancers: an analysis of mutations that interfere with GSK3 binding. *Genes. Chromosomes Cancer* **28,** 443–53 (2000).

80. Liu, W. *et al.* Mutations in AXIN2 cause colorectal cancer with defective mismatch repair by activating β-catenin/TCF signalling. *Nat. Genet.* **26,** 146–147 (2000).

81. Bos, J. L. *et al.* Prevalence of ras gene mutations in human colorectal cancers. *Nature* **327,** 293–297 (1987).

82. Jass, J. R. Classification of colorectal cancer based on correlation of clinical, morphological and molecular features. *Histopathology* **50,** 113–130 (2007).

83. Markowitz, S. *et al.* Inactivation of the type II TGF-beta receptor in colon cancer cells with microsatellite instability. *Science* **268,** 1336–8 (1995).

84. Tarapore, P. & Fukasawa, K. Loss of p53 and centrosome hyperamplification. *Oncogene* **21,** 6234–6240 (2002).

85. Odronitz, F. & Kollmar, M. Drawing the tree of eukaryotic life based on the analysis of 2,269 manually annotated myosins from 328 species. *Genome Biol.* **8,** R196 (2007).

86. Hartman, M. A. & Spudich, J. A. The myosin superfamily at a glance.

J. Cell Sci. **125,** 1627–1632 (2012).

87. Krendel, M. & Mooseker, M. S. Myosins: tails (and heads) of functional diversity. *Physiology (Bethesda).* **20,** 239–51 (2005).

88. Syamaladevi, D. P., Spudich, J. A. & Sowdhamini, R. Structural and functional insights on the myosin superfamily. *Bioinform. Biol. Insights* **6,** 11–21 (2012).

89. Hartman, M. A., Finan, D., Sivaramakrishnan, S. & Spudich, J. a. Principles of unconventional myosin function and targeting. *Annu. Rev. Cell Dev. Biol.* **27,** 133–55 (2011).

90. Rodriguez, O. C. & Cheney, R. E. A new direction for myosin. *Trends Cell Biol.* **10,** 307–311 (2000).

91. Vicente-Manzanares, M., Ma, X., Adelstein, R. S. & Horwitz, A. R. Non-muscle myosin II takes centre stage in cell adhesion and migration. *Nat. Rev. Mol. Cell Biol.* **10,** 778–790 (2009).

92. Seabra, M. C. & Coudrier, E. Rab GTPases and Myosin Motors in Organelle Motility. *Traffic* **5,** 393–399 (2004).

93. Grosshans, B. L., Ortiz, D. & Novick, P. Rabs and their effectors: achieving specificity in membrane traffic. *Proc. Natl. Acad. Sci. U. S. A.* **103,** 11821–7 (2006).

94. Wu, X. *et al.* Rab27a enables myosin Va-dependent melanosome capture by recruiting the myosin to the organelle. *J. Cell Sci.* **114,** 1091–100 (2001).

95. Fukuda, M., Kuroda, T. S. & Mikoshiba, K. Slac2-a/melanophilin, the missing link between Rab27 and myosin Va: Implications of a tripartite protein complex for melanosome transport. *J. Biol. Chem.* **277,** 12432–12436 (2002).

96. Wu, X. S. *et al.* Identification of an organelle receptor for myosin-Va. *Nat. Cell Biol.* **4,** 271–278 (2002).

97. Quintero, O. A. *et al.* Human Myo19 Is a Novel Myosin that Associates with Mitochondria. *Curr. Biol.* **19,** 2008–2013 (2009).

98. Naccache, S. N., Hasson, T. & Horowitz, A. Binding of internalized receptors to the PDZ domain of GIPC synectin recruits myosin VI to endocytic vesicles. *Proc. Natl. Acad. Sci* **103,** 12735–12740 (2006).

99. Gonsalvez, G. B., Urbinati, C. R. & Long, R. M. RNA localization in yeast: moving towards a mechanism. *Biol. cell* **97,** 75–86 (2005).

100. Post, P. L., Bokoch, G. M. & Mooseker, M. S. Human myosin-IXb is a mechanochemically active motor and a GAP for rho. *J. Cell Sci.* 941–50 (1998). at <http://www.ncbi.nlm.nih.gov/pubmed/9490638>

101. Roland, J. T. *et al.* Rab GTPase-Myo5B complexes control membrane recycling and epithelial polarization. *Proc. Natl. Acad. Sci. U. S. A.* **108,** 2789–94 (2011).

102. Dhekne, Herschel S; Hsiao Nai-Hua; Roelofs Pieter, K. M. et al. Myosin Vb and rab11a regulate ezrin phosphorylation in enterocytes. *J Cell Sci* **127,** 1007–1017 (2014).

103. Puthalakath, H. *et al.* Bmf: a proapoptotic BH3-only protein regulated by interaction with the myosin V actin motor complex, activated by anoikis. *Science* **293,** 1829–32 (2001).

104. Komaba, S., Inoue, A., Maruta, S., Hosoya, H. & Ikebe, M. Determination of human myosin III as a motor protein having a protein kinase activity. *J. Biol. Chem.* **278,** 21352–60 (2003).

105. Aschenbrenner, L., Lee, T. & Hasson, T. Myo6 facilitates the translocation of endocytic vesicles from cell peripheries. *Mol. Biol. Cell* **14,** 2728–43 (2003).

106. Gumbiner, B. M. Cell adhesion: the molecular basis of tissue architecture and morphogenesis. *Cell* **84,** 345–57 (1996).

107. Bryant, D. M. & Stow, J. L. The ins and outs of E-cadherin trafficking. *Trends Cell Biol.* **14,** 427–34 (2004).

108. Millo, H., Leaper, K., Lazou, V. & Bownes, M. Myosin VI plays a role in cell-cell adhesion during epithelial morphogenesis. *Mech. Dev.* **121,** 1335–51 (2004).

109. Dippold, H. C. *et al.* GOLPH3 Bridges Phosphatidylinositol-4-Phosphate and Actomyosin to Stretch and Shape the Golgi to Promote Budding. *Cell* **139,** 337–351 (2009).

110. Yin, H., Pruyne, D., Huffaker, T. C. & Bretscher, A. Myosin V orientates the mitotic spindle in yeast. *Nature* **406,** 1013–5 (2000).

111. Provance, D. W., Wei, M., Ipe, V. & Mercer, J. A. Cultured melanocytes from dilute mutant mice exhibit dendritic morphology and altered melanosome distribution. *Proc. Natl. Acad. Sci. U. S. A.* **93,** 14554–8 (1996).

112. Tyska, M. J. & Mooseker, M. S. A role for myosin-1A in the localization of a brush border disaccharidase. *J. Cell Biol.* **165,** 395–405 (2004).

113. Pestic-Dragovich, L. *et al.* A myosin I isoform in the nucleus. *Science* **290,** 337–41 (2000).

114. Li, Q. & Sarna, S. K. Nuclear myosin II regulates the assembly of preinitiation complex for ICAM-1 gene transcription. *Gastroenterology* **137,** 1051–60, 1060–3 (2009).

115. Vreugde, S. *et al.* Nuclear myosin VI enhances RNA polymerase II-dependent transcription. *Mol. Cell* **23,** 749–55 (2006).

116. Johnston, G. C., Prendergast, J. A. & Singer, R. A. The Saccharomyces cerevisiae MYO2 gene encodes an essential myosin for vectorial transport of vesicles. *J. Cell Biol.* **113,** 539–51 (1991).

117. Reck-Peterson, S. L., Provance, D. W., Mooseker, M. S. & Mercer, J. A. Class V myosins. *Biochim. Biophys. Acta - Mol. Cell Res.* **1496,** 36–51 (2000).

118. Hirokawa, N. Kinesin and dynein superfamily proteins and the mechanism of organelle transport. *Science* **279,** 519–26 (1998).

119. Trybus, K. M. Myosin V from head to tail. *Cell. Mol. Life Sci.* **65,** 1378–1389 (2008).

120. Sellers, J. R. & Veigel, C. Walking with myosin V. *Curr. Opin. Cell Biol.* **18,** 68–73 (2006).

121. Fukuda, M. & Itoh, T. Slac2-a/melanophilin contains multiple PEST-like sequences that are highly sensitive to proteolysis. *J. Biol. Chem.* **279,** 22314–21 (2004).

122. Au, J. S.-Y. & Huang, J.-D. A tissue-specific exon of myosin Va is responsible for selective cargo binding in melanocytes. *Cell Motil. Cytoskeleton* **53,** 89–102 (2002).

123. Roland, J. T., Lapierre, L. a & Goldenring, J. R. Alternative splicing in class V myosins determines association with Rab10. *J. Biol. Chem.* **284,** 1213–23 (2009).

124. Rodriguez, O. C. & Cheney, R. E. Human myosin-Vc is a novel class V myosin expressed in epithelial cells. *J. Cell Sci.* **115,** 991–1004 (2002).

125. Wang, F. *et al.* Regulated Conformation of Myosin V. *J. Biol. Chem.* **279,** 2333–2336 (2004).

126. Liu, J., Taylor, D. W., Krementsova, E. B., Trybus, K. M. & Taylor, K. A. Three-dimensional structure of the myosin V inhibited state by

cryoelectron tomography. *Nature* **442,** 208–11 (2006).

127. Thirumurugan, K. *et al.* The cargo-binding domain regulates structure and activity of myosin 5. *Nature* **442,** 212–5 (2006).

128. Krementsov, D. N., Krementsova, E. B. & Trybus, K. M. Myosin V: regulation by calcium, calmodulin and the tail domain. *J. Cell Biol.* **164,** 877–886 (2004).

129. Li, X.-D., Ikebe, R. & Ikebe, M. Activation of myosin Va function by melanophilin, a specific docking partner of myosin Va. *J. Biol. Chem.* **280,** 17815–22 (2005).

130. Tang, F. *et al.* Regulated degradation of a class V myosin receptor directs movement of the yeast vacuole. *Nature* **422,** 87–92 (2003).

131. Desnos, C., Huet, S. & Darchen, F. 'Should I stay or should I go?': myosin V function in organelle trafficking. *Biol. Cell* **99,** 411–23 (2007).

132. Wagner, W., Fodor, E., Ginsburg, A. & Hammer, J. A. The binding of DYNLL2 to myosin Va requires alternatively spliced exon B and stabilizes a portion of the myosin's coiled-coil domain. *Biochemistry* **45,** 11564–77 (2006).

133. Hódi, Z. *et al.* Alternatively spliced exon B of myosin Va is essential for binding the tail-associated light chain shared by dynein. *Biochemistry* **45,** 12582–95 (2006).

134. Roland, J. T., Kenworthy, A. K., Peranen, J., Caplan, S. & Goldenring, J. R. Myosin Vb interacts with Rab8a on a tubular network containing EHD1 and EHD3. *Mol. Biol. Cell* **18,** 2828–37 (2007).

135. Strom, M., Hume, A. N., Tarafder, A. K., Barkagianni, E. & Seabra, M. C. A family of Rab27-binding proteins: Melanophilin links Rab27a and myosin Va function in melanosome transport. *J. Biol. Chem.* **277,** 25423–25430 (2002).

136. Karcher, R. L. *et al.* Cell cycle regulation of myosin-V by calcium/calmodulin-dependent protein kinase II. *Science* **293,** 1317–20 (2001).

137. Mercer, J. A., Seperack, P. K., Strobel, M. C., Copeland, N. G. & Jenkins, N. A. Novel myosin heavy chain encoded by murine dilute coat colour locus. *Nature* **349,** 709–13 (1991).

138. Ménasché, G. *et al.* Griscelli syndrome restricted to hypopigmentation results from a melanophilin defect (GS3) or a MYO5A F-exon deletion

(GS1). *J. Clin. Invest.* **112,** 450–456 (2003).

139. Desnos, C. *et al.* Rab27A and its effector MyRIP link secretory granules to F-actin and control their motion towards release sites. *J. Cell Biol.* **163,** 559–70 (2003).

140. Ivarsson, R., Jing, X., Waselle, L., Regazzi, R. & Renström, E. Myosin 5a controls insulin granule recruitment during late-phase secretion. *Traffic* **6,** 1027–35 (2005).

141. Naisbitt, S. *et al.* Interaction of the postsynaptic density-95/guanylate kinase domain-associated protein complex with a light chain of myosin-V and dynein. *J. Neurosci.* **20,** 4524–34 (2000).

142. Wagner, W., Brenowitz, S. D. & Hammer, J. A. Myosin-Va transports the endoplasmic reticulum into the dendritic spines of Purkinje neurons. *Nat. Cell Biol.* **13,** 40–8 (2011).

143. McCaffrey, M. W. & Lindsay, A. J. Roles for myosin Va in RNA transport and turnover. *Biochem. Soc. Trans.* **40,** 1416–1420 (2012).

144. Lindsay, A. J. & McCaffrey, M. W. Myosin Vb localises to nucleoli and associates with the RNA polymerase I transcription complex. *Cell Motil. Cytoskeleton* **66,** 1057–72 (2009).

145. Rodriguez, O. C. & Cheney, R. E. Human myosin-Vc is a novel class V myosin expressed in epithelial cells. *J. Cell Sci.* **115,** 991–1004 (2002).

146. The human protein atlas.

147. van Ijzendoorn, S. C. D. & Ijzendoorn, S. C. D. Van. Recycling endosomes. *J. Cell Sci.* **119,** 1679–81 (2006).

148. Lapierre, L. A. *et al.* Myosin vb is associated with plasma membrane recycling systems. *Mol. Biol. Cell* **12,** 1843–57 (2001).

149. Lapierre, L. A. & Goldenring, J. R. Interactions of myosin vb with rab11 family members and cargoes traversing the plasma membrane recycling system. *Methods Enzymol.* **403,** 715–23 (2005).

150. Schafer, J. C. *et al.* Rab11-FIP2 Interaction with MYO5B Regulates Movement of Rab11a-Containing Recycling Vesicles. *Traffic* **15,** 292–308 (2014).

151. Wang, X., Kumar, R., Navarre, J., Casanova, J. E. & Goldenring, J. R. Regulation of vesicle trafficking in madin-darby canine kidney cells by Rab11a and Rab25. *J. Biol. Chem.* **275,** 29138–46 (2000).

152. Dow, L. E. *et al.* Apc Restoration Promotes Cellular Differentiation and Reestablishes Crypt Homeostasis in Colorectal Cancer. *Cell* **161,** 1539–52 (2015).

153. Casanova, J. E. *et al.* Association of Rab25 and Rab11a with the apical recycling system of polarized Madin-Darby canine kidney cells. *Mol. Biol. Cell* **10,** 47–61 (1999).

154. Fan, G.-H., Lapierre, L. A., Goldenring, J. R., Sai, J. & Richmond, A. Rab11-family interacting protein 2 and myosin Vb are required for CXCR2 recycling and receptor-mediated chemotaxis. *Mol. Biol. Cell* **15,** 2456–69 (2004).

155. Hales, C. M. *et al.* Identification and characterization of a family of Rab11-interacting proteins. *J. Biol. Chem.* **276,** 39067–75 (2001).

156. Volpicelli, L. A., Lah, J. J., Fang, G., Goldenring, J. R. & Levey, A. I. Rab11a and myosin Vb regulate recycling of the M4 muscarinic acetylcholine receptor. *J. Neurosci.* **22,** 9776–84 (2002).

157. Lisé, M.-F. *et al.* Involvement of myosin Vb in glutamate receptor trafficking. *J. Biol. Chem.* **281,** 3669–78 (2006).

158. Liu, Y. *et al.* Myosin Vb controls biogenesis of post-Golgi Rab10 carriers during axon development. *Nat. Commun.* **4,** 194–205 (2013).

159. Chen, Y. *et al.* Myosin Vb gene is associated with schizophrenia in Chinese Han population. *Psychiatry Res.* **207,** 13–18 (2013).

160. Tzaban, S. *et al.* The recycling and transcytotic pathways for IgG transport by FcRn are distinct and display an inherent polarity. *J. Cell Biol.* **185,** 673–684 (2009).

161. Müller, T. *et al.* MYO5B mutations cause microvillus inclusion disease and disrupt epithelial cell polarity. *Nat. Genet.* **40,** 1163–5 (2008).

162. Li, B. X., Satoh, A. K. & Ready, D. F. Myosin V, Rab11, and dRip11 direct apical secretion and cellular morphogenesis in developing Drosophila photoreceptors. *J. Cell Biol.* **177,** 659–69 (2007).

163. Ducharme, N. A. *et al.* MARK2/EMK1/Par-1Balpha phosphorylation of Rab11-family interacting protein 2 is necessary for the timely establishment of polarity in Madin-Darby canine kidney cells. *Mol. Biol. Cell* **17,** 3625–37 (2006).

164. Lapierre, L. A. *et al.* Phosphorylation of Rab11-FIP2 regulates polarity in MDCK cells. *Mol. Biol. Cell* **23,** 2302–2318 (2012).

165. Wu, B. & Guo, W. The Exocyst at a Glance. *J. Cell Sci.* **128,** 2957–2964 (2015).

166. Bryant, D. M. *et al.* A molecular network for de novo generation of the apical surface and lumen. *Nat. Cell Biol.* **12,** 1035–1045 (2010).

167. Qin, Y., Meisen, W. H., Hao, Y. & Macara, I. G. Tuba, a Cdc42 GEF, is required for polarized spindle orientation during epithelial cyst formation. *J. Cell Biol.* **189,** 661–9 (2010).

168. Jaffe, A. B., Kaji, N., Durgan, J. & Hall, A. Cdc42 controls spindle orientation to position the apical surface during epithelial morphogenesis. *J. Cell Biol.* **183,** 625–633 (2008).

169. Joberty, G., Petersen, C., Gao, L. & Macara, I. G. The cell-polarity protein Par6 links Par3 and atypical protein kinase C to Cdc42. *Nat. Cell Biol.* **2,** 531–9 (2000).

170. Das, S. *et al.* Rab8a vesicles regulate Wnt ligand delivery and Paneth cell maturation at the intestinal stem cell niche. *Development* **142,** 2147–62 (2015).

171. Sato, T. *et al.* The Rab8 GTPase regulates apical protein localization in intestinal cells. *Nature* **448,** 366–9 (2007).

172. Knödler, A. *et al.* Coordination of Rab8 and Rab11 in primary ciliogenesis. *Proc. Natl. Acad. Sci. U. S. A.* **107,** 6346–51 (2010).

173. Khandelwal, P. *et al.* A Rab11a-Rab8a-Myo5B network promotes stretch-regulated exocytosis in bladder umbrella cells. *Mol. Biol. Cell* **24,** 1007–19 (2013).

174. ten Klooster, J. P. *et al.* Mst4 and Ezrin induce brush borders downstream of the Lkb1/Strad/Mo25 polarization complex. *Dev. Cell* **16,** 551–62 (2009).

175. Gloerich, M. *et al.* Rap2A links intestinal cell polarity to brush border formation. *Nat. Cell Biol.* **14,** 793–801 (2012).

176. Consonni, S. V, Brouwer, P. M., van Slobbe, E. S. & Bos, J. L. The PDZ domain of the guanine nucleotide exchange factor PDZGEF directs binding to phosphatidic acid during brush border formation. *PLoS One* **9,** e98253 (2014).

177. Wald, F. A. *et al.* Atypical protein kinase C (iota) activates ezrin in the apical domain of intestinal epithelial cells. *J. Cell Sci.* **121,** 644–54 (2008).

178. Shiue, H., Musch, M. W., Wang, Y., Chang, E. B. & Turner, J. R. Akt2 phosphorylates ezrin to trigger NHE3 translocation and activation. *J. Biol. Chem.* **280,** 1688–95 (2005).

179. Viswanatha, R., Ohouo, P. Y., Smolka, M. B. & Bretscher, A. Local phosphocycling mediated by LOK/SLK restricts ezrin function to the apical aspect of epithelial cells. *J. Cell Biol.* **199,** 969–84 (2012).

180. Davidson, G. P., Cutz, E., Hamilton, J. R. & Gall, D. G. Familial enteropathy: a syndrome of protracted diarrhea from birth, failure to thrive, and hypoplastic villus atrophy. *Gastroenterology* **75,** 783–90 (1978).

181. Cutz, E. *et al.* Microvillus Inclusion Disease: An Inherited Defect of Brush-Border Assembly and Differentiation. *N. Engl. J. Med.* **320,** 646–651 (1989).

182. Ruemmele, F. M., Schmitz, J. & Goulet, O. Microvillous inclusion disease (microvillous atrophy). *Orphanet J. Rare Dis.* **1,** 22 (2006).

183. Phillips, A. D. & Schmitz, J. Familial microvillous atrophy: a clinicopathological survey of 23 cases. *J. Pediatr. Gastroenterol. Nutr.* **14,** 380–96 (1992).

184. Halac, U. *et al.* Microvillous Inclusion Disease: How to Improve the Prognosis of a Severe Congenital Enterocyte Disorder. *J. Pediatr. Gastroenterol. Nutr.* **52,** 460–465 (2011).

185. Ruemmele, F. M. *et al.* Loss-of-function of MYO5B is the main cause of microvillus inclusion disease: 15 novel mutations and a CaCo-2 RNAi cell model. *Hum. Mutat.* **31,** 544–551 (2010).

186. van der Velde, K. J. *et al.* An overview and online registry of microvillus inclusion disease patients and their MYO5B mutations. *Hum. Mutat.* **34,** 1597–605 (2013).

187. Wiegerinck, C. L. *et al.* Loss of Syntaxin 3 Causes Variant Microvillus Inclusion Disease. *Gastroenterology* **147,** 65–68.e10 (2014).

188. Iancu, T. C., Mahajnah, M., Manov, I. & Shaoul, R. Microvillous inclusion disease: ultrastructural variability. *Ultrastruct. Pathol.* **31,** 173–88 (2007).

189. Delie, F. & Rubas, W. A human colonic cell line sharing similarities with enterocytes as a model to examine oral absorption: advantages and limitations of the Caco-2 model. *Crit. Rev. Ther. Drug Carrier Syst.* **14,** 221–86 (1997).

190. Thoeni, C. E. *et al.* Microvillus Inclusion Disease: Loss of Myosin Vb Disrupts Intracellular Traffic and Cell Polarity. *Traffic* **15,** 22–42 (2014).

191. Knowles, B. C. *et al.* Myosin Vb uncoupling from RAB8A and RAB11A elicits microvillus inclusion disease. *J. Clin. Invest.* **124,** 2947–2962 (2014).

192. Vogel, G. F. *et al.* Cargo-selective apical exocytosis in epithelial cells is conducted by Myo5B, Slp4a, Vamp7, and Syntaxin 3. *J. Cell Biol.* **211,** 587–604 (2015).

193. Sobajima, T. *et al.* Rab11a is required for apical protein localisation in the intestine. *Biol. Open* 1–9 (2014). doi:10.1242/bio.20148532

194. Michaux, G. *et al.* The localisation of the apical Par/Cdc42 polarity module is specifically affected in microvillus inclusion disease. *Biol. Cell* **108,** 19–28 (2016).

195. Melendez, J. *et al.* Cdc42 coordinates proliferation, polarity, migration, and differentiation of small intestinal epithelial cells in mice. *Gastroenterology* **145,** 808–19 (2013).

196. Sakamori, R. *et al.* Cdc42 and Rab8a are critical for intestinal stem cell division, survival, and differentiation in mice. *J. Clin. Invest.* **122,** 1052–65 (2012).

197. Zhang, X. & Gao, N. RAB and RHO GTPases regulate intestinal crypt cell homeostasis and enterocyte function. *Small GTPases* **7,** 59–64 (2016).

198. Overeem, A. W., Posovszky, C., Rings, E. H. M. M., Giepmans, B. N. G. & van IJzendoorn, S. C. D. The role of enterocyte defects in the pathogenesis of congenital diarrheal disorders. *Dis. Model. Mech.* **9,** 1–12 (2016).

199. Sidhaye, J. *et al.* The zebrafish goosepimples/myosin Vb mutant exhibits cellular attributes of human microvillus inclusion disease. *Mech. Dev.* **142,** 62–74 (2016).

200. Chen, X. *et al.* Organellar Proteomics: Analysis of Pancreatic Zymogen Granule Membranes. *Mol. Cell. Proteomics* **5,** 306–312 (2005).

201. Marchelletta, R. R., Jacobs, D. T., Schechter, J. E., Cheney, R. E. & Hamm-Alvarez, S. F. The class V myosin motor, myosin 5c, localizes to mature secretory vesicles and facilitates exocytosis in lacrimal acini. *Am. J. Physiol. Cell Physiol.* **295,** C13-28 (2008).

202. Jacobs, D. T., Weigert, R., Grode, K. D., Donaldson, J. G. & Cheney, R. E. Myosin Vc Is a Molecular Motor That Functions in Secretory Granule Trafficking. *Mol. Biol. Cell* **20,** 4471–4488 (2009).

203. Bultema, J. J. *et al.* Myosin Vc Interacts with Rab32 and Rab38 Proteins and Works in the Biogenesis and Secretion of Melanosomes. *J. Biol. Chem.* **289,** 33513–33528 (2014).

204. Watanabe, S. *et al.* Human myosin Vc is a low duty ratio nonprocessive motor. *J. Biol. Chem.* **283,** 10581–92 (2008).

205. Sladewski, T. E., Krementsova, E. B. & Trybus, K. M. Myosin Vc Is Specialized for Transport on a Secretory Superhighway. *Curr. Biol.* **26,** 2202–2207 (2016).

206. Ouderkirk, J. L. & Krendel, M. Non-muscle myosins in tumor progression, cancer cell invasion, and metastasis. *Cytoskeleton* **71,** 447–463 (2014).

207. Li, Y.-R. & Yang, W.-X. Myosins as fundamental components during tumorigenesis: diverse and indispensable. *Oncotarget* **7,** 46785–46812 (2015).

208. van Diepen, M. T. *et al.* MyosinV controls PTEN function and neuronal cell size. *Nat. Cell Biol.* **11,** 1191–6 (2009).

209. Izidoro-Toledo, T. C. *et al.* A myosin-Va tail fragment sequesters dynein light chains leading to apoptosis in melanoma cells. *Cell Death Dis.* **4,** e547 (2013).

210. Lan, L. *et al.* Upregulation of myosin Va by Snail is involved in cancer cell migration and metastasis. *Int. J. cancer* **126,** 53–64 (2010).

211. Dong, W. *et al.* Inactivation of MYO5B promotes invasion and motility in gastric cancer cells. *Dig. Dis. Sci.* **57,** 1247–1252 (2012).

212. Dong, W., Qin, G., Shen, R. & Hospital, R. Rab11-FIP2 promotes the metastasis of gastric cancer cells.

213. Nam, K. T. *et al.* Loss of Rab25 promotes the development of intestinal neoplasia in mice and is associated with human colorectal adenocarcinomas. *J. Clin. Invest.* **120,** 840–849 (2010).

214. Goldenring, J. R. & Nam, K. T. Rab25 as a tumour suppressor in colon carcinogenesis. *Br. J. Cancer* **104,** 33–36 (2011).

215. Kuang, S.-Q. *et al.* Genome-wide identification of aberrantly methylated promoter associated CpG islands in acute lymphocytic

leukemia. *Leukemia* **22,** 1529–38 (2008).

216. Martínez-López, E. *et al.* Allelic loss on chromosome 18q as a prognostic marker in stage II colorectal cancer. *Gastroenterology* **114,** 1180–7 (1998).

217. Mazzolini, R. *et al.* Brush border Myosin Ia has tumor suppressor activity in the intestine. *Proc. Natl. Acad. Sci.* **109,** 1530–1535 (2011).

218. Goldenring, J. R. A central role for vesicle trafficking in epithelial neoplasia: intracellular highways to carcinogenesis. *Nat. Rev. Cancer* **13,** 813–20 (2013).

219. Skarnes, W. C. *et al.* A conditional knockout resource for the genome-wide study of mouse gene function. *Nature* **474,** 337–42 (2011).

220. Testa, G. *et al.* A reliable lacZ expression reporter cassette for multipurpose, knockout-first alleles. *Genesis* **38,** 151–8 (2004).

221. Kranz, A. *et al.* An improved Flp deleter mouse in C57Bl/6 based on Flpo recombinase. *Genesis* **48,** 512–20 (2010).

222. el Marjou, F. *et al.* Tissue-specific and inducible Cre-mediated recombination in the gut epithelium. *Genesis* **39,** 186–93 (2004).

223. Meerbrey, K. L. *et al.* The pINDUCER lentiviral toolkit for inducible RNA interference in vitro and in vivo. *Proc. Natl. Acad. Sci. U. S. A.* **108,** 3665–70 (2011).

224. Paddison, P. J. *et al.* Cloning of short hairpin RNAs for gene knockdown in mammalian cells. *Nat. Methods* **1,** 163–7 (2004).

225. Baas, A. F. *et al.* Complete polarization of single intestinal epithelial cells upon activation of LKB1 by STRAD. *Cell* **116,** 457–66 (2004).

226. Peterson, M. D. & Mooseker, M. S. Characterization of the enterocyte-like brush border cytoskeleton of the C2BBe clones of the human intestinal cell line, Caco-2. *J. Cell Sci.* 581–600 (1992). at <http://www.ncbi.nlm.nih.gov/pubmed/1506435>

227. Truett, G. E. *et al.* Preparation of PCR-quality mouse genomic DNA with hot sodium hydroxide and tris (HotSHOT). *Biotechniques* **29,** 52, 54 (2000).

228. Bazzocco, S. *et al.* Highly Expressed Genes in Rapidly Proliferating Tumor Cells as New Targets for Colorectal Cancer Treatment. *Clin. Cancer Res.* **21,** 3695–704 (2015).

229. Szperl, A. M. *et al.* Functional Characterization of Mutations in the Myosin Vb Gene Associated With Microvillus Inclusion Disease. *J. Pediatr. Gastroenterol. Nutr.* **52,** 307–313 (2011).

230. Alhopuro, P. *et al.* SMAD4 levels and response to 5-fluorouracil in colorectal cancer. *Clin. Cancer Res.* **11,** 6311–6 (2005).

231. Peterson, M. D. & Mooseker, M. S. Characterization of the enterocyte-like brush border cytoskeleton of the C2BBe clones of the human intestinal cell line, Caco-2. *J. Cell Sci.* 581–600 (1992). at <http://www.ncbi.nlm.nih.gov/pubmed/1506435>

232. Vogelstein, B. *et al.* Cancer Genome Landscapes. *Science (80-.).* **339,** 1546–1558 (2013).

233. Wodarz, A. & Näthke, I. Cell polarity in development and cancer. *Nat. Cell Biol.* **9,** 1016–24 (2007).

234. Chantret, I., Barbat, A., Dussaulx, E., Brattain, M. G. & Zweibaum, A. Epithelial polarity, villin expression, and enterocytic differentiation of cultured human colon carcinoma cells: a survey of twenty cell lines. *Cancer Res.* **48,** 1936–42 (1988).

235. Pinto M, Robine-Leon S, Appay M-D, et al. Enterocyte-like differentiation and polarization of the human colon carcinoma cell line Caco-2 in culture. *Biol. Cell* **47,** 323–30 (1983).

236. Ramond, M. J., Martinot-Peignoux, M. & Erlinger, S. Dome formation in the human colon carcinoma cell line Caco-2 in culture. Influence of ouabain and permeable supports. *Biol. cell* **54,** 89–92 (1985).

237. Hara, A. *et al.* Changes of proliferative activity and phenotypes in spontaneous differentiation of a colon cancer cell line. *Jpn. J. Cancer Res.* **84,** 625–32 (1993).

238. Abe, M. *et al.* Mechanisms of confluence-dependent expression of CD26 in colon cancer cell lines. *BMC Cancer* **11,** 51 (2011).

239. Rodrigues, P. *et al.* RHOA inactivation enhances Wnt signalling and promotes colorectal cancer. *Nat. Commun.* **5,** 5458 (2014).

240. Blouin, J.-M. *et al.* Butyrate elicits a metabolic switch in human colon cancer cells by targeting the pyruvate dehydrogenase complex. *Int. J. cancer* **128,** 2591–601 (2011).

241. Shin, J. *et al.* The Intestinal Epithelial Cell Differentiation Marker Intestinal Alkaline Phosphatase (ALPi) Is Selectively Induced by Histone Deacetylase Inhibitors (HDACi) in Colon Cancer Cells in a

Kruppel-like Factor 5 (KLF5)-dependent Manner. *J. Biol. Chem.* **289,** 25306–25316 (2014).

242. Nürnberg, A., Kitzing, T. & Grosse, R. Nucleating actin for invasion. *Nat. Rev. Cancer* **11,** 177–187 (2011).

243. ten Klooster, J. P. *et al.* Mst4 and Ezrin Induce Brush Borders Downstream of the Lkb1/Strad/Mo25 Polarization Complex. *Dev. Cell* **16,** 551–562 (2009).

244. Cartón-García, F. *et al.* Myo5b knockout mice as a model of microvillus inclusion disease. *Sci. Rep.* **5,** 12312 (2015).

245. Segre, J. A., Bauer, C. & Fuchs, E. Klf4 is a transcription factor required for establishing the barrier function of the skin. *Nat. Genet.* **22,** 356–60 (1999).

246. Miyazaki, M., Dobrzyn, A., Elias, P. M. & Ntambi, J. M. Stearoyl-CoA desaturase-2 gene expression is required for lipid synthesis during early skin and liver development. *Proc. Natl. Acad. Sci. U. S. A.* **102,** 12501–6 (2005).

247. Turgeon, B., Meloche, S. & Recherche, I. De. Interpreting Neonatal Lethal Phenotypes in Mouse Mutants : Insights Into Gene Function and Human Diseases. 1–26 (2009). doi:10.1152/physrev.00040.2007.

248. Scheuner, D. *et al.* Translational control is required for the unfolded protein response and in vivo glucose homeostasis. *Mol. Cell* **7,** 1165–76 (2001).

249. Kuma, A. *et al.* The role of autophagy during the early neonatal starvation period. *Nature* **432,** 1032–1036 (2004).

250. Vogel, G. F. *et al.* Cargo-selective apical exocytosis in epithelial cells is conducted by Myo5B, Slp4a, Vamp7, and Syntaxin 3. *J. Cell Biol.* **211,** (2015).

251. Shaw, D., Gohil, K. & Basson, M. D. Intestinal mucosal atrophy and adaptation. *World J. Gastroenterol.* **18,** 6357 (2012).

252. Buchman, A. L. *et al.* Parenteral Nutrition Is Associated With Intestinal Morphologic and Functional Changes in Humans. *J. Parenter. Enter. Nutr.* **19,** 453–460 (1995).

253. Weis, V. G. *et al.* Loss of MYO5B in Mice Recapitulates Microvillus Inclusion Disease and Reveals an Apical Trafficking Pathway Distinct to Neonatal Duodenum. *C. Cell. Mol. Gastroenterol. Hepatol.* **2,** 131–157 (2016).

254. Schneeberger, K. *et al.* An inducible mouse model for microvillus inclusion disease reveals a role for myosin Vb in apical and basolateral trafficking. *Proc. Natl. Acad. Sci.* 201516672 (2015). doi:10.1073/pnas.1516672112

255. Yui, S. *et al.* Functional engraftment of colon epithelium expanded in vitro from a single adult Lgr5$^+$ stem cell. *Nat. Med.* **18,** 618–23 (2012).

256. Martin-Belmonte, F. & Perez-Moreno, M. Epithelial cell polarity, stem cells and cancer. *Nat. Rev. Cancer* **12,** 23–38 (2011).

257. Muthuswamy, S. K. & Xue, B. Cell Polarity as a Regulator of Cancer Cell Behavior Plasticity. *Annu. Rev. Cell Dev. Biol.* **28,** 599–625 (2012).

258. Royer, C. & Lu, X. Epithelial cell polarity: a major gatekeeper against cancer? *Cell Death Differ.* **18,** 1470–1477 (2011).

259. McCaffrey, L. M. & Macara, I. G. Epithelial organization, cell polarity and tumorigenesis. *Trends Cell Biol.* **21,** 727–735 (2011).

260. Halaoui, R. & McCaffrey, L. Rewiring cell polarity signaling in cancer. *Oncogene* **34,** 939–950 (2015).

261. Herrmann, J. L., Byekova, Y., Elmets, C. A. & Athar, M. Liver Kinase B1 (LKB1) in the pathogenesis of epithelial cancers. *Cancer Lett.* **306,** 1–9 (2011).

262. Bardeesy, N. *et al.* Loss of the Lkb1 tumour suppressor provokes intestinal polyposis but resistance to transformation. *Nature* **419,** 162–167 (2002).

263. Stenmark, H. Rab GTPases as coordinators of vesicle traffic. *Nat. Rev. Mol. Cell Biol.* **10,** 513–25 (2009).

264. Kravtsov, D. V. *et al.* Identification of intestinal ion transport defects in microvillus inclusion disease. *Am. J. Physiol. - Gastrointest. Liver Physiol.* **311,** G142–G155 (2016).

265. Forcet, C. *et al.* Functional analysis of Peutz-Jeghers mutations reveals that the LKB1 C-terminal region exerts a crucial role in regulating both the AMPK pathway and the cell polarity. *Hum. Mol. Genet.* **14,** 1283–92 (2005).

266. Trojan, J., Brieger, A., Raedle, J., Esteller, M. & Zeuzem, S. 5′-CpG island methylation of the LKB1/STK11 promoter and allelic loss at chromosome 19p13.3 in sporadic colorectal cancer. *Gut* **47,** 272–6

(2000).

267. Wang, Z. J., Taylor, F., Churchman, M., Norbury, G. & Tomlinson, I. Genetic pathways of colorectal carcinogenesis rarely involve the PTEN and LKB1 genes outside the inherited hamartoma syndromes. *Am. J. Pathol.* **153,** 363–6 (1998).

268. Kravtsov, D. *et al.* Myosin 5b loss of function leads to defects in polarized signaling: implication for microvillus inclusion disease pathogenesis and treatment. *Am. J. Physiol. Gastrointest. Liver Physiol.* **307,** G992–G1001 (2014).

269. Murray, N. R. *et al.* Protein kinase Cι is required for Ras transformation and colon carcinogenesis in vivo. *J. Cell Biol.* **164,** 797–802 (2004).

270. Murray, N. R., Weems, J., Braun, U., Leitges, M. & Fields, A. P. Protein Kinase C II and PKC / : Collaborating Partners in Colon Cancer Promotion and Progression. *Cancer Res.* **69,** 656–662 (2009).

271. Murray, N. R., Kalari, K. R. & Fields, A. P. Protein kinase Cι expression and oncogenic signaling mechanisms in cancer. *J. Cell. Physiol.* **226,** 879–87 (2011).

272. Eder, A. M. *et al.* Atypical PKCiota contributes to poor prognosis through loss of apical-basal polarity and cyclin E overexpression in ovarian cancer. *Proc. Natl. Acad. Sci. U. S. A.* **102,** 12519–24 (2005).

273. Kojima, Y. *et al.* The overexpression and altered localization of the atypical protein kinase C lambda/iota in breast cancer correlates with the pathologic type of these tumors. *Hum. Pathol.* **39,** 824–31 (2008).

274. Weis, V. G. *et al.* Loss of MYO5B in Mice Recapitulates Microvillus Inclusion Disease and Reveals an Apical Trafficking Pathway Distinct to Neonatal Duodenum. *Cell. Mol. Gastroenterol. Hepatol.* **2,** 131–157 (2016).

275. Schneeberger, K. *et al.* An inducible mouse model for microvillus inclusion disease reveals a role for myosin Vb in apical and basolateral trafficking. *Proc. Natl. Acad. Sci.* **112,** 12408–12413 (2015).

276. Children, H. S. Microvillus inclusion disease : specific diagnostic features shown by alkaline phosphatase histochemistry. *J. Clin. Pathol.* 880–882 (1988).

277. Turecková, J., Vojtechová, M., Kucerová, D., Velek, J. & Tuhácková, Z. Sodium butyrate-mediated differentiation of colorectal cancer cells: regulation of PKCbetaII by PI 3-kinase. *Int. J. Mol. Med.* **15,** 329–35

(2005).

278. Mariadason, J. M., Velcich, a, Wilson, a J., Augenlicht, L. H. & Gibson, P. R. Resistance to butyrate-induced cell differentiation and apoptosis during spontaneous Caco-2 cell differentiation. *Gastroenterology* **120,** 889–899 (2001).

279. Orchel, A., Dzierzewicz, Z., Parfiniewicz, B., Weglarz, L. & Wilczok, T. Butyrate-induced differentiation of colon cancer cells is PKC and JNK dependent. *Dig. Dis. Sci.* **50,** 490–8 (2005).

280. Knoblich, J. A. Asymmetric cell division: recent developments and their implications for tumour biology. *Nat. Rev. Mol. Cell Biol.* **11,** 849–60 (2010).

281. Quyn, A. J. *et al.* Spindle orientation bias in gut epithelial stem cell compartments is lost in precancerous tissue. *Cell Stem Cell* **6,** 175–81 (2010).

282. Melendez, J. *et al.* Cdc42 coordinates proliferation, polarity, migration, and differentiation of small intestinal epithelial cells in mice. *Gastroenterology* **145,** 808–19 (2013).

283. Sakamori, R. *et al.* Cdc42 and Rab8a are critical for intestinal stem cell division , survival , and differentiation in mice. **122,** (2012).

284. Warner, S. J., Yashiro, H. & Longmore, G. D. The Cdc42/Par6/aPKC polarity complex regulates apoptosis-induced compensatory proliferation in epithelia. *Curr. Biol.* **20,** 677–86 (2010).

285. Sakamori, R. *et al.* CDC42 inhibition suppresses progression of incipient intestinal tumors. *Cancer Res.* **74,** 5480–92 (2014).

286. Durgan, J., Kaji, N., Jin, D. & Hall, A. Par6B and Atypical PKC Regulate Mitotic Spindle Orientation during Epithelial Morphogenesis. *J. Biol. Chem.* **286,** 12461–12474 (2011).

287. Das, S. *et al.* Rab8a vesicles regulate Wnt ligand delivery and Paneth cell maturation at the intestinal stem cell niche. *Development* **142,** 2147–62 (2015).

288. Barker, N. *et al.* Crypt stem cells as the cells-of-origin of intestinal cancer. *Nature* **457,** 608–611 (2009).

289. Yamashita, Y. M., Jones, D. L. & Fuller, M. T. Orientation of Asymmetric Stem Cell Division by the APC Tumor Suppressor and Centrosome. *Science (80-.).* **301,** 1547–1550 (2003).

290. Chung, C. K., Zaino, R. J. & Stryker, J. A. Colorectal carcinoma: evaluation of histologic grade and factors influencing prognosis. *J. Surg. Oncol.* **21,** 143–8 (1982).

291. Thiery, J. P. & Sleeman, J. P. Complex networks orchestrate epithelial–mesenchymal transitions. *Nat. Rev. Mol. Cell Biol.* **7,** 131–142 (2006).

292. Williams, K. C. & Coppolino, M. G. Phosphorylation of Membrane Type 1-Matrix Metalloproteinase (MT1-MMP) and Its Vesicle-associated Membrane Protein 7 (VAMP7)-dependent Trafficking Facilitate Cell Invasion and Migration. *J. Biol. Chem.* **286,** 43405–43416 (2011).

293. Rainero, E. *et al.* Diacylglycerol kinase α controls RCP-dependent integrin trafficking to promote invasive migration. *J. Cell Biol.* **196,** 277–295 (2012).

294. Krishnan, M., Lapierre, L. A., Knowles, B. C. & Goldenring, J. R. Rab25 regulates integrin expression in polarized colonic epithelial cells. *Mol. Biol. Cell* **24,** 818–31 (2013).

295. Lioni, M. *et al.* Dysregulation of claudin-7 leads to loss of E-cadherin expression and the increased invasion of esophageal squamous cell carcinoma cells. *Am. J. Pathol.* **170,** 709–21 (2007).

296. Jones, R. G. *et al.* Conditional deletion of beta1 integrins in the intestinal epithelium causes a loss of Hedgehog expression, intestinal hyperplasia, and early postnatal lethality. *J. Cell Biol.* **175,** 505–14 (2006).

297. Lurje, G., Zhang, W. & Lenz, H.-J. Molecular Prognostic Markers in Locally Advanced Colon Cancer. *Clin. Colorectal Cancer* **6,** 683–690 (2007).

298. Alazzouzi, H. *et al.* SMAD4 as a prognostic marker in colorectal cancer. *Clin. Cancer Res.* **11,** 2606–11 (2005).

299. Lech, G., Słotwiński, R., Słodkowski, M. & Krasnodębski, I. W. Colorectal cancer tumour markers and biomarkers: Recent therapeutic advances. *World J. Gastroenterol.* **22,** 1745–55 (2016).

300. Ogino, S. *et al.* CpG island methylator phenotype, microsatellite instability, BRAF mutation and clinical outcome in colon cancer. *Gut* **58,** 90–6 (2009).

www.nature.com/scientificreports

SCIENTIFIC REPORTS

OPEN

Myo5b knockout mice as a model of microvillus inclusion disease

Fernando Cartón-García[1,2], Arend W. Overeem[3], Rocio Nieto[1,2], Sarah Bazzocco[1,2], Higinio Dopeso[1,2], Irati Macaya[1,2], Josipa Bilic[1,2], Stefania Landolfi[4], Javier Hernandez-Losa[4], Simo Schwartz Jr[5], Santiago Ramon y Cajal[4], Sven C. D. van Ijzendoorn[3] & Diego Arango[1,2]

Received: 24 March 2015
Accepted: 25 June 2015
Published: 23 July 2015

Inherited *MYO5B* mutations have recently been associated with microvillus inclusion disease (MVID), an autosomal recessive syndrome characterized by intractable, life-threatening, watery diarrhea appearing shortly after birth. Characterization of the molecular mechanisms underlying this disease and development of novel therapeutic approaches is hampered by the lack of animal models. In this study we describe the phenotype of a novel mouse model with targeted inactivation of *Myo5b*. *Myo5b* knockout mice show perinatal mortality, diarrhea and the characteristic mislocalization of apical and basolateral plasma membrane markers in enterocytes. Moreover, in transmission electron preparations, we observed microvillus atrophy and the presence of microvillus inclusion bodies. Importantly, *Myo5b* knockout embryos at day 20 of gestation already display all these structural defects, indicating that they are tissue autonomous rather than secondary to environmental cues, such as the long-term absence of nutrients in the intestine. *Myo5b* knockout mice closely resemble the phenotype of MVID patients and constitute a useful model to further investigate the underlying molecular mechanism of this disease and to preclinically assess the efficacy of novel therapeutic approaches.

Microvillus inclusion disease (MVID) is an autosomal recessive syndrome affecting the intestinal epithelium[1,2]. It was first described in 1978 and it is characterized by the onset of abundant neonatal watery diarrhea that most commonly starts within the first days of life, and can cause the loss of up to 30% of body weight within 24 h[1,2]. In some cases (<20%), MVID manifests at later times, within the first 3–4 months of life.

The diagnosis of MVID is based on the detection of morphological abnormalities in the intestinal epithelium using a combination of light and electron microscopy. Histological examination of the small intestinal mucosa reveals a variable degree of villus atrophy. In addition, there is a characteristic accumulation of periodic acid–Schiff (PAS)-positive cytoplasmic granules in intestinal epithelial cells[3,4]. Transmission electron microscopy (TEM) of intestinal epithelial biopsies is used to confirm the diagnosis. Ultrastructural defects in small intestinal enterocytes include the shortening of microvilli and the presence of distinctive cytoplasmic vacuoles lined by microvilli, known as microvillus inclusion bodies[5].

Inactivating mutations in *MYO5B* have recently been associated with the majority of cases of MVID[6,7]. *MYO5B* codes for the unconventional myosin Vb, an actin-based motor involved in plasma membrane recycling through its interactions with RAB GTPases[8]. The loss of a functional Myosin Vb protein results in profound protein trafficking defects in enterocytes leading to the mistargeting of apical and basolateral proteins[9,10]. These abnormalities in the structure of the apical brush border and the mislocalization of membrane proteins are likely responsible for the absorption defects and the watery diarrhea observed in

[1]Group of Molecular Oncology, CIBBIM-Nanomedicine, Vall d'Hebron University Hospital Research Institute (VHIR), Universitat Autònoma de Barcelona, Barcelona, Spain. [2]CIBER de Bioingeniería, Biomateriales y Nanomedicina (CIBER-BBN), Zaragoza, Spain. [3]Department of Cell Biology, University of Groningen, University Medical Center Groningen, Groningen, The Netherlands. [4]Department of Pathology, Vall d'Hebron Hospital, Barcelona, Spain. [5]Group of Drug Delivery and Targeting, CIBBIM-Nanomedicine, Vall d'Hebron University Hospital Research Institute (VHIR), Universitat Autònoma de Barcelona, Barcelona, Spain. Correspondence and requests for materials should be addressed to D.A. (email: diego.arango@vhir.org)

these patients, but the detailed molecular mechanisms remain to be fully elucidated. Currently, the only treatment options available for this uniformly fatal disease are total parenteral nutrition and intestinal transplant[11].

Here we describe the phenotype of the first animal model with targeted inactivation of *Myo5b*. Mice deficient for this myosin show perinatal mortality, watery diarrhea and the characteristic structural defects of patients with MVID. This study provides formal demonstration of *MYO5B* mutations as the cause of microvillus inclusion disease. Moreover, the availability of this mouse model will decisively contribute to shed new light on the underlying molecular mechanisms of this disease and the development and testing of new therapeutic approaches for MVID patients.

Results

Survival of *Myo5b* knockout mice. Homologous recombination was used to introduce a targeting cassette including the mouse En2 splice acceptor and the SV40 polyadenylation sequences after exon 4 of *Myo5b*, which is predicted to generate a null allele through splicing to a lacZ "gene trap" element (Supplementary Figure 1)[12]. As expected, mice homozygous for the trapped allele showed no Myosin Vb expression in their intestine (henceforth referred to as *Myo5b* knockout mice; Fig. 1). Wild type, heterozygous or *Myo5b* knockout embryos at day 20 of gestation (E20) showed no difference in their size or weight (Fig. 2A,B). Animals were born at Mendelian ratios ($n = 99$; Chi-square test, $p = 0.14$; Fig. 2C), but *Myo5b* knockout mice invariably died within the first 12 h after being born (Fig. 2D). No differences were observed between wild type and knockout newborn mice in their body size (Fig. 2E) or the gross histology of the gastrointestinal tract (Supplementary Figure 2) or other organs studied, including the lungs, liver, central nervous system, heart, pancreas and spleen. No cyanotic episodes or respiratory distress was observed in *Myo5b* knockout mice. However, newborn *Myo5b* knockout mice showed reduced bodyweight compared to wild type and heterozygous mice (Fig. 2F). Moreover, knockout mice showed signs of diarrhea and wrinkled skin, possibly due to dehydration (Fig. 2G,H). Although newborn *Myo5b* knockout mice showed no suckling defects (presence of a milk spot; Fig. 2G,H), they had significantly reduced blood glucose levels compared to wild type and heterozygous littermates (Fig. 2I). This is consistent with the watery diarrhea and absorption defects observed in patients with MVID[1,2] and likely contributed to the death of the *Myo5b* knockout mice within hours of birth[13].

Mislocalization of apical brush border proteins in the enterocytes of *Myo5b* knockout mice. At the ultrastructural level, the intestinal enterocytes of *Myo5b* knockout newborn mice showed the characteristic cytoplasmic accumulation of periodic-acid Schiff (PAS) staining observed in MVID patients[3,4] (Fig. 3A,B). Moreover, proteins normally expressed in the apical membrane of intestinal enterocytes such as alkaline phosphatase (ALP; Fig. 3C,D), 5'-Nucleotidase (5'NT; Fig. 3E,F) and ezrin (Fig. 3G,H) mislocalized to the basolateral membrane or the cytoplasm. Transferrin receptor (TfR) accumulated in the basal cytoplasm of enterocytes from *Myo5b* knockout mice (Fig. 3I,J), while other basolateral markers such as E-cadherin (Fig. 3K,L) and β-catenin (Fig. 3M,N) were unaffected. Notably, in some epithelial cells of *Myo5b* knockout mice ezrin (Fig. 3G,H) and actin (Fig. 3O,P) were found in circular cytoplasmic structures, closely resembling microvillus inclusions. These findings are in good agreement with the protein sorting defects observed in the intestinal epithelium of patients with MVID[3,6,14,15]. Importantly, these structural defects were also observed in E20 embryos (Supplementary Figure 3A–L).

Ultrastructural defects in the brush border of the enterocytes of *Myo5b* knockout mice. Transmission electron microscopy (TEM) analysis of the intestinal epithelium revealed the presence of microvillus inclusion bodies in the cytoplasm of absorptive cells from *Myo5b* knockout E20 embryos (Fig. 4A). In addition, the apical surface of the intestinal enterocytes showed widespread microvilli atrophy and reduced packing with areas with few/absent microvilli (Fig. 4B–D and Supplementary Figure 4) and presence of microvilli in the lateral plasma membrane (Fig. 4E,F). Vesicles were frequently observed at the apical plasma membrane in *Myo5b* wild type mice but not in the *Myo5b* knockout animals, where a characteristic accumulation of vesicles could be observed underneath the terminal web (Fig. 4B and Supplementary Figure 4). These ultrastructural abnormalities closely resemble the phenotype observed in the intestinal epithelium of patients with MVID (Fig. 5A–C)[4,5].

Discussion

We describe here the phenotype of the first mouse model with targeted inactivation of *Myo5b*. Germline mutations in this gene are associated with microvillus inclusion disease (MVID)[6], a congenital disorder of the intestinal epithelium causing persistent life-threatening watery diarrhea[1,2]. Myosin Vb is an actin-based molecular motor with a key role in vesicle trafficking and plasma membrane recycling through its interaction with the small GTPases RAB11 and RAB8[8,9]. It is not surprising, therefore, that inactivation of either *Rab11a* or *Rab8a* in the mouse intestine resulted in nutrient malabsorption, intracellular accumulation of apical proteins in intestinal epithelial cells, shortening of microvilli and microvillus inclusion bodies[16,17]. Interestingly, inactivation of the small GTPase *Cdc42* also caused microvilli shortening and microvillus inclusions in intestinal epithelial cells[18]. However, diarrhea, one of the hallmarks of MVID patients, was not observed in *Rab11* or *Cdc42* knockout mice[17,18], and *Rab8* knock out mice survived for approximately 5 weeks after birth, more closely resembling the phenotype of late

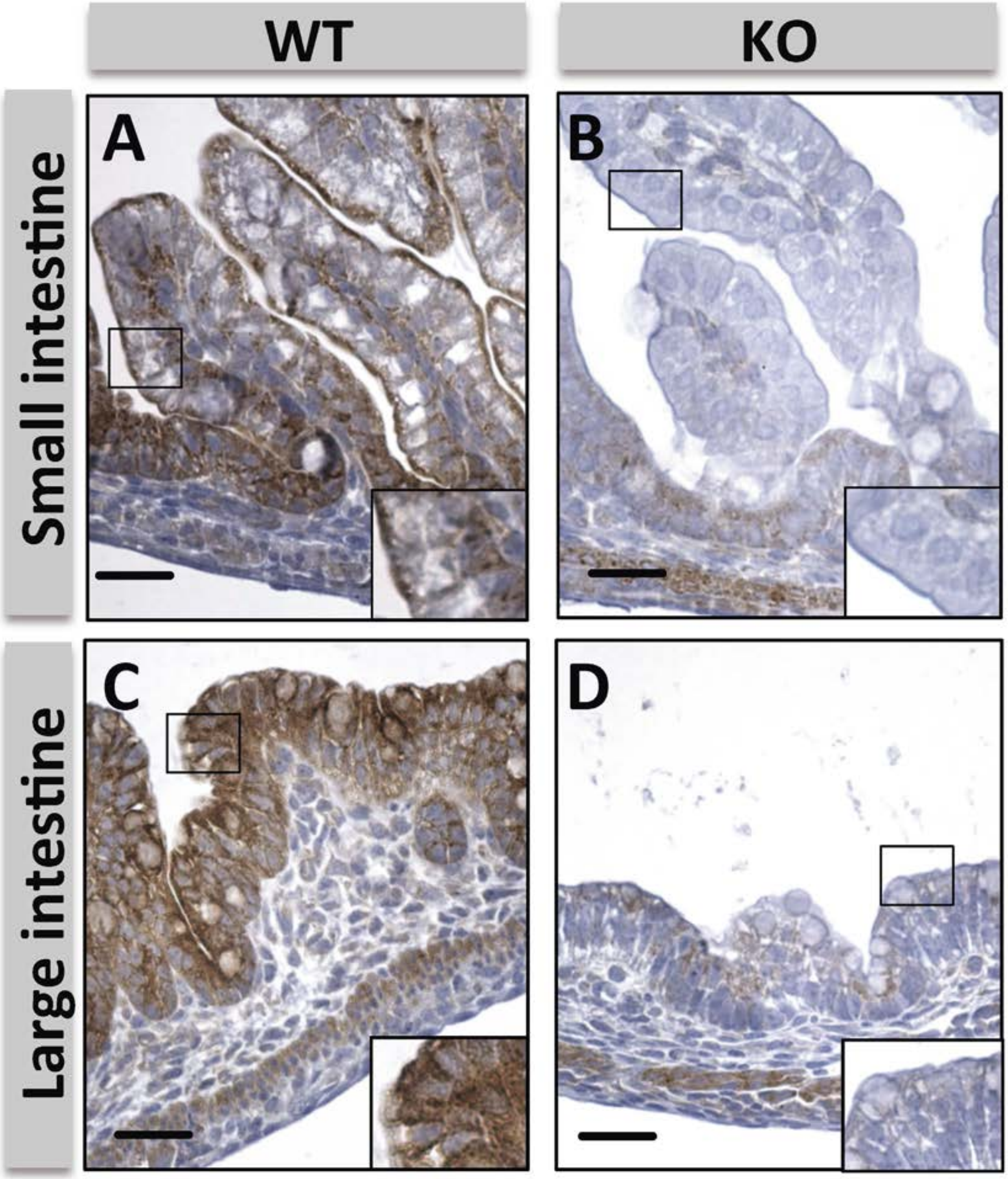

Figure 1. Effects of *Myo5b* inactivation. Immunostaining showing Myosin Vb levels in the small (**A,B**) and large (**C,D**) intestine of *Myo5b* wild type (**A** and **C**) and knockout (**B** and **D**) newborn mice. Scale bar: 50 μm.

onset MVID. Importantly, no mutations in *RAB8* or *RAB11* GTPases have been identified in *MYO5B* mutation negative MVID patients[19], suggesting that *Myo5b* deficient mice represent the optimal animal model for human microvillus inclusion disease.

Indeed, *Myo5b* knockout mice showed all the typical features observed in patients with early onset MVID, the most common form of this disease accounting for >80% of the cases[4]. *Myo5b* deficient mice showed no overt defects during embryonic development, having normal size and weight. However, newborn *Myo5b* knockout mice showed watery diarrhea and died during the first 12 h of life, likely due to dehydration and/or reduced nutrient availability secondary to absorption defects, as exemplified by the low blood glucose levels observed, although the contribution of each of these symptoms to the death of Myo5b deficient mice cannot be conclusively determined. The body weight reduction observed in *Myo5b* knockout mice (8% in approximately 6 h) is consistent with the fluid loss reported in early onset MVID patients (>30% of body weight in 24 h; i.e., 7.5% in 6 h)[3]. In previous studies, the perinatal mortality of *Klf4* or *Scd2* newborn knockout mice was attributed to a 5–10% reduction of body weight due to transepidermal water loss[20,21]. In humans, this rapid rate of dehydration would result in hypovolemic shock leading to death, as observed in *Myo5b* knockout mice. On the other hand, newborn mice have

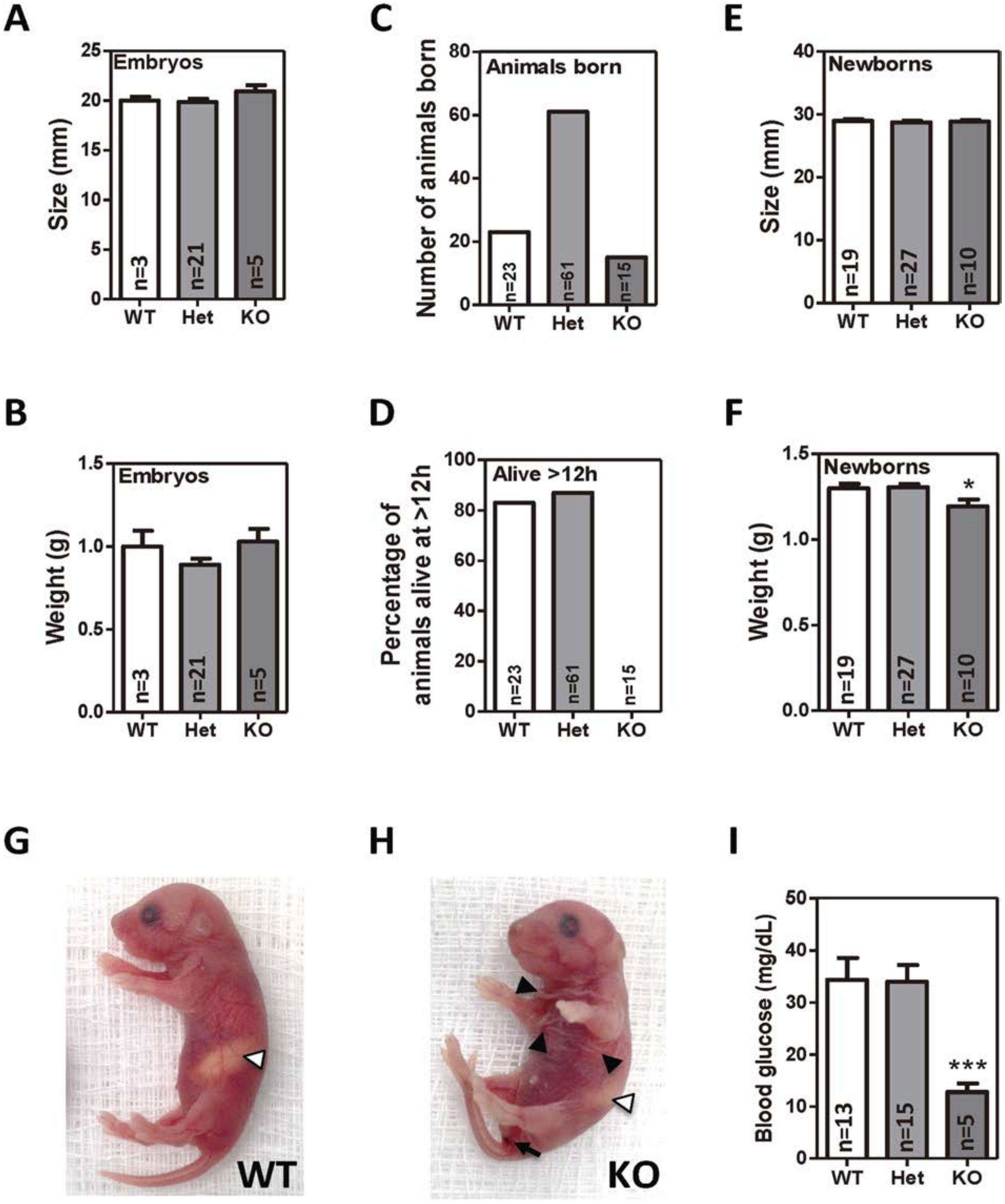

Figure 2. Phenotype of *Myo5b* E20 embryos and newborn mice. Size (**A**) and weight (**B**) of E20 embryos by *Myo5b* genotype. The mean ± SEM is shown. N = number of animals per group. (**C**) Genotype of 99 mice born from crossing heterozygous male and female mice. (**D**) Percentage of these 99 mice that were alive 12 h after birth. Size (**E**) and weight (**F**) of newborn mice by *Myo5b* genotype (mean ± SEM). Newborn wild type (**G**) and *Myo5b* knockout (**H**) mice showing the presence of the milk spot (white arrowhead), wrinkled skin (black arrowhead) and evidence of diarrhea (arrow). (**I**) Histogram showing average (±SEM) blood glucose levels in *Myo5b* wild type, heterozygous and newborn mice. $^{*}p < 0.05$; $^{***}p < 0.001$ (Student's T-test).

previously been shown to go through a transitory phase of severe hypoglycemia (about 10 mg/dL within 2 h of birth) until glucose levels are restored due to gluconeogenesis and eventually nutrient absorption of maternal milk[13,22,23]. Consistent with the phenotype observed in *Myo5b* knockout animals, the incapacity

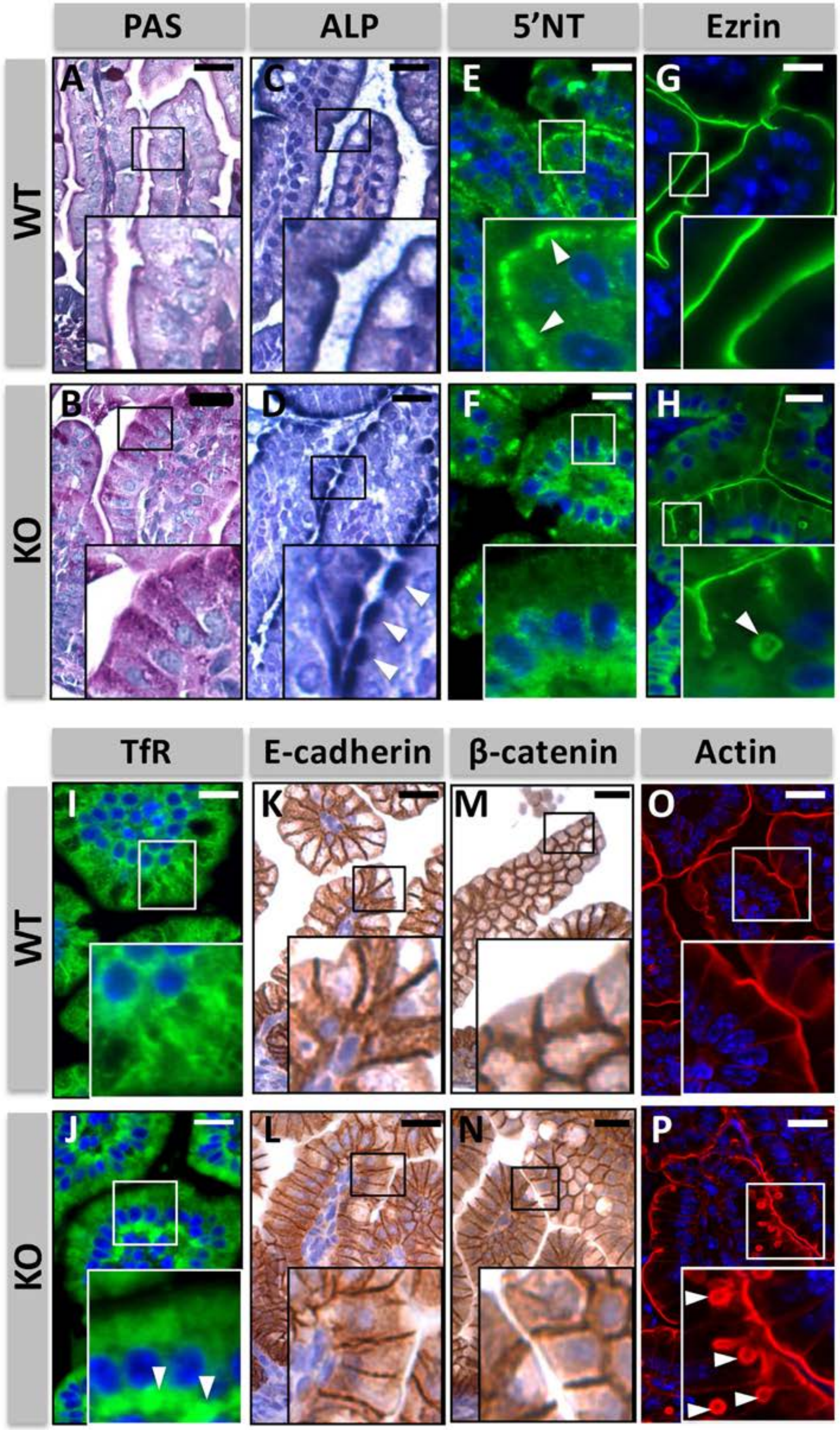

Figure 3. Changes in the localization of apical and basolateral protein markers in Myo5b knockout newborn mice. Periodic acid–Schiff (PAS) staining (**A,B**), alkaline phosphatase (ALP) staining (**C,D**; arrowheads indicate the subapical accumulation of ALP in *Myo5b* knockout mice), immunostaining of 5'-Nucleotidase (5'NT; **E,F**; arrowheads indicate the apical distribution of 5'NT in wild type mice), ezrin (**G,H**; arrowhead indicates an intracellular ezrin-coated vesicle in *Myo5b* knockout mice), transferrin receptor (TfR; **I,J**; arrowheads indicate the basal accumulation of TfR in *Myo5b* knockout mice), E-Cadherin (**K,L**), β-catenin (**M,N**) and actin (**O,P**; arrowheads indicate intracellular actin-coated vesicles in *Myo5b* knockout mice) in *Myo5b* wild type and knockout newborn mice. Scale bar: 25 µm.

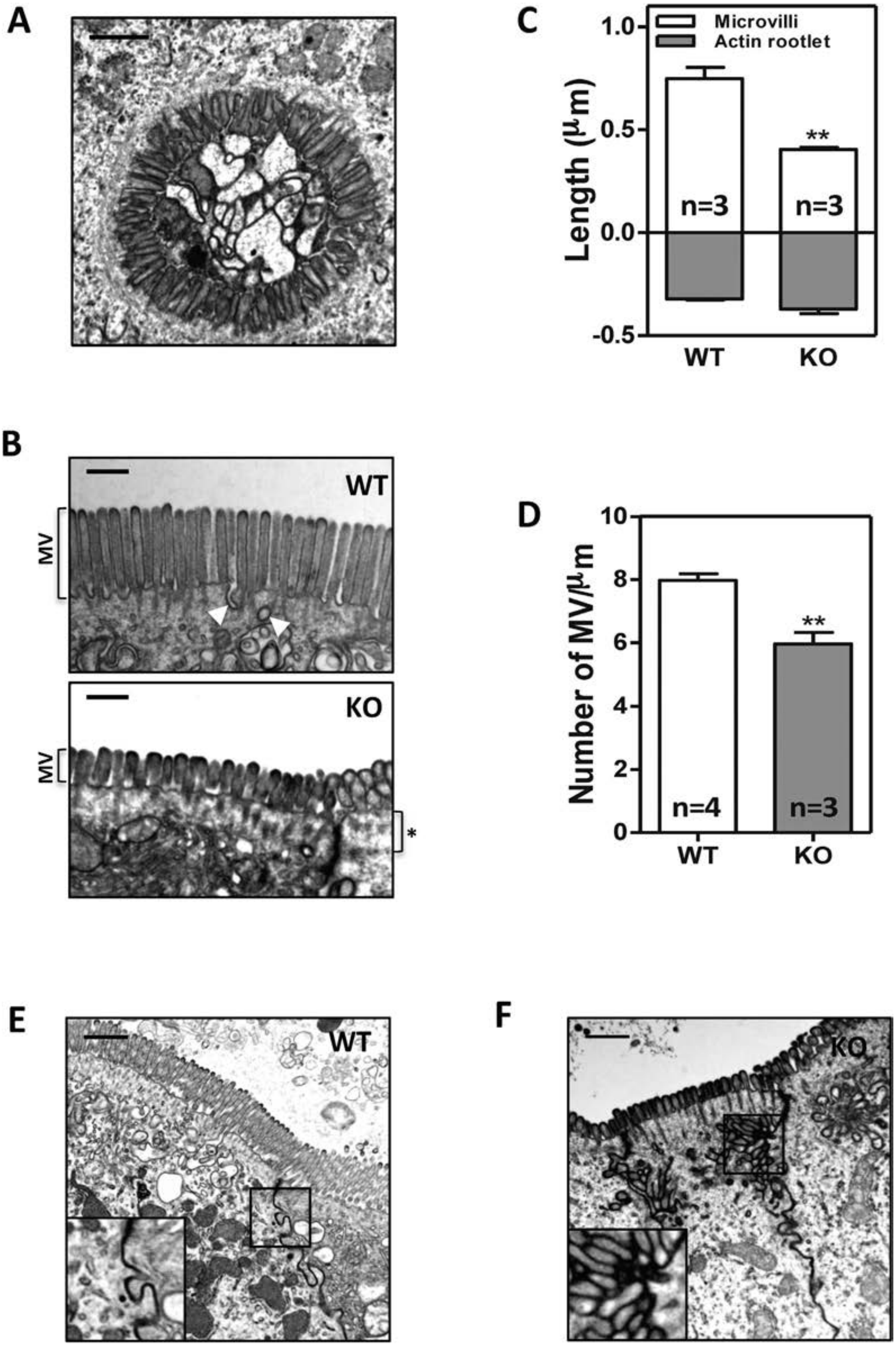

Figure 4. Ultrastructural defects in the intestinal epithelium of knockout *Myo5b* E20 embryos. (**A**) TEM micrograph showing microvillus inclusion bodies in *Myo5b* knockout E20 embryos (scale bar $0.5\,\mu$m). (**B**) Apical microvilli of enterocytes in *Myo5b* wild type and knockout E20 embryos (scale bar $0.5\,\mu$m). MV: microvilli; White arrowheads: subapical microvesicles; asterisk indicates a subapical region devoid of microvesicles. (**C**) Average (±SEM) length of microvilli projecting into the lumen and actin rootlets. (**D**) Number of microvilli observed per micrometer in transverse sections of the brush border. The normal junction between enterocytes in wild type *Myo5b* E20 embryos is shown in (**E**). Scale bar $1\,\mu$m. Microvilli-like structures could be observed in the lateral membrane of enterocytes in *Myo5b* knockout mice (**F**). Scale bar $1\,\mu$m. $^{**}p < 0.01$ (Student's T-test).

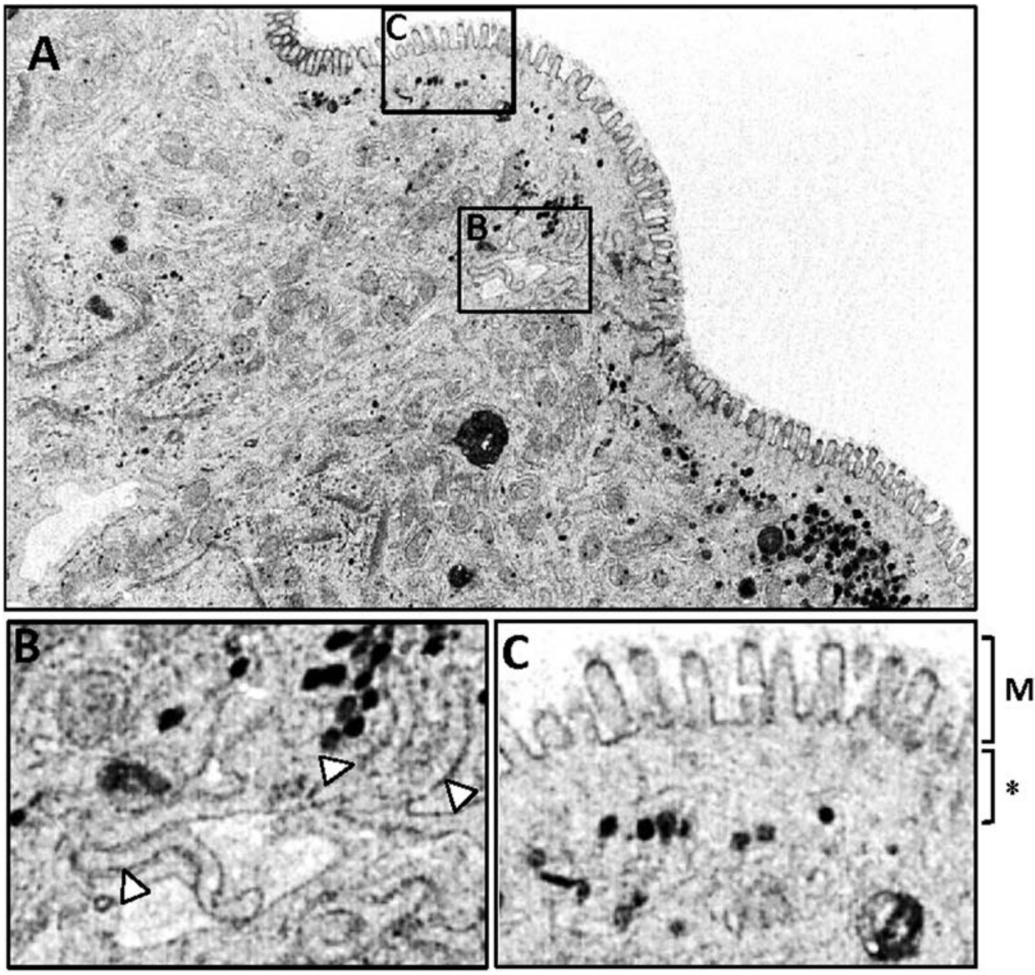

Figure 5. Ultrastructural defects in the intestinal epithelium of MVID patients. (**A**) Transmission electron microscopy pictures from a duodenum biopsy of a MVID patient carrying a homozygous *MYO5B* nonsense mutation (c.4366C > T, p.1456X). (**B**) Larger magnification of a region containing lateral microvilli-like structures (white arrowheads). (**C**) Detail of the apical region containing short/poorly packed microvilli (MV) and a subapical area devoid of microvesicles (asterisk).

of newborn mice to overcome the postnatal hypoglycemia has been shown to be fatal within 18 h[22]. Moreover, although no reproducible defects have been reported in other organs of MVID patients and no histological abnormalities were observed in the *Myo5b* knockout mice, additional studies of the function of other organs and the possible contribution to the death of Myo5b deficient mice are warranted.

Consistent with the changes observed in the intestinal epithelium of MVID patients[1,2], important structural defects were observed in the enterocytes of *Myo5b* knockout newborn mice, including the mislocalization of apical and basolateral markers, microvillus atrophy and the presence of microvillus inclusion bodies. Collectively, this study provides formal demonstration of the inactivation of *Myo5b* as the cause of microvillus inclusion disease. Moreover, these results indicate that the absence of a functional Myosin Vb protein, rather than the presence of pathogenic Myosin Vb mutations[24], is responsible for the intestinal defects observed in MVID patients. In addition, the presence of ultrastructural defects in the enterocytes of Myo5b-deficient E20 embryos indicates that this phenotype is tissue-autonomous. However, the characteristic villus atrophy observed in patients with MVID was not observed in *Myo5b* knockout E20 embryos or newborn mice (Supplementary Figure 2E), suggesting that this phenotype is secondary to environmental cues, such as the prolonged absence of nutrients in their gastrointestinal tract[25]. The *Myo5b* knockout model described here will be instrumental for the characterization of the molecular mechanisms downstream of Myosin Vb responsible for the phenotype observed in patients with MVID, and should significantly contribute to the identification of novel therapeutic approaches for these patients.

It has been reported that up to 75% of MVID patients die before 9 months of age[4]. Different pharmacological approaches have been used in an attempt to stop/reduce the severe diarrhea in these patients, but none of them has proven effective[4]. Patients are dependent on total parenteral nutrition, which over time often causes liver damage and sepsis. Small-bowel transplantation is the only option available to avoid parenteral nutrition and improve the quality of life and the long-term prognosis of these children[11]. However, intestinal transplantation is associated with high rates of rejection and/or mortality[11], and additional therapeutic options are urgently needed for these patients. The *Myo5b* knockout model described here will constitute an ideal system to preclinically test the efficiency of possible new treatment options, including pharmacological or gene therapy using for example autologous reimplantation of intestinal epithelium grown *ex vivo* following restoration of functional Myosin Vb[26].

In conclusion, we describe here the phenotype of *Myo5b* knockout mice, which closely phenocopies human early-onset microvillus inclusion disease. These experiments confirm the important role of Myosin Vb in the formation of the apical brush border and the sorting of apical and basolateral proteins in intestinal absorptive cells, and formally demonstrate that the loss of a functional Myosin Vb protein is responsible for the phenotype observed in MVID patients. The availability of this mouse model of MVID will not only contribute to the characterization of the molecular pathological mechanisms downstream of Myosin Vb leading to novel therapeutic approaches, but also provides an ideal system to preclinically test different treatment options.

Methods

Generation of *Myo5b* knockout mice. *Myo5b*$^{tm1a(KOMP)Wtsi}$ targeted ES cells (C57BL/6N, agouti) were obtained from the KOMP repository at UC Davis[12,27]. After expansion, cells were injected into donor blastocysts and transplanted into pseudopregnant females. Chimeric male offspring were mated to C57BL/6N females to confirm germ line transmission. Animals were genotyped by PCR. The primers used were: Myo5b-F: 5'-CCA GTT CCT TGG GGA CAT AA-3', loxP-F: 5'-GAG ATG GCG CAA CGC AAT TAA TG-3' and Myo5b-R: 5'-AGT GAT GCT GTC CTG AGT GTA CTG G-3'. The initial *tm1a* allele generates a null allele through splicing to a lacZ trapping element, including the mouse En2 splice acceptor and the SV40 polyadenylation sequences (Supplementary Figure 1). Heterozygous *Myo5b*$^{tm1a(KOMP)Wtsi}$ mice were intercrossed to obtain animals homozygous for the targeted *Myo5b* allele (knockout mice). All animal experiments were carried out according to procedures approved by the Ethics Committee for Animal Experimentation at Vall d´Hebron Research Institute.

Transmission electron microscopy. Duodenal samples were collected from *Myo5b* wild type and *Myo5b* knockout E20 embryos (at least 3 animals per genotype). Samples were fixed with 2.5% glutaraldehyde and 2% paraformaldehyde and processed following standard procedures. Ultra-thin sections were mounted on copper grids, contrasted with uranyle acetate/lead citrate double-staining, and observed in a Jeol JEM-1400 (Jeol LTD, Tokyo, Japan) transmission electron microscope equipped with a Gatan Ultrascan ES1000 CCD camera. The brush border architecture was evaluated on a minimum of 12 enterocytes per animal. Microvilli length (actin rootlet and actin core bundles) and microvilli density (microvilli/μm) were measured using ImageJ software. Duodenum biopsy sample from a MVID patient carrying a homozygous *MYO5B* nonsense mutation (c.4366C > T, p.1456X) was obtained after removal of the diseased intestine during the transplantation procedure[10]. The sample was fixed in 2% glutaraldehyde in phosphate buffer, rinsed in 6.8% sucrose in phosphate buffer, and postfixed in a solution of 1% osmium tetroxide in 0.1 mol/L sodium cacodylate buffer containing 11.2% potassium ferrocyanide. Samples were dehydrated with ethanol and processed according to standard procedures upon embedding. Ultra-thin sections were mounted on copper grids and contrasted with uranyle acetate and lead citrate double-staining.

Histology and immunohistochemistry. *Myo5b* wild type and knockout embryos were obtained at day 20 of gestation (E20) and sacrificed by decapitation on ice-cold PBS. Newborns were collected within 6 hours of birth, and sacrificed by decapitation. Both embryos and newborn mice were weighted and measured using a caliper. Blood samples were obtained form tail clips of newborn mice. Glucose levels were measured with a Glucocard G+ meter (Menarini diagnostics, Barcelona). The small and large intestine were dissected from embryos or newborn mice, their length measured and then fixed overnight with 4% formalin, dehydrated by serial immersion in 50%, 70%, 96%, 100% ethanol and xylene and embedded in paraffin. In parallel, formalin-fixed duodenal samples obtained from newborns were cryoprotected in 15% sucrose in PBS overnight, then 30% sucrose overnight. Samples were then immersed in OCT (VWR) and frozen on dry-ice for cryosectioning.

For MYO5B, E-cadherin and β-catenin immunostaining, the NovoLink polymer detection system (Novocastra Laboratories) was used. Inmunostaining was carried out in 3 μm tissue sections, after deparaffination and antigen retrieval with 10 mM citrate buffer pH 6.0 in a pressure cooker for 4 min. The antibodies used were: anti-MYO5B (Atlas antibodies HPA040902; 1:800); anti-E-cadherin (BD Bioscience cat# 610181; 1:100) and β-catenin (BD Bioscience cat# 610154; 1:100). For Ezrin and Transferrin receptor inmunostaining, epitopes were retrieved at 100 °C for 20 minutes in 10 mM citric acid, 0.05% Tween 20 pH6.0. For 5'-nucleotidase, epitopes were retrieved with 10 mM Tris Base, 1 mM EDTA Solution, 0.05% Tween 20, pH 9.0. Non-specific binding sites were blocked with 5% FCS and 1% BSA in PBS overnight. Primary antibodies were diluted in blocking solution with 0.05% Tween 20 at 37 °C for 2 hours followed by 1 hour incubation with Alexa-Fluor-488-conjugated (Ezrin and 5'-nucleotidase) or Alexa-Fluor-543-conjugated secondary antibody (Transferrin receptor). Primary antibodies used were: anti-Ezrin (Tebu Bio, 1:100), anti-Transferrin receptor (Invitrogen, 1:100), anti-5'-nucleotidase (Abgent, 1:50). Nuclei were stained with DAPI and slides were mounted with DAKO mounting medium. For alkaline phosphatase activity detection, slides were incubated with staining solution for a maximum of 1 h at 37 °C. Then, counterstained with hematoxylin and washed with distillated water before mounting. Staining solution contains 0.4 mg/mL 5-Bromo-4-chloro-3-indolyl phosphate p-toluidine (Sigma), 0.5 mg/mL of nitro blue tetrazolium (Sigma), 100 mM $MgCl_2$ (Sigma), 2 mM Levamisole hydrochloride (Santa cruz Biotechnology), 5 mM Sodium azide (Sigma) and 0.15 mM of 1-methoxy-5-methylphenazinium methyl sulphate in 100 mM Tris pH 9.5 (Sigma). Periodic acid-Schiff staining was performed after deparaffination. Briefly, the slides were immersed in 0.5% periodic acid solution (Sigma) for 5 min, washed in distillated water and placed in Schiff reagent (Sigma) for 15 min. Then counterstain with hematoxylin and mounted. For F-Actin staining, 10 μm thick duodenal cryosections were stained with rhodamine phalloidin (Cytoeskeleton), nuclei were counterstained with DAPI and slides were mounted with Prolong antifade reagent (Invitrogen). Fluorescence microscopy pictures were taken with a confocal microscope (FV1000 Olympus).

References

1. Davidson, G. P., Cutz, E., Hamilton, J. R. & Gall, D. G. Familial enteropathy: a syndrome of protracted diarrhea from birth, failure to thrive, and hypoplastic villus atrophy. *Gastroenterology* **75,** 783–90 (1978).
2. Cutz, E. *et al.* Microvillus inclusion disease: an inherited defect of brush-border assembly and differentiation. *N. Engl. J. Med.* **320,** 646–651 (1989).
3. Ruemmele, F. M., Schmitz, J. & Goulet, O. Microvillous inclusion disease (microvillous atrophy). *Orphanet J. Rare Dis.* **1,** 22 (2006).
4. Phillips, A. D. & Schmitz, J. Familial Microvillous Atrophy: A Clinicopathological Survey of 23 Cases. *J. Pediatr. Gastroenterol. Nutr.* **14,** 380–396 (1992).
5. Iancu, T. C., Mahajnah, M., Manov, I. & Shaoul, R. Microvillous inclusion disease: ultrastructural variability. *Ultrastruct. Pathol.* **31,** 173–88 (2007).
6. Müller, T. *et al.* MYO5B mutations cause microvillus inclusion disease and disrupt epithelial cell polarity. *Nat. Genet.* **40,** 1163–5 (2008).
7. Ruemmele, F. M. *et al.* Loss-of-function of MYO5B is the main cause of microvillus inclusion disease: 15 Novel mutations and a CaCo-2 RNAi cell model. *Hum. Mutat.* **31,** 544–551 (2010).
8. Roland, J. T. *et al.* Rab GTPase-Myo5B complexes control membrane recycling and epithelial polarization. *Proc. Natl. Acad. Sci. USA* **108,** 2789–2794 (2011).
9. Golachowska, M. R., Hoekstra, D. & van IJzendoorn, S. C. D. Recycling endosomes in apical plasma membrane domain formation and epithelial cell polarity. *Trends Cell Biol.* **20,** 618–26 (2010).
10. Szperl, A. M. *et al.* Functional characterization of mutations in the myosin Vb gene associated with microvillus inclusion disease. *J. Pediatr. Gastroenterol. Nutr.* **52,** 307–13 (2011).
11. Halac, U. *et al.* Microvillous inclusion disease: how to improve the prognosis of a severe congenital enterocyte disorder. *J. Pediatr. Gastroenterol. Nutr.* **52,** 460–465 (2011).
12. Skarnes, W. C. *et al.* A conditional knockout resource for the genome-wide study of mouse gene function. *Nature* **474,** 337–42 (2011).
13. Turgeon, B. & Meloche, S. Interpreting neonatal lethal phenotypes in mouse mutants: insights into gene function and human diseases. *Physiol. Rev.* **89,** 1–26 (2009).
14. Dhekne, H. S. *et al.* Myosin Vb and Rab11a regulate phosphorylation of ezrin in enterocytes. *J. Cell Sci.* **127,** 1007–17 (2014).
15. Thoeni, C. E. *et al.* Microvillus inclusion disease: loss of myosin Vb disrupts intracellular traffic and cell polarity. *Traffic* **15,** 22–42 (2013).
16. Sato, T. *et al.* The Rab8 GTPase regulates apical protein localization in intestinal cells. *Nature* **448,** 366–9 (2007).
17. Sobajima, T. *et al.* Rab11a is required for apical protein localisation in the intestine. *Biol. Open* 1–9 (2014), doi: 10.1242/bio.20148532.
18. Sakamori, R., Das, S. & Yu, S. Cdc42 and Rab8a are critical for intestinal stem cell division, survival, and differentiation in mice. *J. Clin. Invest.* **122,** 1052–1065 (2012).
19. Van der Velde, K. J. *et al.* An overview and online registry of microvillus inclusion disease patients and their MYO5B mutations. *Hum. Mutat.* **34,** 1597–605 (2013).
20. Segre, J. a, Bauer, C. & Fuchs, E. Klf4 is a transcription factor required for establishing the barrier function of the skin. *Nat. Genet.* **22,** 356–360 (1999).
21. Miyazaki, M., Dobrzyn, A., Elias, P. M. & Ntambi, J. M. Stearoyl-CoA desaturase-2 gene expression is required for lipid synthesis during early skin and liver development. *Proc. Natl. Acad. Sci. USA* **102,** 12501–12506 (2005).
22. Scheuner, D. *et al.* Translational control is required for the unfolded protein response and *in vivo* glucose homeostasis. *Mol. Cell* **7,** 1165–76 (2001).
23. Kuma, A. *et al.* The role of autophagy during the early neonatal starvation period. *Nature* **432,** 1032–1036 (2004).
24. Knowles, B. & Roland, J. Myosin Vb uncoupling from RAB8A and RAB11A elicits microvillus inclusion disease. *J. Clin. Invest.* **124,** 2947–2962 (2014).
25. Shaw, D., Gohil, K. & Basson, M. D. Intestinal mucosal atrophy and adaptation. *World J. Gastroenterol.* **18,** 6357–6375 (2012).
26. Yui, S. *et al.* Functional engraftment of colon epithelium expanded *in vitro* from a single adult $Lgr5^+$ stem cell. *Nat. Med.* **18,** 618–23 (2012).
27. Testa, G. *et al.* A reliable lacZ expression reporter cassette for multipurpose, knockout-first alleles. *Genesis* **38,** 151–8 (2004).

Acknowledgements

This study was partially funded by grants of the Association for International Cancer Research (AICR13-0245), the Spanish Ministry for Economy and Competitiveness (CP05/00256, TRA2009-0093, SAF2008-00789, PI12/03103 and PI12/01095) and Agència de Gestió d'Ajuts Universitaris i de Recerca (AGAUR; SGR 157) to Diego Arango. Fernando Carton is supported by a fellowship from AGAUR (2014FI_B 00426).

Author Contributions

F.C.G., A.O., S.B., H.D., I.M., J.B., S.L., J.H.L., S.S. and S.R.C.: acquisition of data; data analysis and interpretation. R.N.; Technical support. F.C.G., S.I.J. and D.A.: study concept and design; analysis and interpretation of the data; manuscript writing.

Additional Information

Supplementary information accompanies this paper at http://www.nature.com/srep

Competing financial interests: The authors declare no competing financial interests.

How to cite this article: Cartón-García, F. *et al. Myo5b* knockout mice as a model of microvillus inclusion disease. *Sci. Rep.* **5**, 12312; doi: 10.1038/srep12312 (2015).

Myo5b knockout mice as a model of microvillus inclusion disease

Fernando Cartón-García[1,2], Arend Overeem[3], Rocio Nieto[1,2], Sarah Bazzocco[1,2], Higinio Dopeso[1,2], Irati Macaya[1,2], Josipa Bilic[1,2], Stefania Landolfi[4], Javier Hernandez-Losa[4], Simo Schwartz Jr[5], Santiago Ramon y Cajal[4], Sven C. D. van Ijzendoorn[3] and Diego Arango[1,2]

[1]Group of Molecular Oncology, CIBBIM-Nanomedicine, Vall d'Hebron University Hospital, Research Institute (VHIR), Universitat Autònoma de Barcelona, Barcelona, Spain; [2]CIBER de Bioingeniería, Biomateriales y Nanomedicina (CIBER-BBN); Zaragoza, Spain; [3] Department of Cell Biology, University of Groningen, University Medical Center Groningen, Groningen, The Netherlands; [4]Department of Pathology, Vall d'Hebron Hospital, Barcelona, Spain; [5]Group of Drug Delivery and Targeting, CIBBIM-Nanomedicine, Vall d'Hebron University Hospital, Research Institute (VHIR), Universitat Autònoma de Barcelona, Barcelona, Spain.

Supplementary Figure 1

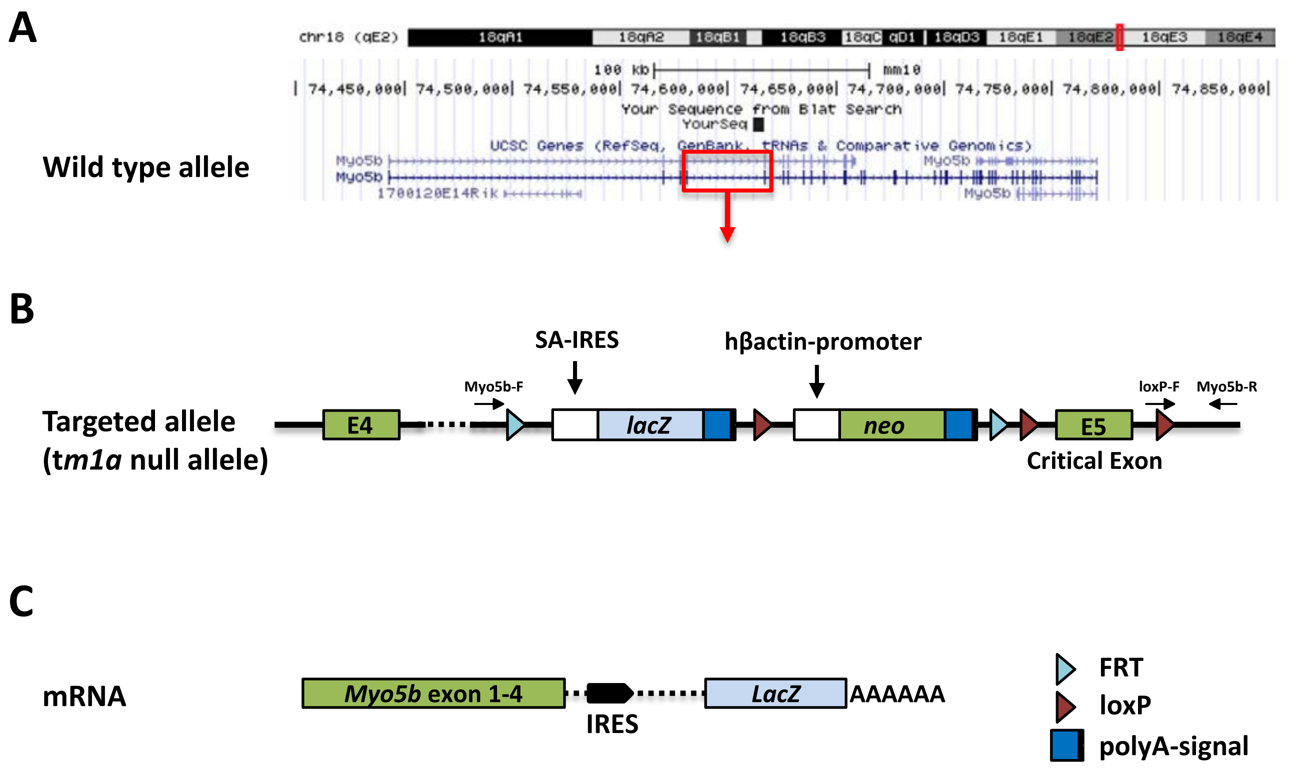

Supplementary Figure 1: Targeted inactivation of *Myo5b*. The wild type *Myo5b* murine allele (**A**) and the targeted allele (**B**) are shown. Using homologous recombination, a trapping element was introduced in intron 4-5 of *Myo5b*, including the mouse *En2* splice acceptor and the SV40 polyadenylation sequences, as well as a neomycin resistance cassette under the control of the human β-actin promoter, flanked by a FRT sites. This allele is predicted to result in a truncated mRNA containing the first 4 exons of *Myo5b* followed by an IRES sequence and the *LacZ* coding sequence (**C**). The strategy used has the potential to be converted into a conditional knockout system by crossing these mice with an Flp deleter mouse (not pursued here). Horizontal black arrows in (**B**) indicate the location of the PCR primers used for genotyping.

Supplementary Figure 2

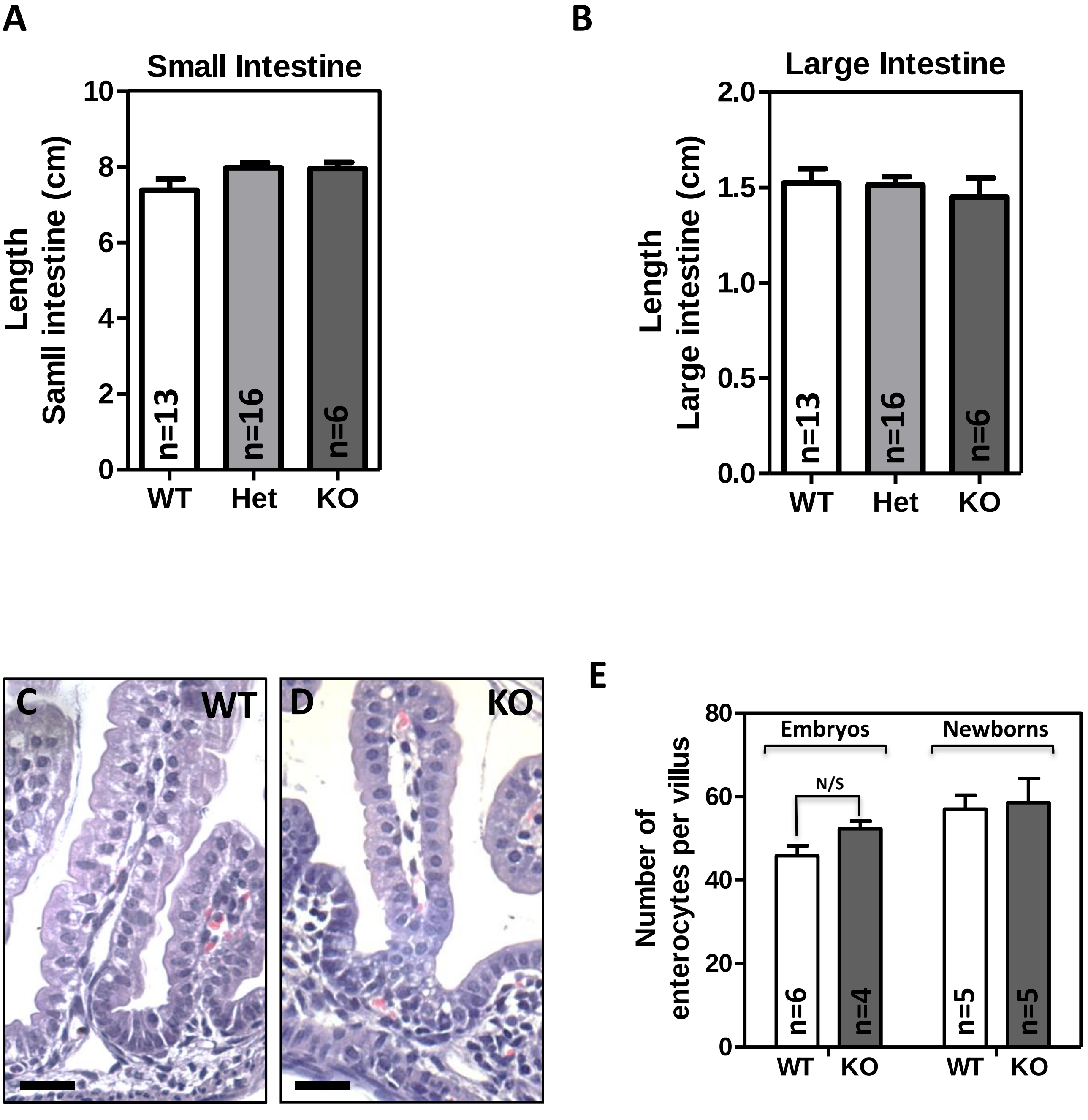

Supplementary Figure 2: Histology and anatomy of the intestine of *Myo5b* knockout mice. (**A-B**) Average length (±SE) of the small (**A**) and large (**B**) intestine of newborn mice that are wild type, heterozygous or knockout for *Myo5b*. N: number of animals per group. (**C-D**) Sections from formalin-fixed, paraffin-embedded samples from the small intestine of newborn *Myo5b* wild type (**C**) and knockout (**D**) mice were stained with hematoxylin and eosin. Scale bar 25µm. (**E**) The number of epithelial cells in at least five longitudinally sectioned villi per mouse was scored blinded from the sample identity in E20 embryos and newborn mice. The average (±SE) is shown. N: number of animals per group.

Supplementary Figure 3

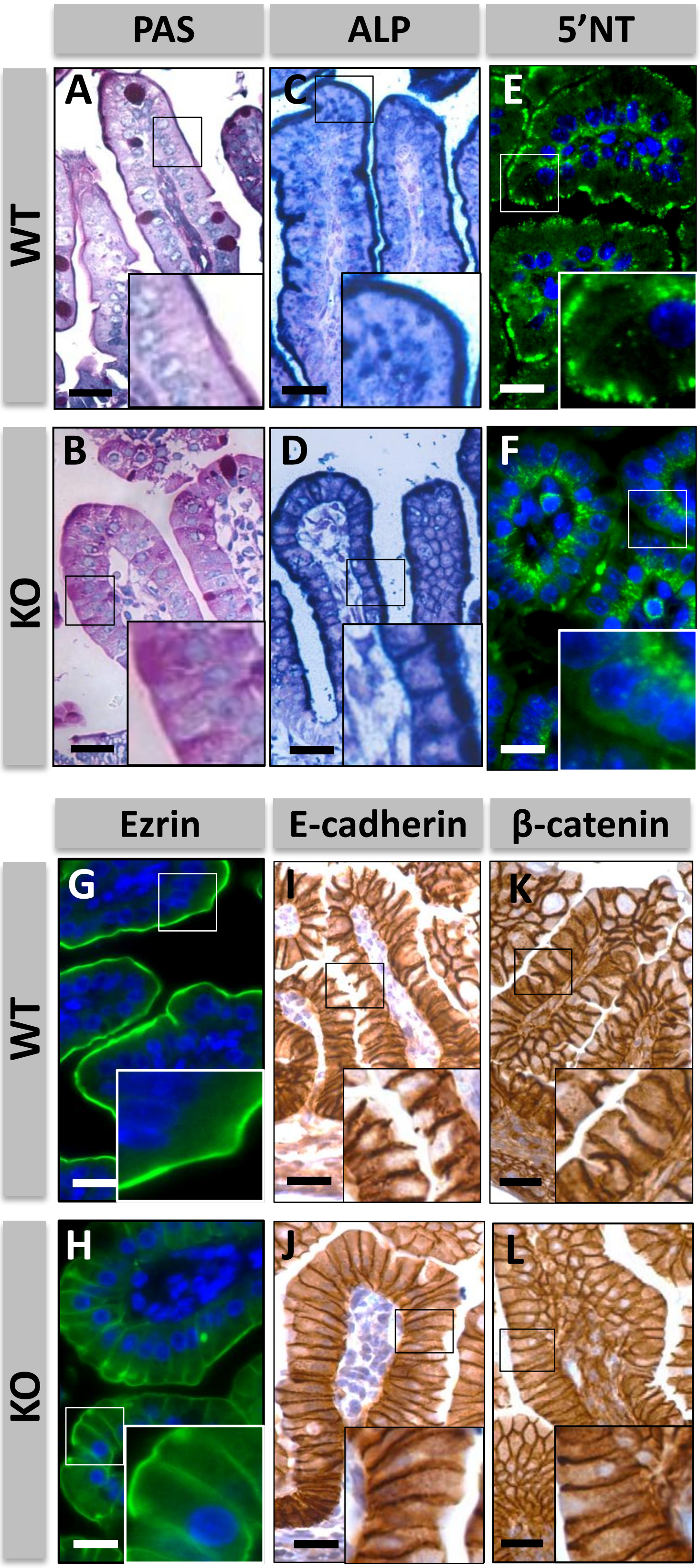

Supplementary Figure 3: Structural changes in the intestinal epithelial cells of *Myo5b* E20 embryos. (**A-L**) Periodic acid–Schiff (PAS) staining (**A-B**), alkaline phosphatase staining (ALP; **C-D**), immunostaining of 5'-Nucleotidase (5’NT; **E-F**), ezrin (**G-H**), E-Cadherin (**I-J**) and β-catenin (**K-L**) in *Myo5b* wild type and knockout E20 embryos. Scale bar: 25 μm.

Supplementary Figure 4

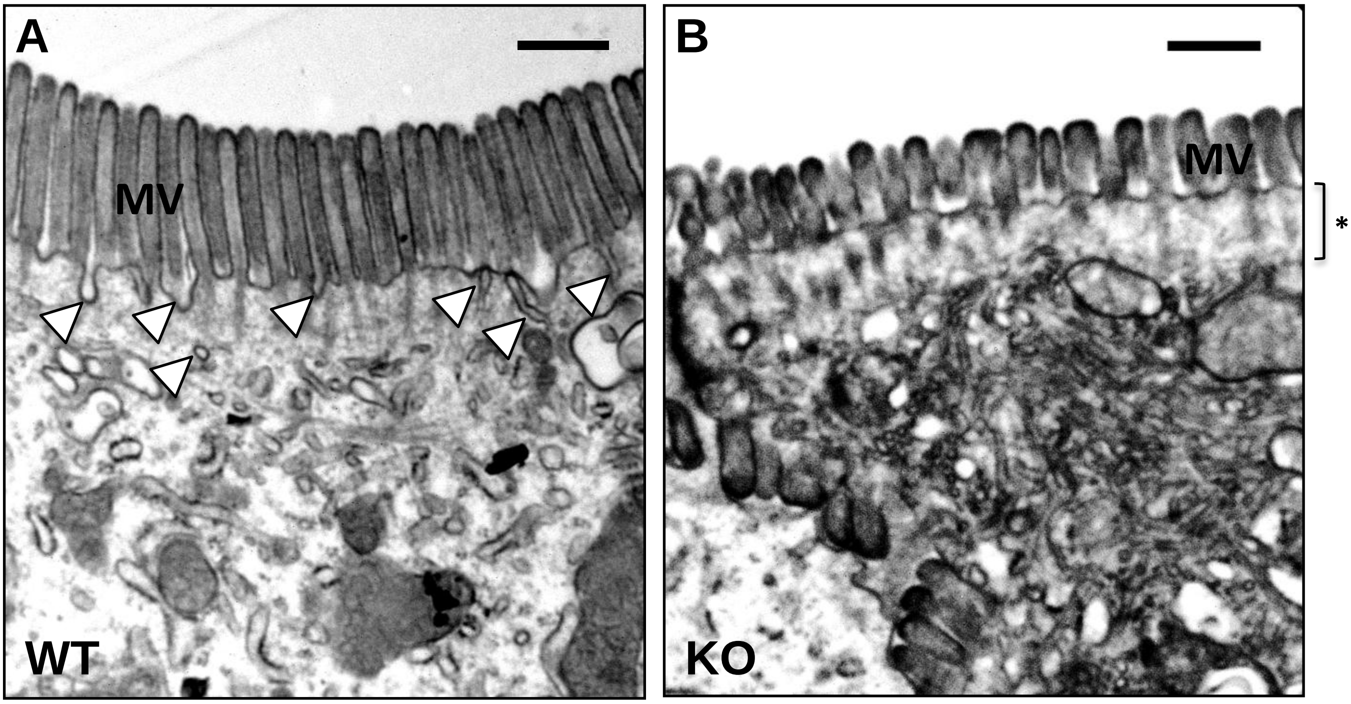

Supplementary Figure 4: Apical region of enterocytes from *Myo5b* wild type and knockout mice. Representative transmission electron microscopy micrographs of the apical region of enterocytes from *Myo5b* wild type (**A**) and knockout (**B**) mice. Enterocytes from *Myo5b* knockout mice showed shorter microvilli (MV) and a subapical region lacking microvesicle trafficking (asterisk). White arrowheads indicate apical vesicle trafficking in the *Myo5b* wild type enterocytes. Scale bar: 0.5 µm.